Article

# Radiation-induced amphiregulin drives tumour metastasis

https://doi.org/10.1038/s41586-025-08994-0

Received: 31 May 2023

Accepted: 8 April 2025

Published online: 14 May 2025

Check for updates

András Piffkó[1,2,3,15], Kaiting Yang[1,2,4,15], Arpit Panda[5,6,15], Janna Heide[7], Krystyna Tesak[1,2,5], Chuangyu Wen[1,2], Katarzyna Zawieracz[8], Liangliang Wang[1,2,9], Emile Z. Naccasha[1,2], Jason Bugno[1,2,10], Yanbin Fu[1,2,11], Dapeng Chen[1,2], Leonhard Donle[7], Ernst Lengyel[7], Douglas G. Tilley[12], Matthias Mack[13], Ronald S. Rock[5], Steven J. Chmura[1,2], Everett E. Vokes[14], Chuan He[5,6], Sean P. Pitroda[1,2,15], Hua Laura Liang[1,2,15] & Ralph R. Weichselbaum[1,2,15] ✉

The anti-tumour effect of radiotherapy beyond the treatment field—the abscopal effect—has garnered much interest[1]. However, the potentially deleterious effect of radiation in promoting metastasis is less well studied. Here we show that radiotherapy induces the expression of the EGFR ligand amphiregulin in tumour cells, which reprogrammes EGFR-expressing myeloid cells toward an immunosuppressive phenotype and reduces phagocytosis. This stimulates distant metastasis growth in human patients and in pre-clinical mouse tumour models. The inhibition of these tumour-promoting factors induced by radiotherapy may represent a novel therapeutic strategy to improve patient outcomes.

Radiotherapy has a critical role in cancer treatment and approximately 50–60% of cancer patients receive radiotherapy during their treatment course[2]. Ionizing radiation causes cell death principally through the induction of DNA damage and immune-mediated anti-tumour effects such as dendritic cell-mediated T-cell priming[3,4]. However, radiotherapy-induced immunosuppressive factors—such as the recruitment of regulatory T cells and myeloid-derived suppressor cells, or the production of immunosuppressive cytokines—have a negative effect on radiotherapy outcomes[5,6]. Although radiotherapy primarily treats localized tumours, its potential as a curative option in oligometastatic disease or in combination with immune checkpoint blockade (ICB) for widespread metastases is gaining interest[7]. Despite the potentially synergistic immune-activating mechanisms of radiotherapy and ICB, clinical trials have failed to meet primary endpoints in metastatic disease[1,8]. We hypothesize that radiotherapy-induced factors that promote distant tumour growth contribute to treatment failure, a phenomenon that we term the 'badscopal' effect[9].

EGFR is activated by amphiregulin (AREG) through dimerization and autophosphorylation[10,11], which are integral to type 2 immune-mediated tolerance and resistance mechanisms in various immune cells[12–14]. AREG overexpression occurs across multiple cancers[15,16], and has been linked to intestinal epithelial regeneration following radiotherapy[17], but the role of tumour-cell derived AREG in response to radiotherapy remains unclear.

Here we identify radiotherapy-induced upregulation of *AREG* in patients with metastatic solid tumours from a multisite stereotactic body radiotherapy (SBRT) trial (ClinicalTrials.gov ID: NCT02608385)[18]. Radiotherapy-mediated *AREG* induction correlated with distant metastasis progression. In mouse lung metastasis models, tumour cell-derived AREG promoted lung metastasis growth by reprogramming $EGFR^+$ mononuclear phagocytes (MNPs)[19] into an immunosuppressive phenotype. AREG also suppressed MNP phagocytosis via increased CD47 expression on tumour cells. Notably, targeting AREG prevented radiotherapy-induced metastasis growth and enhanced radiotherapy efficacy. Whereas most of the 'classical' predictors of radiotherapy outcome, such as tumour histology, size and molecular subtype, are not modifiable after radiotherapy initiation, our findings suggest that inhibiting specific radiation-induced metastasis-promoting proteins could improve cancer therapy.

## Radiotherapy promotes distant metastasis growth

We profiled gene expression in patients with advanced solid tumours, who received SBRT to multiple metastatic sites[18] (Supplementary Table 1; ClinicalTrials.gov ID: NCT02608385). In 22 matched pre- and post-radiotherapy biopsies from irradiated metastases, we identified 60 overlapping genes that: (1) increased in expression following SBRT; and (2) positively correlated with progression of distant unirradiated metastases (Fig. 1a and Supplementary Table 2). Among these, the EGFR ligand *AREG* was involved in three of the top 20 upregulated gene pathways that correlated with distant tumour progression (Extended Data Fig. 1a). Stratifying the patient cohort by the change in *AREG* expression in response to radiotherapy demonstrated a shorter progression-free survival and overall survival in patients whose tumours exhibited

[1]Department of Radiation and Cellular Oncology, University of Chicago, Chicago, IL, USA. [2]The Ludwig Center for Metastasis Research, University of Chicago, Chicago, IL, USA. [3]Department of Neurosurgery, University Medical Center Hamburg-Eppendorf, Hamburg, Germany. [4]School of Biomedical Sciences and Engineering, South China University of Technology, Guangzhou International Campus, Guangzhou, P. R. China. [5]Department of Chemistry, Department of Biochemistry and Molecular Biology, and Institute for Biophysical Dynamics, University of Chicago, Chicago, IL, USA. [6]Howard Hughes Medical Institute, University of Chicago, Chicago, IL, USA. [7]Department of Obstetrics and Gynecology/Section Gynecologic Oncology, University of Chicago, Chicago, IL, USA. [8]Department of Pathology, Section of Hematology/Oncology, University of Chicago, Chicago, IL, USA. [9]The Laboratory of Microbiome and Microecological Technology, Institute of Microbiology, Chinese Academy of Sciences, Beijing, P. R. China. [10]Committee on Clinical Pharmacology and Pharmacogenomics, University of Chicago, Chicago, IL, USA. [11]Drukier Institute for Children's Health, Department of Pediatrics, Weill Cornell Medicine, New York, NY, USA. [12]Department of Cardiovascular Sciences, Temple University, Philadelphia, PA, USA. [13]Department of Internal Medicine, University of Regensburg, Regensburg, Germany. [14]Department of Medicine, University of Chicago, Chicago, IL, USA. [15]These authors contributed equally: András Piffkó, Kaiting Yang, Arpit Panda, Sean P. Pitroda, Hua Laura Liang, Ralph R. Weichselbaum. ✉e-mail: ralph.weichselbaum@uchospitals.edu

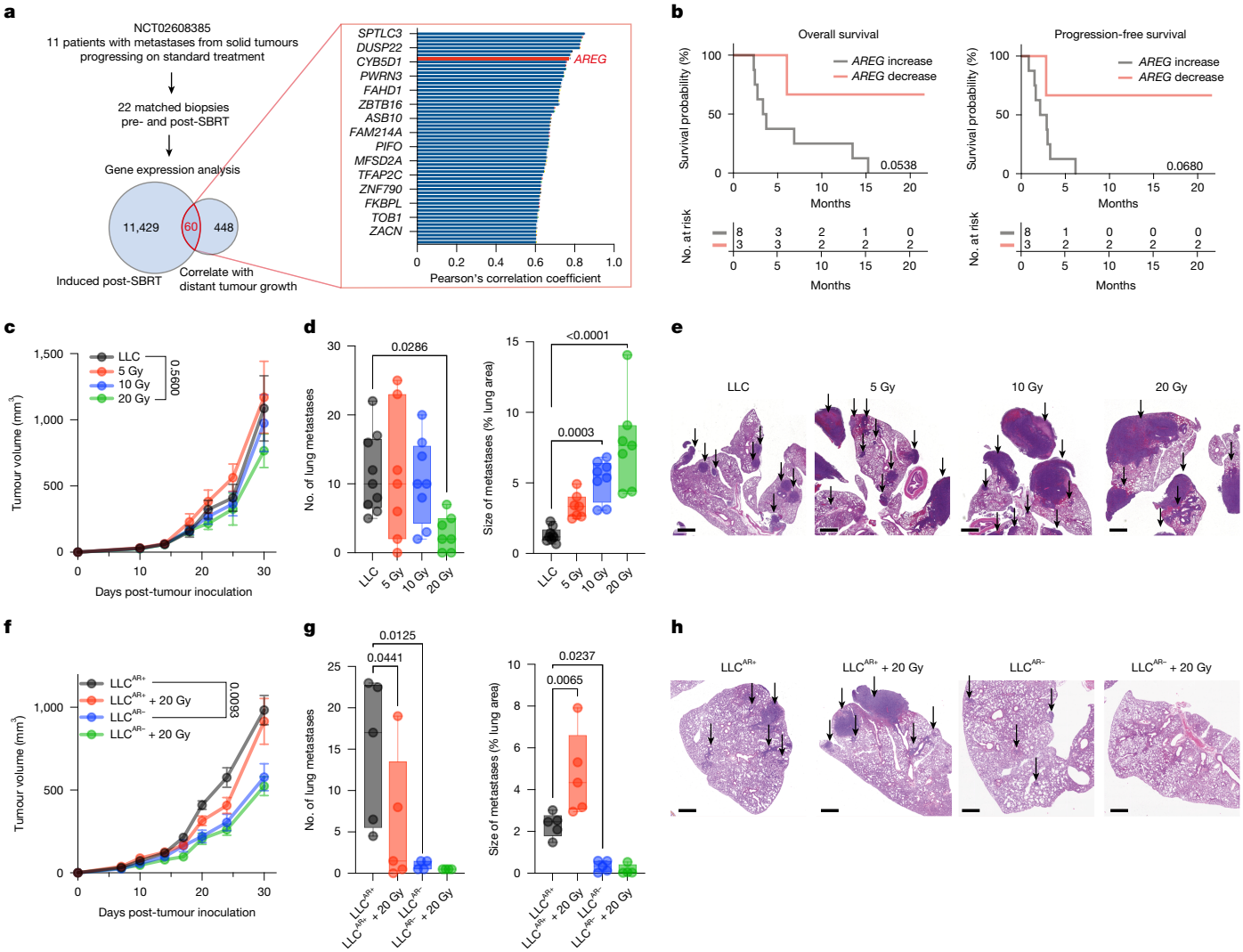



**Fig. 1 | Radiotherapy induces amphiregulin expression and growth of distant metastasis. a**, Schematic of biopsy acquisition and gene expression analysis; genes that are induced by SBRT and correlate with growth of distant metastases are highlighted (right). Pearson correlation coefficient of 60 genes: distant tumour progression based on RECIST (response evaluation criteria in solid tumors) criteria was correlated with gene expression post-SBRT in a microarray of $n = 22$ matched pre- and post-SBRT biopsies from $n = 11$ patients. **b**, Kaplan–Meier plot showing overall survival (left) and progression-free survival (right), stratified by increase or decrease of *AREG* expression post-SBRT (log-rank (Mantel–Cox) test). **c**, Growth curve of LLC flank tumours with or without radiotherapy with 5, 10 or 20 Gy ($n = 5$ mice per group). Two-way ANOVA, Dunnett's test. **d**, Number of lung metastases (left), and mean size of the five largest metastases per lung area (right). LLC: $n = 9$; 5 Gy: $n = 7$; 10 Gy: $n = 8$; 20 Gy: $n = 7$ mice, pooled from two separate experiments. One-way ANOVA, Dunnett's test. **e**, Haematoxylin and eosin (H&E) staining. Black arrows indicate metastatic lesions. **f**, Growth curve of $LLC^{AR+}$ and $LLC^{AR-}$ flank tumours with or without 20 Gy treatment. $n = 10$ mice per group, pooled from 2 independent experiments. Two-way ANOVA, Tukey's test. **g**, Number of lung metastases (left), and mean size of the five largest metastases per lung area (right). $n = 5$ mice per group. One-way ANOVA, Šídák's test. **h**, H&E staining. Black arrows indicate metastatic lesions. Data are mean ± s.e.m. In box plots, the centre line shows the median, box edges delineate first and third quartiles, and whiskers show the range of values. Scale bars, 500 µm.

increased *AREG* expression following SBRT (Fig. 1b). Supporting these findings, analysis of data from patients with radiotherapy-treated lung squamous cell cancer (LUSC) from The Cancer Genome Atlas (TCGA) confirmed an association between higher tumour *AREG* expression and poor prognosis (Extended Data Fig. 1b).

We utilized the mouse Lewis lung carcinoma (LLC) model of spontaneous lung cancer metastasis to characterize the mechanisms by which radiotherapy-induced AREG expression contributes to distant metastasis. LLC tumour cells were implanted subcutaneously in the flank of C57BL/6 wild-type mice and treated with local radiotherapy (5, 10 and 20 Gy) after 12–14 days. The resulting tumours showed a high degree of radiation resistance at these doses (Fig. 1c). Although 20 Gy treatment decreased the number of lung metastases, both 10 Gy and 20 Gy treatments significantly increased the mean size of lung metastases compared with metastases derived from non-irradiated tumours (Fig. 1d,e). Irradiation of LLC flank tumours induced a significant, dose-dependent increase of local and systemic AREG concentration with highest levels at 20 Gy; this response was absent following radiotherapy in non-tumour bearing mice, indicating that AREG upregulation is specific to irradiated tumour tissues (Extended Data Fig. 1c–e). Similar flank tumour and lung metastasis size was observed in wild-type mice and in $Vav1^{\Delta Areg}$ mice, in which all haematopoietic and endothelial lineages lack *Areg*[20] (Extended Data Fig. 1f,g). These data reinforced that although a range of tissues can produce AREG, tumour cell-derived AREG has a central role in mediating the metastasis phenotype.

In addition, we verified that lung metastases were present at the time of systemic radiotherapy-induced AREG upregulation (five days post-radiotherapy) (Extended Data Fig. 1h,i). Whereas early irradiation

of smaller tumours on day 8 reduced the number and size of lung metastases (Extended Data Fig. 1j), a significant increase in metastasis size of larger tumours (radiotherapy on day 20) coincided with greater systemic AREG levels 5 days post-radiotherapy (mean ± s.e.m. flank tumour sizes 79.95 ± 6.10 $mm^3$ and 415.80 ± 30.02 $mm^3$, respectively; Extended Data Fig. 1k–m). A positive correlation was observed between tumour size at the time of radiotherapy and the induction of serum AREG 5 days after radiotherapy, suggesting that larger irradiated tumours secrete more AREG (Extended Data Fig. 1n).

## *Areg* knockout reduces distant metastasis growth

We generated a CRISPR–Cas9 genome-edited knockout of *Areg* in LLC cells expressing red fluorescent protein (RFP; we call these cells $LLC^{AR-}$ and the corresponding wild-type cells $LLC^{AR+}$) to evaluate the effect of AREG on metastasis growth and response to irradiation. $LLC^{AR-}$ tumours did not upregulate AREG after radiotherapy (Extended Data Fig. 2a–c). Non-irradiated $LLC^{AR-}$ tumours exhibited slower tumour growth than $LLC^{AR+}$ tumours, and a high degree of radiation resistance persisted in flank tumours of both genotypes (Fig. 1f). Moreover, $LLC^{AR-}$ tumours resulted in significantly smaller and fewer lung metastases, and the size of $LLC^{AR-}$ lung metastases did not increase following flank tumour radiotherapy (Fig. 1g,h). These results were reproduced in an orthotopic lung cancer model, in which computed tomography (CT)-guided irradiation of intraparenchymal lung tumours resulted in increased systemic AREG concentration and size of contralateral lung metastases in $LLC^{AR+}$ tumour-bearing mice but not in $LLC^{AR-}$ tumour-bearing mice (Extended Data Fig. 2d–h).

In the breast cancer cell line EO771-LMB[21] (hereafter LMB), which spontaneously metastasises to the lung and also upregulates *Areg* in response to radiotherapy, 20 Gy suppressed both flank tumour and lung metastasis growth (Extended Data Fig. 2i,j). However, a single dose of 5 Gy, which does not suppress LMB flank tumour growth, led to a significant size increase of lung metastases compared with untreated controls, suggesting that distant metastasis proliferation may be particularly pronounced in the setting of ineffective local tumour control (Extended Data Fig. 2j–l). Similar to the effects observed in LLC, CRISPR-mediated *Areg* knockout prevented radiation-induced *Areg* upregulation and significantly delayed the growth of flank tumours without affecting the response of the tumour to radiotherapy (Extended Data Fig. 2m,n). *Areg*-knockout LMB tumours also exhibited a reduced number and size of spontaneous lung metastases, and radiotherapy-related metastasis growth was absent (Extended Data Fig. 2o,p). These findings indicate that although local radiotherapy can reduce the number of lung metastases, it can also increase the size of established lung metastases through AREG upregulation.

*Areg* knockout and treatment with recombinant AREG did not affect the proliferative (Extended Data Fig. 3a) or migratory (Extended Data Fig. 3b) capacity of wild-type or *Areg*-knockout tumour cells in vitro. Similarly, effects of radiotherapy on proliferation, migration and clonogenic survival were unchanged (Extended Data Fig. 3c–h). To delineate whether the seeding or growth of lung metastases is affected by tumour cell-derived AREG, we injected $LLC^{AR+}$ and $LLC^{AR-}$ cells intravenously. $LLC^{AR+}$ and $LLC^{AR-}$ cells extravasated and formed comparable numbers of micrometastases by day 7 post-intravenous injection (Extended Data Fig. 4a,b). By day 14, however, $LLC^{AR-}$ metastases were significantly fewer in number and smaller than $LLC^{AR+}$ metastases (Extended Data Fig. 4c,d). Notably, the number of $LLC^{AR-}$ lung metastases declined between days 7 and 14, suggesting an immune-mediated reduction of AREG-deficient metastases.

To recapitulate the AREG-induced phenotype, we used intravenous injection of recombinant AREG (rAREG), which significantly increased the size of $LLC^{AR-}$ lung metastases, implying that in the absence of tumour-derived AREG, AREG supplementation can drive lung metastasis growth (Extended Data Fig. 4e). We next explored whether this mechanism is unique in the context of radiotherapy or whether other types of tissue injury similarly elicit lung metastasis growth and found that surgical resection of the flank tumour did not increase systemic AREG levels or lung metastasis size (Extended Data Fig. 4f–i). Mechanistically, we found that after radiotherapy of $LLC^{AR+}$ cells, AREG induction was mediated by type I interferon signalling (Extended Data Fig. 4j,k), consistent with previous reports[22]. Furthermore, IFNβ treatment significantly increased AREG RNA and protein levels, an effect that was attenuated by knockdown of the type I interferon-related transcription factor STAT2 (Extended Data Fig. 4l–o). In summary, local radiotherapy reduces the number of lung metastases but increases their size via AREG secretion, mediated by type I interferon signalling. *Areg* knockout prevents this effect.

## Radiotherapy-induced AREG targets $EGFR^+$ MNPs

We hypothesized that the host immune response contributed to the AREG-dependent metastatic growth observed in patients and mouse models. AREG induces EGFR phosphorylation at tyrosine residue 992 (Tyr992), which has previously been implicated in the dysplasia severity of oesophageal carcinomas[23,24]. We utilized spectral flow cytometry to validate the presence of Tyr992 phosphorylated EGFR-positive ($p\text{-}EGFR^+$) immune cells in peripheral blood mononuclear cells (PBMCs) of patients with metastatic non-small cell lung cancer (NSCLC) treated with SBRT in a second clinical trial[25] (ClinicalTrials.gov ID: NCT03223155; Supplementary Table 3). We analysed matched pre- and post-SBRT PBMC samples from 15 patients and created a *t*-distributed stochastic neighbour embedding (*t*-SNE)[26] projection of 800,000 live $CD45^+$ cells. The highest expression of Tyr992 p-EGFR was found on monocytes ($CD33^+CD14^+$) and dendritic cells ($CD11c^+CD141^+HLA\text{-}DR^+$) (Fig. 2a–c and Extended Data Fig. 5a–c). The fraction of $CD33^+CD14^+$ $p\text{-}EGFR^+$ monocytes increased after SBRT (Fig. 2d). Trichotomization of the NSCLC patient cohort on the basis of the fold change of $CD33^+CD14^+$ $p\text{-}EGFR^+$ monocytes demonstrated a significantly worse overall survival in the patients with the greatest increase following SBRT (Fig. 2e,f).

Mirroring our findings in PBMCs, the cell types with the highest Tyr992 p-EGFR expression in mouse lung tissues were myeloid cells: $CD11b^+Ly6G^+$ granulocytes, $CD11c^+MHCII^+$ dendritic cells and $CD11b^+Ly6C^+F4/80^+$ MNPs (Fig. 2g–i and Extended Data Fig. 5d–f). The fraction of myeloid cells significantly increased in the lungs of flank tumour-bearing mice compared with non-tumour bearing mice (Extended Data Fig. 5g). Whereas radiotherapy resulted in a similar increase of $Ly6G^+$ granulocytes in the lungs of $LLC^{AR+}$ and $LLC^{AR-}$ tumour-bearing mice, the fraction of $p\text{-}EGFR^+Ly6C^+$ MNPs exhibited a unique increase after radiotherapy in $LLC^{AR+}$ tumour-bearing mice, but did not increase in the lungs of $LLC^{AR-}$ tumour-bearing mice post-radiotherapy (Fig. 2j and Extended Data Fig. 5h). These results suggested a possible link between $Ly6C^+$ MNPs, radiotherapy-induced AREG and the increased metastasis size observed in mice bearing $LLC^{AR+}$ tumours treated with 20 Gy. Similar patterns were not observed in $CD4^+$ and $CD8^+$ T cells or $CD19^+$ B cells (Extended Data Fig. 5h,i). We verified the presence of $p\text{-}EGFR^+Ly6C^+$ MNPs in the lung metastatic microenvironment by confocal microscopy (Fig. 2k) and developed an artificial intelligence (AI)-based cell segmentation model, which detected a significant increase of $Ly6C^+$ MNPs post-radiotherapy (Fig. 2l and Extended Data Fig. 5j,k). These findings demonstrate that: (1) MNPs are the primary immune cells expressing Tyr992 p-EGFR in PBMCs from patients with NSCLC and in lung tissues from mice bearing $LLC^{AR+}$ flank tumours; and (2) radiotherapy drives an increase in $Ly6C^+$ MNPs in the lung metastatic microenvironment, a process that is reversed by *Areg* knockout.

## AREG reshapes MNP trajectories

MNPs were identified as target populations of tumour-secreted, radiotherapy-induced AREG. Since circulating $Ly6C^+$ monocytes can

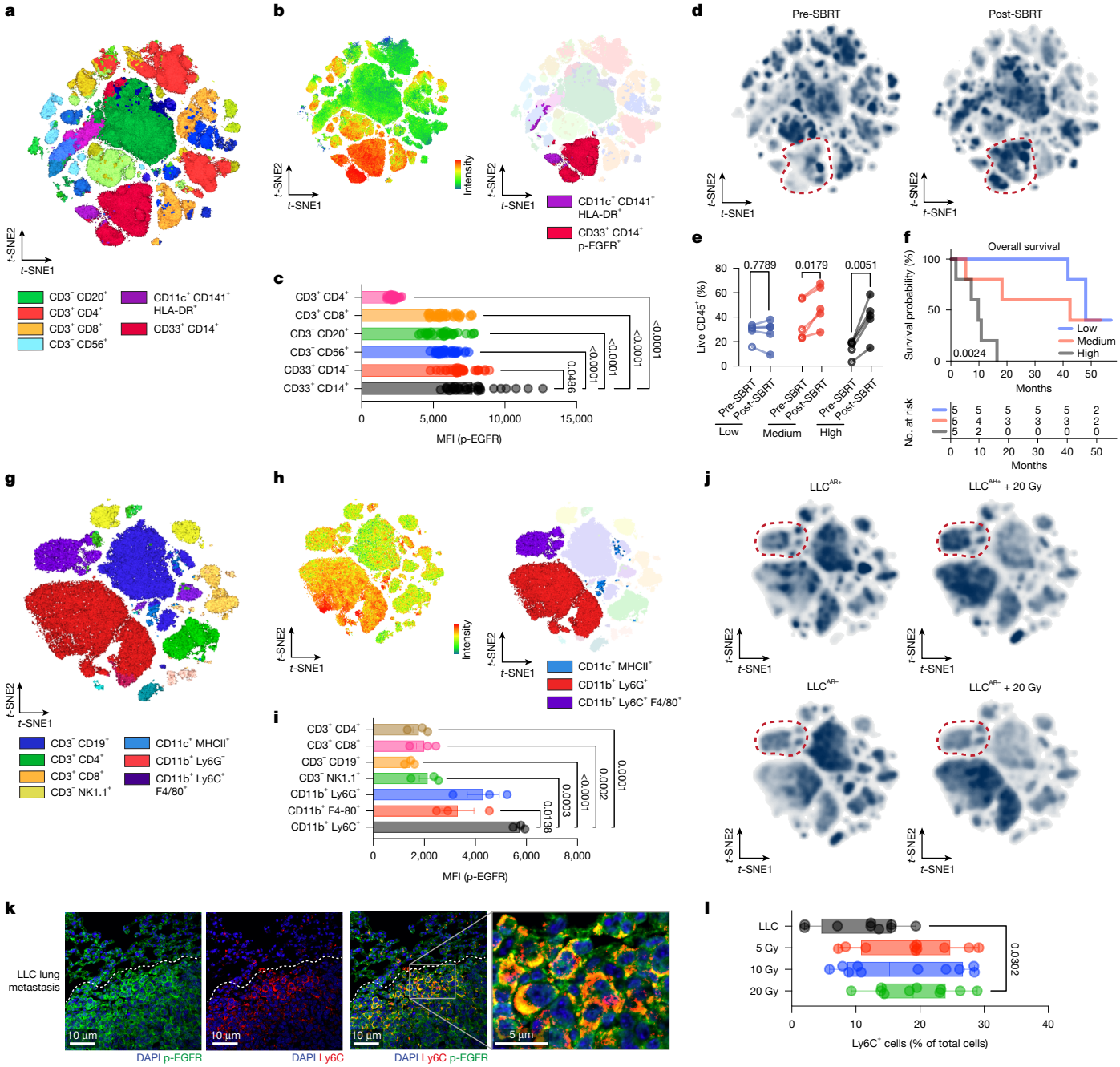



**Fig. 2 | Radiation-induced AREG modulates the myeloid immune landscape in NSCLC patient PBMCs and a mouse lung metastasis model. a**, Spectral flow cytometry. *t*-SNE clustering of 800,000 live CD45$^+$ PBMCs of matched pre- and post-SBRT samples from $n = 15$ patients. **b**, Tyr992 p-EGFR expression intensity (left) and the top p-EGFR-expressing clusters (right) projected on the *t*-SNE from **a**. **c**, Mean fluorescence intensity (MFI) of Tyr992 p-EGFR in manually gated immune cell populations (pre- and post-SBRT combined). One-way ANOVA, Šídák's test. **d**, Density plots of *t*-SNE from PBMCs pre- and post-SBRT; the p-EGFR$^+$CD33$^+$CD14$^+$ population is outlined. **e**, PBMC trichotomized by fold change in p-EGFR$^+$CD33$^+$CD14$^+$ frequency pre- and post-SBRT (left); high (>2,0-fold), medium (1.1–1.9-fold) and low (0.6–1.1-fold). Unpaired two-sided *t*-test. **f**, Kaplan–Meier survival curves of trichotomized patient groups ($n = 5$ per group). Log-rank (Mantel–Cox) test. **g**, Spectral flow cytometry. *t*-SNE clustering of 230,000 live CD45$^+$ immune cells from lungs of non-tumour-bearing and tumour-bearing mice. **h**, Tyr992 p-EGFR expression intensity (left) and top p-EGFR-expressing clusters (right) projected on the *t*-SNE from **g**. **i**, MFI of Tyr992 p-EGFR in manually gated immune cell populations from non-tumour bearing mice. $n = 3$ mice per group. One-way ANOVA, Šídák's test. **j**, Density plot of *t*-SNE from lung tissue stratified by experimental condition; the p-EGFR$^+$Ly6C$^+$ F4/80$^+$ population is outlined. $n = 5$ per group. **k**, Immunofluorescence staining of Ly6C$^+$Tyr992p-EGFR$^+$ MNPs in the metastatic tumour microenvironment of LLC lung metastases (Ly6C PE/Dazzle 594, red; Tyr992 p-EGFR AF488, green; DAPI, blue), representative of two independent experiments. **l**, Frequency of Ly6C$^+$ MNPs in the LLC lung metastatic microenvironment post 5, 10 and 20 Gy radiotherapy, determined by AI-assisted Cellpose segmentation model and logistic regression classifier ($n = 9$ LLC mice, $n = 10$ mice in all others, pooled from two independent experiments). One-way ANOVA, Šídák's test. Data are mean ± s.e.m. In box plots, the centre line shows the median, box edges delineate first and third quartiles, and whiskers show the range of values.

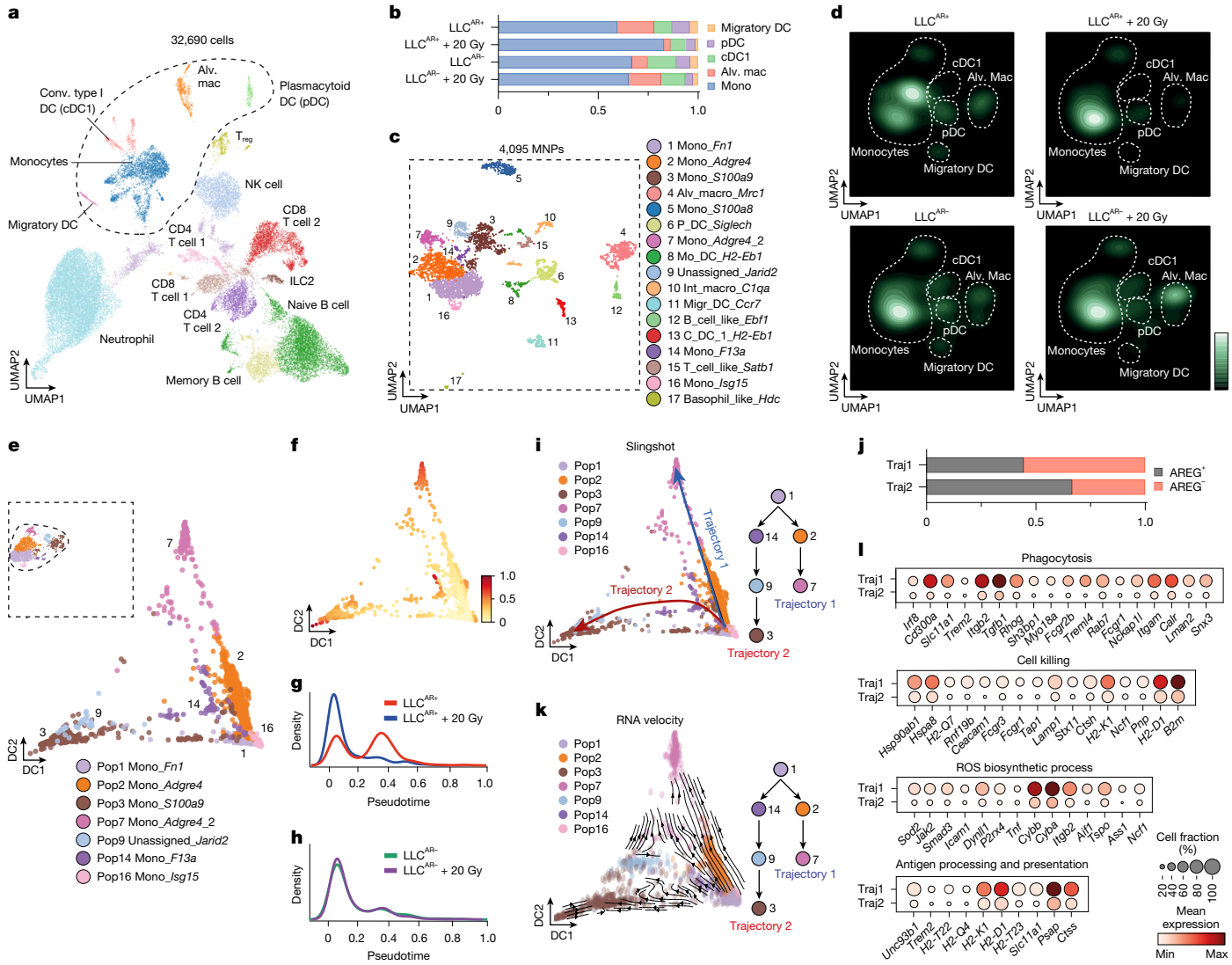



**Fig. 3 | scRNA-seq identifies AREG-dependent changes in MNPs in lung tissue from LLC$^{AR+}$ and LLC$^{AR-}$ tumour-bearing mice post-radiotherapy.** **a**, scRNA-seq and unsupervised uniform manifold approximation and projection (UMAP) clustering of 32,690 live CD45$^+$ cells from lungs of LLC$^{AR+}$ and LLC$^{AR-}$ tumour-bearing mice with or without 20 Gy treatment. $n = 4$ mice per group. Outline indicates MNP clusters. Alv. mac, alveolar macrophage; cDC, conventional type I dendritic cell; ILC2, type 2 innate lymphoid cell; NK, natural killer cell; pDC, plasmacytoid dendritic cell; $T_{reg}$, regulatory T cell. **b**, Quantification of five MNP clusters (outlined in **a**) stratified by experimental group. **c**, UMAP clustering of 4,095 MNPs, identifying 17 subclusters, annotated using Pegasus auto-annotation and the most significantly upregulated differentially expressed gene. Alv_macro, alveolar macrophage; C_DC_1, classical type 1 dendritic cell; Int_macro, interstitial macrophage; Migr_DC, migratory dendritic cell; Mo_DC, monocyte-derived dendritic cell; Mono, monocyte; P_DC, plasmacytoid dendritic cell. **d**, Density plot of 4,095 MNPs stratified by experimental groups. **e**, Diffusion map projection of 2,600 monocytes, using the same cluster colours as in **c**. DC, diffusion component. **f**, Pseudotime diffusion map of 2,600 monocytes. **g**, Density plots across pseudotime for monocytes from AREG-sufficient conditions (LLC$^{AR+}$ and LLC$^{AR+}$ + 20 Gy). **h**, Density plots across pseudotime for monocytes from AREG-deficient conditions (LLC$^{AR-}$ and LLC$^{AR-}$ + 20 Gy). **i**, Slingshot trajectory inference of monocytes on the diffusion map. **j**, Proportion of cells from wild-type (AREG$^+$) and AREG-deficient (AREG$^-$) conditions in trajectories 1 and 2. **k**, RNA velocity vectors of monocytes on diffusion map. **l**, Bubble plot showing differential expression of selected genes related to phagocytosis, cell killing, reactive oxygen species biosynthetic process or antigen processing and presentation of trajectories 1 and 2 (signatures from Wang et al.[29]). Max, maximum; min, minimum.

differentiate into metastasis-associated macrophages[27,28], we investigated their involvement in AREG-dependent lung metastasis growth by single-cell RNA sequencing (scRNA-seq) of immune cells from the lungs of mice bearing LLC$^{AR+}$ and LLC$^{AR-}$ flank tumours five days post-radiotherapy.

Unsupervised clustering of 32,690 CD45$^+$ cells identified 21 clusters from 11 major cell lineages, including five clusters containing 4,095 MNPs (monocytes, alveolar macrophages, conventional type I dendritic cells, plasmacytoid dendritic cells and migratory dendritic cells) (Fig. 3a, Extended Data Fig. 6a–d and Supplementary Table 4). Consistent with our previous results, local irradiation of LLC$^{AR+}$ flank tumours increased the fraction of monocytes in the lung, which was not recapitulated under AREG-deficient conditions (LLC$^{AR-}$ and LLC$^{AR-}$ with 20 Gy treatment) (Fig. 3b). Gene expression analysis of the LLC$^{AR+}$ + 20 Gy monocyte cluster revealed that immunosuppressive (*Lrg1*, *Retnlg* and *Eno1*) and S100 (*S100a9* and *S100a8*) genes were upregulated, and genes involved in inflammation (*Cd36*, *Dock2* and *Aff3*), antigen processing and presentation (*H2-K1*, *H2-Aa* and *Cd83*) and phagolysosomal processes (*Dock10*, *Picalm* and *Satb1*), were downregulated (Extended Data Fig. 6e). By contrast, we observed the opposite pattern in the LLC$^{AR-}$ plus 20 Gy monocyte cluster, in which S100 and immunosuppressive genes (*Cd274*, *Retnlg*, *Fosl1* and *Eif1*) were downregulated

and genes involved in inflammatory (*Cd86* and *Tnfaip8*) and phagolysosomal (*Hexb* and *Cops9*) processes were significantly upregulated (Extended Data Fig. 6f).

Subclustering of MNPs identified 17 populations (Fig. 3c and Supplementary Table 5) with a distinctive shift in the composition of the monocyte clusters post-radiotherapy with $LLC^{AR+}$ and $LLC^{AR+}$ with 20 Gy treatment, which was not observed in corresponding $LLC^{AR-}$ conditions (Fig. 3d and Extended Data Fig. 6g,h). Monocytes from $LLC^{AR+}$ were dominated by population 3 (Mono_*S100a9*), a population that was characterized by high expression of *S100a9*, *S100a8* and *Satb1*. The most abundant cluster in $LLC^{AR+}$ with 20 Gy treatment was population 1, which was also characterized by high expression of S100, immunosuppressive (*Chil3*, *Hp* and *Anxa1*) and tissue-repair genes (*Fn1*, *F13a1* and *Vcan*), as well as a significant downregulation of genes involved in monocyte-to-macrophage differentiation (*Pparg*, *Itgax* and *Ly75*) (Extended Data Fig. 6g–i). MNPs from the lungs of *Areg*-knockout tumour-bearing mice showed a more diverse spread between all clusters and a larger fraction of clusters 4 (Alv_macro_*Mrc1*), 10 (Int_Macro_*C1qa*) and 13 (Class_DC_1_*H2-Eb1*) (Fig. 3d and Extended Data Fig. 6g,h).

To improve our understanding of how tumour-derived AREG affects functionally relevant monocyte differentiation trajectories, we inferred the development of monocyte subclusters by computing a diffusion map and ordering them along a pseudotime axis (Fig. 3e-f and Extended Data Fig. 7a,b,d). Notably, the comparison of pseudotime states under AREG-sufficient conditions showed that a considerable fraction of monocytes from $LLC^{AR+}$ with 20 Gy treatment were arrested at an earlier pseudotime state and less likely to differentiate to later stages (Fig. 3g and Extended Data Fig. 7c). By contrast, *Areg*-knockout cells were more likely to differentiate, measured by progression along pseudotime, and local tumour irradiation did not affect their pseudotime density (Fig. 3h and Extended Data Fig. 7c). Corresponding to the differentiation arrest, we found that the largest fraction of cells in population 1—the population with the lowest pseudotime—was derived from $LLC^{AR+}$ with 20 Gy treatment (Extended Data Fig. 7e). Notably, Pop1_*Fn1* also showed a higher expression of genes associated with EGFR signalling pathways compared with other subpopulations (Extended Data Fig. 7f).

Trajectory inference using Slingshot with population 1 as a starting population predicted two main trajectories: trajectory 1 developed through population 2 to 7, and an alternative trajectory, trajectory 2, moved through populations 14 and 9 instead, ending in population 3 (Fig. 3i). Population 7 was made up of equal parts of cells from all conditions and characterized by high expression of genes involved in inflammatory, phagocytic and antigen processing functions such as *Fcgr4*, *Myo1g* and *Ctsb*. By contrast, population 3 was dominated by monocytes from AREG-sufficient conditions and characterized by high expression of immunosuppressive genes (*Chil3*, *Thbs1*, *Fn1* and *F13a1*) and genes encoding S100 proteins (Extended Data Fig. 7g,h). Correspondingly, cells in both *Areg* wild-type and *Areg*-knockout conditions were equally likely to traverse trajectory 1, while *Areg* wild-type cells preferentially traversed trajectory 2 (Fig. 3j). These findings were reproduced using RNA velocity analysis (Fig. 3k and Extended Data Fig. 7i–l).

Cells following trajectory 1 increasingly expressed macrophage differentiation and function genes along their differentiation trajectory (*Cd68*, *Trem3*, *Csf1r* and *Adgre1*), whereas MNPs in trajectory 2 showed a global downregulation of gene expression, except for genes linked to immunosuppression (*S100a8*, *S100a9*, *Sell* and *Il18rap*) (Extended Data Fig. 7m,n). Further examination of previously published gene signatures involved in anti-tumour functions of MNPs[29] revealed their significant downregulation in trajectory 2 (Fig. 3l), correlating with higher EGFR signalling (Extended Data Fig. 7o). We concluded that the primary route of monocyte differentiation occurred along trajectory 1 and encompassed increasing expression of macrophage markers and gene signatures associated with phagocytosis, antigen processing and inflammatory response. By contrast, in response to tumour-derived AREG, monocytes were more likely to be redirected along an alternative trajectory (trajectory 2), characterized by decreased anti-tumour functions and increased immunosuppression.

The known immunosuppressive functions of monocytes after radiotherapy[30] and their increased presence in the lungs of irradiated $LLC^{AR+}$ tumour-bearing mice (20 Gy) suggested that suppression of the adaptive anti-tumour T-cell response may enable metastatic proliferation under AREG-sufficient conditions. In support of this, we observed an increased expression of immunosuppressive genes in monocytes from lungs of $LLC^{AR+}$ tumour-bearing mice following 20 Gy treatment (Extended Data Fig. 8a) and, correspondingly, a terminally exhausted gene signature of $CD8^+$ T cells, indicative of a decreased proliferative and cytokine production capacity[31] (Extended Data Fig. 8b). RNA sequencing of $Ly6C^+$ MNPs from $EGFR^+$ ($Egfr^{fl/fl}$) and conditionally EGFR-deficient ($LysM^{\Delta Egfr}$; $EGFR^-$) mice co-cultured with $LLC^{AR+}$ and $LLC^{AR-}$ tumour cells (Extended Data Fig. 8c), revealed that tumour cell AREG expression induces an anti-inflammatory transcriptomic state in $EGFR^+$ MNPs. Gene set enrichment analysis (GSEA) identified upregulated pro-inflammatory pathways in $EGFR^+$ MNPs co-cultured with $LLC^{AR-}$ tumour cells compared with those co-cultured with $LLC^{AR+}$ tumour cells (Extended Data Fig. 8d). This effect was further amplified in $EGFR^-$ MNPs, where IFNγ/α responses, inflammatory response and TNFα signalling were the top upregulated pathways in the presence of $LLC^{AR-}$ cells (Extended Data Fig. 8e). Gene signatures related to phagocytosis, cell killing and reactive oxygen species (ROS) biosynthesis[29] showed highest expression in $EGFR^-$ MNPs co-cultured with $LLC^{AR-}$ tumour cells (Extended Data Fig. 8f–h), whereas genes associated with immunosuppression were most highly expressed in $EGFR^+$ MNPs co-cultured with $LLC^{AR+}$ tumour cells (Extended Data Fig. 8g). rAREG further induced a T-cell suppressive phenotype in bone-marrow-derived myeloid cells (BMDM) (Extended Data Fig. 8j).

Despite these findings, antibody-mediated depletion of $CD8^+$ T cells did not eliminate the size difference between $LLC^{AR+}$ and $LLC^{AR-}$ metastases (Extended Data Fig. 8k–m), suggesting that $CD8^+$ T cells are not the primary mediators of metastatic size differences in vivo. We hypothesized that $Ly6C^+$ MNPs are key effector cells. CCR2 antibody[32]-mediated depletion of $Ly6C^+$ MNPs (Extended Data Fig. 9a) did not alter lung metastasis size in $LLC^{AR+}$ tumour-bearing mice, but significantly increased it in mice bearing $LLC^{AR-}$ tumours (Extended Data Fig. 9b–e), indicating that $Ly6C^+$ MNPs have a crucial role in constraining $LLC^{AR-}$ lung metastasis growth.

## AREG suppresses MNP phagocytosis

The phagocytic activity of MNPs has a central role in tumour control, in both tissue-resident and monocyte-derived cells within the lung tumour microenvironment[29,33]. AREG has been implicated in reducing monocytic phagocytosis-induced cell death[34]; however, the effects of tumour cell-derived AREG on the phagocytic capacity of MNPs remain unclear. To investigate this, we utilized a co-culture system in which we observed that BMDM phagocytosed significantly fewer $LLC^{AR+}$ tumour cells compared with $LLC^{AR-}$ tumour cells (Extended Data Fig. 10a,b). This reduced phagocytic activity correlated with a significantly higher expression of the 'don't-eat-me' signal CD47 on $LLC^{AR+}$ tumour cells, as well as a radiotherapy-induced CD47 upregulation, which was absent in $LLC^{AR-}$ tumour cells (Extended Data Fig. 10c,d). Treatment of $LLC^{AR-}$ tumour cells with rAREG increased CD47 protein levels, whereas treatment of $LLC^{AR+}$ with an AREG-targeting antibody (anti-AREG) decreased CD47 levels (Fig. 4a). AREG increases STAT3 phosphorylation in tumour cells[35,36] and STAT3 is known to upregulate *Cd47* by binding to consensus DNA elements in the promoter and intron regions of *Cd47* in lung cancer cells[37]. Correspondingly, treatment with a STAT3 inhibitor[38] (STAT3i) suppressed both rAREG- and radiotherapy-induced *Cd47* upregulation (Extended Data Fig. 10e–g).

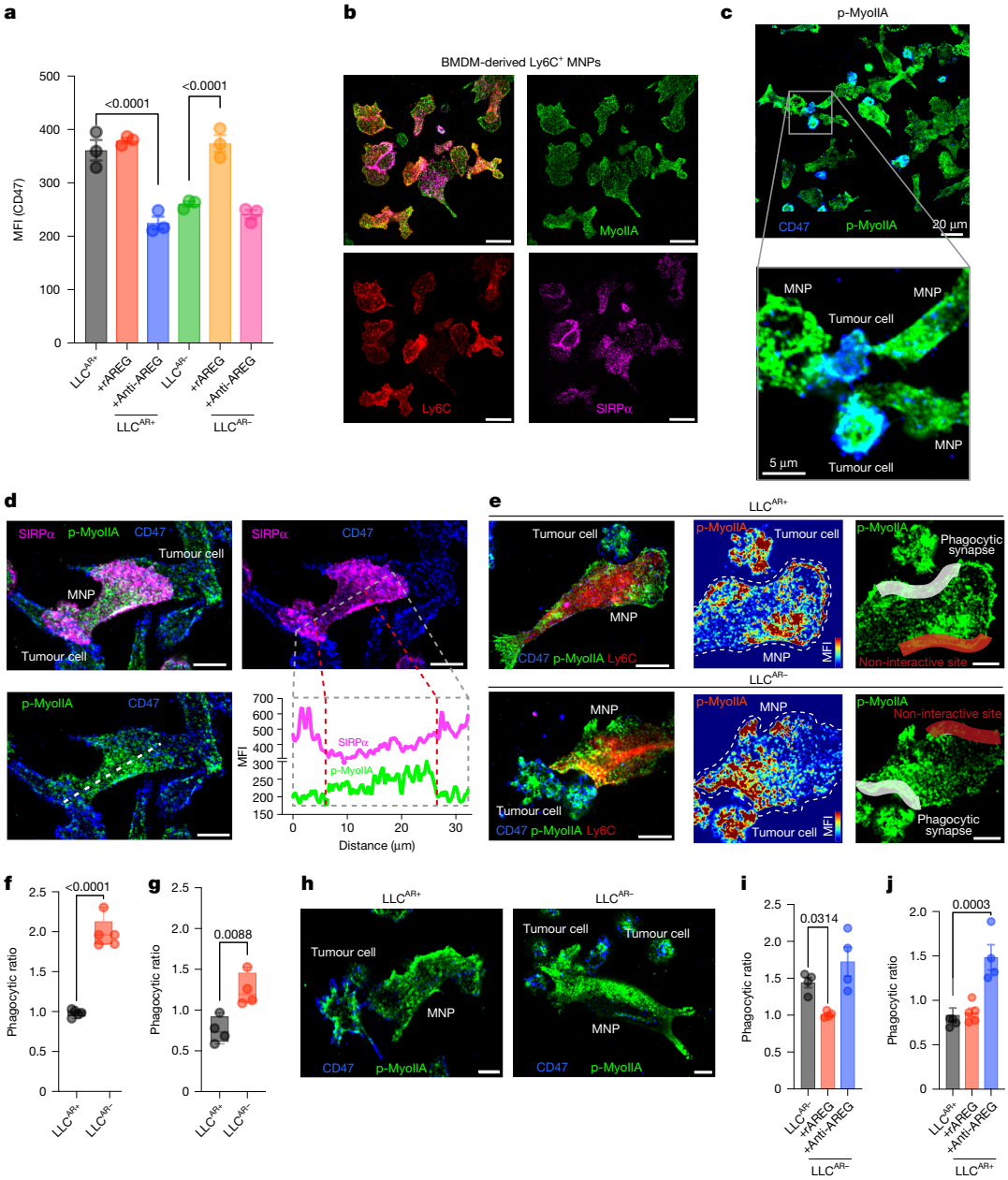



**Fig. 4 | AREG upregulates CD47 in tumour cells resulting in SIRPα-mediated MNP phagocytosis suppression. a**, CD47 MFI in LLC$^{AR+}$ and LLC$^{AR-}$ cells after 48 h treatment with 250 pg ml$^{-1}$ rAREG or 1.5 μg ml$^{-1}$ anti-AREG. $n = 3$ technical replicates. One-way ANOVA, Šídák's test. **b**, Immunofluorescence staining of Ly6C$^+$ MNPs for Ly6C (PE/Dazzle 594, red), MyoIIA (AF488, green) and SIRPα (AF647, magenta). Scale bars, 20 μm. **c**, Immunofluorescence staining of Ly6C$^+$ MNPs co-cultured with LLC cells for p-MyoIIA (AF488, green) and CD47 (BV421, blue). Close-up of phagocytic synapses. **d**, Immunofluorescence staining of Ly6C$^+$ MNPs co-cultured with LLC cells for p-MyoIIA (AF488, green), SIRPα (AF647, magenta), and CD47 (BV421, blue). Bottom right, intensity profile of p-MyoIIA and SIRPα along the grey dashed line representing a Ly6C$^+$ MNP interacting with two tumour cells. Red dashed lines indicate borders of cell–cell contact. Scale bars, 10 μm. **e**, Left, immunofluorescence staining of Ly6C$^+$ MNPs co-cultured with LLC$^{AR+}$ (top) and LLC$^{AR-}$ (bottom) cells, p-MyoIIA (AF488, green), Ly6C (PE/Dazzle 594, red) and CD47 (BV421, blue). Centre, p-MyoIIA MFI heat map of phagocytic synapses. Right, outlines of phagocytic synapses (white) and distant non-interactive sites (red). Scale bars, 10 μm. **f**, Phagocytic ratio of BMDM-derived Ly6C$^+$ MNPs co-cultured with LLC$^{AR+}$ and LLC$^{AR-}$. Unpaired two-sided *t*-test. $n = 5$ technical replicates. **g**, Phagocytic ratio of lung-derived Ly6C$^+$ MNPs co-cultured with LLC$^{AR+}$ and LLC$^{AR-}$. Unpaired two-sided t-test. $n = 4$ technical replicates. **h**, Immunofluorescence staining of lung-derived Ly6C$^+$ MNPs, co-cultured with LLC$^{AR+}$ (top) and LLC$^{AR-}$ (bottom) for p-MyoIIA (AF488, green) and CD47 (BV421, blue). Scale bars, 10 μm. **i**, Phagocytic ratio of Ly6C$^+$ MNPs co-cultured with LLC$^{AR-}$ cells after 48 h treatment with 250 pg ml$^{-1}$ rAREG or 1.5 μg ml$^{-1}$ anti-AREG. One-way ANOVA, Šídák's test. $n = 4$ technical replicates. **j**, Phagocytic ratio of Ly6C$^+$ MNPs co-cultured with LLC$^{AR+}$ cells after 48 h treatment with 250 pg ml$^{-1}$ rAREG or 1.5 μg ml$^{-1}$ anti-AREG. One-way ANOVA, Šídák's test. $n = 4$ technical replicates in anti-AREG group; $n = 5$ technical replicates in LLC$^{AR+}$ and rAREG groups. Data are mean ± s.e.m. In box plots, the centre line shows the median, box edges delineate first and third quartiles, and whiskers show the range of values. One representative experiment out of two independent experiments is shown.

These results suggest that, in addition to its effects on the systemic myeloid immune response, radiotherapy-induced AREG upregulation also promotes phagocytosis resistance of tumour cells by increasing STAT3-mediated CD47 expression.

CD47 inhibits MNP phagocytosis by SIRPα–SHP-1-mediated dephosphorylation of activated myosin-IIA (MyoIIA), reducing actomyosin contractility at the phagocytic synapse[39–41]. We used high-resolution confocal microscopy to assess Ly6C$^+$ MNP phagocytic function by

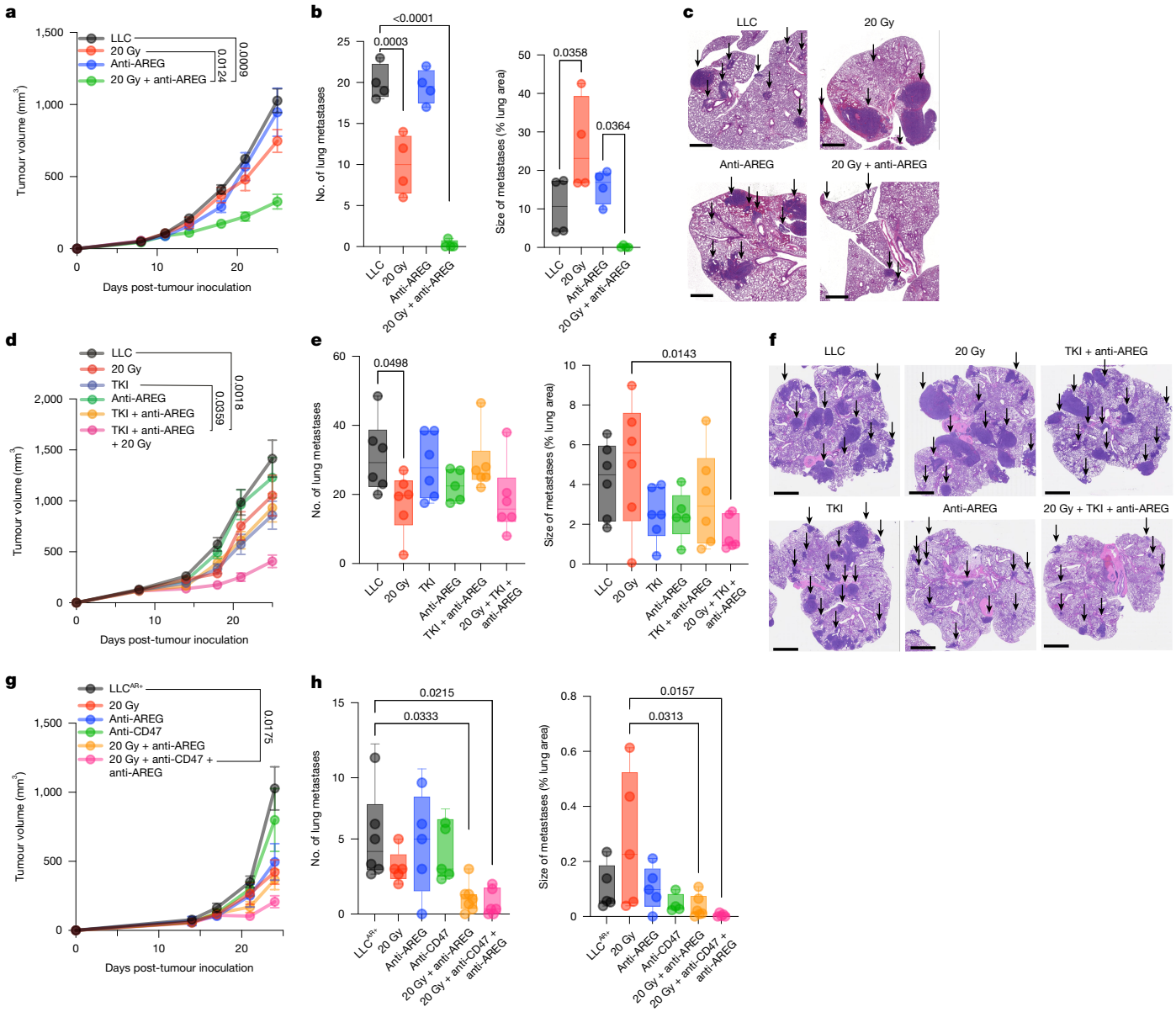



**Fig. 5 | AREG blockade reduces metastasis size in combination with ionizing radiation, EGFR-TKI and anti-CD47 immunotherapy. a**, Growth curve of LLC flank tumours with or without intravenous anti-AREG injection and 20 Gy treatment. $n = 5$ mice per group. Two-way ANOVA, Tukey's test. **b**, Number of lung metastases (left) and mean size of the five largest metastases per lung area (right). $n = 4$ mice per group. One-way ANOVA, Šídák's test. **c**, H&E staining. Black arrows indicate metastatic lesions. Scale bars, 500 µm. **d**, Growth curve of LLC flank tumours with or without intravenous anti-AREG injection, oral EGFR-TKI (Gefitinib) and 20 Gy radiotherapy. $n = 5$ mice in anti-AREG group, $n = 6$ mice in all other groups. Two-way ANOVA, Tukey's test. **e**, Number of lung metastases (left) and mean size of the five largest metastases per lung area (right). $n = 5$ mice in anti-AREG group, $n = 6$ mice in all other groups. One-way ANOVA, Šídák's test. **f**, H&E staining. Black arrows indicate metastatic lesions. Scale bars, 2 mm. **g**, Growth curve of $LLC^{AR+}$ flank tumours with or without intravenous anti-AREG injection, intravenous CD47 antibody and 20 Gy radiotherapy. $n = 4$ mice in $LLC^{AR+}$ group, $n = 5$ mice in all other groups. Two-way ANOVA, Tukey's test. **h**, Number of lung metastases per section (left) and mean size of the five largest metastases per lung area (right). Left to right: $n = 6$, $n = 5$, $n = 5$, $n = 5$, $n = 7$ and $n = 6$ mice per group. One-way ANOVA, Šídák's test. Data are mean ± s.e.m. In box plots, the centre line shows the median, box edges delineate first and third quartiles, and whiskers show the range of values.

visualizing MyoIIA, Ly6C and SIRPα (Fig. 4b). $Ly6C^+$ MNPs co-cultured with LLC tumour cells showed no changes in MyoIIA expression (Extended Data Fig. 10h), but increased levels of the phosphorylated form of MyoIIA (p-MyoIIA) were observed at phagocytic synapses (Fig. 4c). Notably, p-MyoIIA was reduced in MNP-tumour cell contact areas with high SIRPα expression (Fig. 4d), indicating that decreased p-MyoIIA levels reflect local CD47–SIRPα-mediated suppression of phagocytosis. We quantified this suppression by calculating a 'phagocytic ratio': p-MyoIIA fluorescence intensity at the phagocytic synapse compared with a distant membrane section. A phagocytic ratio greater than unity indicated reduced CD47–SIRPα-mediated MyoIIA dephosphorylation and enhanced phagocytic activity. BMDM-derived $Ly6C^+$ MNPs co-cultured with $LLC^{AR-}$ cells showed significantly higher phagocytic ratios than those co-cultured with $LLC^{AR+}$ cells (Fig. 4e,f and Extended Data Fig. 10i), a finding that was confirmed in $Ly6C^+$ MNPs isolated from the lungs (Fig. 4g,h). The phagocytic ratio observed in MNPs co-cultured with $LLC^{AR-}$ cells was significantly decreased after treatment of tumour cells with rAREG, whereas anti-AREG-treatment of $LLC^{AR+}$ cells enhanced the phagocytic ratio of co-cultured MNPs (Fig. 4i,j). These findings demonstrate that AREG signalling upregulates

CD47 on tumour cells, resulting in SIRPα-mediated MyoIIA dephosphorylation and phagocytosis suppression in Ly6C$^+$ MNPs.

## AREG blockade reduces metastasis size

To evaluate the effects of chronic increased systemic AREG in patients, we analysed 42 matched paired serum samples from 21 patients with NSCLC, collected prior to SBRT, as well as after SBRT and three cycles of ICB (from our institutional trial NCT03223155; ref. 25; Supplementary Table 3). We found that reduced serum AREG levels after SBRT and ICB were associated with significantly longer progression-free survival (Extended Data Fig. 11a). Thus, we hypothesized that blocking systemic AREG may improve radiotherapy efficacy and delay tumour progression.

EGFR tyrosine kinase inhibition (EGFR-TKI) has been tested in concurrent and sequential combination with radiotherapy in patients with EGFR-mutant NSCLC with inconsistent results[42–44], and serum AREG levels have been suggested as a predictor of resistance to gefitinib in patients with NSCLC[45]. To evaluate the potential clinical translation of our findings, we treated LLC$^{AR+}$ tumour-bearing mice intravenously with anti-AREG. When combined with anti-AREG, radiotherapy elicited a significant growth delay of flank LLC tumours (Fig. 5a) and the radiotherapy-induced increase in the size of lung metastases was abrogated (Fig. 5b,c). Additionally, EGFR-TKI treatment significantly reduced radiotherapy-induced metastatic growth when combined with anti-AREG (Fig. 5d–f).

Since we observed AREG-induced, CD47–SIRPα-mediated suppression of MNP phagocytosis, we tested whether anti-AREG increased the efficacy of anti-CD47 immunotherapy in combination with radiotherapy. The combination treatment of anti-AREG, anti-CD47 and radiotherapy significantly abrogated LLC$^{AR+}$ flank tumour growth and reduced metastasis size (Fig. 5g,h). Flow cytometry verified a significant increase of Ly6C$^+$ MNP phagocytosis after combination treatment (Extended Data Fig. 11b,c), and a reduction of the radiotherapy-induced increase of p-EGFR$^+$ MNPs in mouse lungs (Extended Data Fig. 12a–i). Therefore, we concluded that AREG blockade abrogates radiotherapy-induced metastatic proliferation while enhancing the efficacy of radiotherapy monotherapy and its combination with EGFR-TKI and anti-CD47 immunotherapy.

## Discussion

Here we find that radiation-induced amphiregulin supports distant metastatic growth by reprogramming p-EGFR$^+$ myeloid cells and suppressing phagocytosis. Of note, radiotherapy-induced AREG and p-EGFR$^+$ MNPs were detected in biopsies, serum and PBMCs of patients with metastatic cancer post-SBRT, findings that were recapitulated in mouse lung metastasis models. These effects were overcome by AREG blockade in mice, thereby inhibiting radiotherapy induction of metastasis growth.

Radiotherapy was first described to increase tumour cell migration, thereby facilitating metastasis in mouse models, by Kaplan et al.[46]. Whereas most investigations have focused on the migratory and invasive potential of metastatic tumour cells[47], we report that local radiotherapy also increases the size of established distant metastases, a clinically relevant mechanism that has garnered less attention. Our results suggest that this mechanism is most pronounced when local tumour control is inadequate, highlighting the need to identify and neutralize metastasis growth-promoting effects of radiotherapy to maximize therapeutic efficacy.

AREG was one of several radiotherapy-inducible genes associated with distant tumour progression in our clinical study. Therefore, we cannot rule out that other soluble factors may be involved in radiotherapy-mediated metastasis proliferation. Here we utilized relatively large radiation doses that are clinically relevant to SBRT. It is unclear whether these effects are observed at smaller doses (2 Gy) used over weeks, as in fractionated radiotherapy; however, the protracted treatment time might also provide more opportunities for identification of factors that potentially limit radiotherapy effectiveness.

Although immune cells other than MNPs may have a role in enhancing metastatic growth, our findings highlight a tumour–AREG–MNP–EGFR signalling loop that enables distant metastasis proliferation following radiotherapy. Tumour-derived AREG induced by distant radiotherapy alters monocyte differentiation in the lung, promoting monocyte arrest at an immature suppressive state, and it induces differentiation along a tumour-tolerogenic trajectory. AREG also modulates immune evasion by upregulating CD47, reducing tumour cell phagocytosis and facilitating tumour cell survival, and AREG blockade enhances anti-CD47 efficacy. CD47 blockade combined with radiotherapy has been shown to elicit a macrophage-mediated abscopal effect in small cell lung cancer (SCLC) models[48]; considered in concert with our findings, this suggests that the distant effects of radiotherapy on tumour growth are in part dependent on phagocytosis. EGFR signalling has been linked to the tumour-promoting roles of MNPs[49], and EGFR-targeted therapies have been shown to mitigate immunosuppression in the tumour microenvironment of inflammatory breast cancer[50]. Notably, AREG has been proposed as a regulator of TAM accumulation in a breast cancer model[51].

Serum AREG concentration has been identified as a predictor of disease progression and progression-free survival in metastatic colorectal cancer and NSCLC[45,52,53], in line with our results of improved progression-free survival in patients with reduced serum AREG levels after SBRT plus ICB. Notably, antibody-mediated targeting of AREG has also shown promising results in decreasing both PD-L1-mediated immunosuppression and chemoresistance in preclinical tumour models[54]. Our data additionally suggest that AREG can modify the treatment response to EGFR-TKI, a finding that has previously been shown to be relevant in patients with NSCLC[45].

We demonstrate that radiation-induced growth factors drive distant metastasis growth in SBRT-treated patients and in mouse models, which leads to shortened survival. We demonstrate that the mechanisms that promote distant metastasis growth post-radiotherapy are targetable, which suggests a clinical trial where adverse factors are assayed shortly after initiation of radiotherapy with or without immunotherapy and neutralized. These results indicate a paradigm shift for the use of radiotherapy in patients with locally advanced and metastatic tumours, leading to a new type of personalized radiotherapy.

## Online content

Any methods, additional references, Nature Portfolio reporting summaries, source data, extended data, supplementary information, acknowledgements, peer review information; details of author contributions and competing interests; and statements of data and code availability are available at https://doi.org/10.1038/s41586-025-08994-0.


1. Weichselbaum, R. R., Liang, H., Deng, L. & Fu, Y. X. Radiotherapy and immunotherapy: a beneficial liaison? *Nat. Rev. Clin. Oncol.* **14**, 365–379 (2017).
2. Orth, M. et al. Current concepts in clinical radiation oncology. *Radiat. Environ. Biophys.* **53**, 1–29 (2014).
3. Lomax, M. E., Folkes, L. K. & O'Neill, P. Biological consequences of radiation-induced DNA damage: relevance to radiotherapy. *Clin. Oncol.* **25**, 578–585 (2013).
4. Lynch, C., Pitroda, S. P. & Weichselbaum, R. R. Radiotherapy, immunity, and immune checkpoint inhibitors. *Lancet Oncol.* **25**, e352–e362 (2024).
5. Liang, H. et al. Host STING-dependent MDSC mobilization drives extrinsic radiation resistance. *Nat. Commun.* **8**, 1736 (2017).
6. Jiménez-Cortegana, C., Galassi, C., Klapp, V., Gabrilovich, D. I. & Galluzzi, L. Myeloid-derived suppressor cells and radiotherapy. *Cancer Immunol. Res.* **10**, 545–557 (2022).
7. Pitroda, S. P., Chmura, S. J. & Weichselbaum, R. R. Integration of radiotherapy and immunotherapy for treatment of oligometastases. *Lancet Oncol.* **20**, e434–e442 (2019).
8. Pointer, K. B., Pitroda, S. P. & Weichselbaum, R. R. Radiotherapy and immunotherapy: open questions and future strategies. *Trends Cancer* **8**, 9–20 (2022).
9. Wang, L. et al. RNA m$^6$A methylation and MDSCs: roles and therapeutic implications for radiotherapy. *Med* **4**, 863–874 (2023).

10. Shoyab, M., Plowman, G., McDonald, V., Bradley, J. G. & Todaro, G. J. Structure and function of human amphiregulin: a member of the epidermal growth factor family. *Science* **243**, 1074–1076 (1989).
11. Shoyab, M., McDonald, V. L., Bradley, J. G. & Todaro, G. J. Amphiregulin: a bifunctional growth-modulating glycoprotein produced by the phorbol 12-myristate 13-acetate-treated human breast adenocarcinoma cell line MCF-7. *Proc. Natl. Acad. Sci. USA* **85**, 6528–6532 (1988).
12. Zaiss, D. M. W. et al. Amphiregulin enhances regulatory T cell-suppressive function via the epidermal growth factor receptor. *Immunity* **38**, 275–284 (2013).
13. Zaiss, D. M. W., Gause, W. C., Osborne, L. C. & Artis, D. Emerging functions of amphiregulin in orchestrating immunity, inflammation, and tissue repair. *Immunity* **42**, 216–226 (2015).
14. Minutti, C. M. et al. Epidermal growth factor receptor expression licenses type-2 helper T cells to function in a T cell receptor-independent fashion. *Immunity* **47**, 710–722.e6 (2017).
15. Busser, B., Sancey, L., Brambilla, E., Coll, J. L. & Hurbin, A. The multiple roles of amphiregulin in human cancer. *Biochim. Biophys. Acta* **1816**, 119–131 (2011).
16. Berasain, C. & Avila, M. A. Amphiregulin. *Semin. Cell Dev. Biol.* **28**, 31–41 (2014).
17. Shao, J. & Sheng, H. Amphiregulin promotes intestinal epithelial regeneration: roles of intestinal subepithelial myofibroblasts. *Endocrinology* **151**, 3728–3737 (2010).
18. Luke, J. J. et al. Safety and clinical activity of pembrolizumab and multisite stereotactic body radiotherapy in patients with advanced solid tumors. *J. Clin. Oncol.* **36**, 1611–1618 (2018).
19. Mulder, K. et al. Cross-tissue single-cell landscape of human monocytes and macrophages in health and disease. *Immunity* **54**, 1883–1900.e5 (2021).
20. Georgiades, P. et al. *vavCre* transgenic mice: a tool for mutagenesis in hematopoietic and endothelial lineages. *Genesis* **34**, 251–256 (2002).
21. Johnstone, C. N. et al. Functional and molecular characterisation of EO771.LMB tumours, a new C57BL/6-mouse-derived model of spontaneously metastatic mammary cancer. *Dis. Model. Mech.* **8**, 237–251 (2015).
22. McElrath, C. et al. Critical role of interferons in gastrointestinal injury repair. *Nat. Commun.* **12**, 2624 (2021).
23. Gilmore, J. L. et al. Amphiregulin-EGFR signaling regulates PTHrP gene expression in breast cancer cells. *Breast Cancer Res. Treat.* **110**, 493–505 (2008).
24. Miyawaki, M. et al. Enhanced phosphorylation of the epidermal growth factor receptor at the site of tyrosine 992 in esophageal carcinomas. *APMIS* **116**, 1097–1106 (2008).
25. Bestvina, C. M. et al. A phase 1 trial of concurrent or sequential ipilimumab, nivolumab, and stereotactic body radiotherapy in patients with stage IV NSCLC study. *J. Thorac. Oncol.* **17**, 130–140 (2022).
26. Van Der Maaten, L. & Hinton, G. Visualizing Data using *t*-SNE. *J. Mach. Learn. Res.* **9**, 2579–2605 (2008).
27. Swirski, F. K., Hilgendorf, I. & Robbins, C. S. From proliferation to proliferation: monocyte lineage comes full circle. *Semin. Immunopathol.* **36**, 137–148 (2014).
28. Noy, R. & Pollard, J. W. Tumor-associated macrophages: from mechanisms to therapy. *Immunity* **41**, 49–61 (2014).
29. Wang, T. et al. Influenza-trained mucosal-resident alveolar macrophages confer long-term antitumor immunity in the lungs. *Nat. Immunol.* **24**, 423–438 (2023).
30. Wang, L. et al. YTHDF2 inhibition potentiates radiotherapy antitumor efficacy. *Cancer Cell* **41**, 1294–1308 (2023).
31. Miller, B. C. et al. Subsets of exhausted $CD8^+$ T cells differentially mediate tumor control and respond to checkpoint blockade. *Nat. Immunol.* **20**, 326–336 (2019).
32. Mack, M. et al. Expression and characterization of the chemokine receptors CCR2 and CCR5 in mice. *J. Immunol.* **166**, 4697–4704 (2001).
33. Lecoultre, M., Dutoit, V. & Walker, P. R. Phagocytic function of tumor-associated macrophages as a key determinant of tumor progression control: a review. *J. Immunother. Cancer* **8**, e001408 (2020).
34. Platen, C., Dreschers, S., Reiss, L. K., Wappler, J. & Orlikowsky, T. W. Amphiregulin regulates phagocytosis-induced cell death in monocytes via EGFR and matrix metalloproteinases. *Mediators Inflamm.* **2018**, 4310419 (2018).
35. Hsu, Y.-L. et al. Lung tumor-associated dendritic cell-derived amphiregulin increased cancer progression. *J. Immunol.* **187**, 1733–1744 (2011).
36. Ebott, J. et al. Enhanced amphiregulin exposure promotes modulation of the high grade serous ovarian cancer tumor immune microenvironment. *Front. Pharmacol.* **15**, 1375421 (2024).
37. Lu, J. et al. Reprogramming of TAMs via the STAT3/CD47-SIRPα axis promotes acquired resistance to EGFR-TKIs in lung cancer. *Cancer Lett.* **564**, 216205 (2023).
38. Schust, J., Sperl, B., Hollis, A., Mayer, T. U. & Berg, T. Stattic: a small-molecule inhibitor of STAT3 activation and dimerization. *Chem. Biol.* **13**, 1235–1242 (2006).
39. Jaiswal, S. et al. CD47 is upregulated on circulating hematopoietic stem cells and leukemia cells to avoid phagocytosis. *Cell* **138**, 271–285 (2009).
40. Oldenborg, P. A., Gresham, H. D. & Lindberg, F. P. CD47-signal regulatory protein α (Sirpα) regulates Fcγ and complement receptor-mediated phagocytosis. *J. Exp. Med.* **193**, 855–862 (2001).
41. Tsai, R. K. & Discher, D. E. Inhibition of 'self' engulfment through deactivation of myosin-II at the phagocytic synapse between human cells. *J. Cell Biol.* **180**, 989–1003 (2008).
42. Ready, N. et al. Chemoradiotherapy and gefitinib in stage III non-small cell lung cancer with epidermal growth factor receptor and KRAS mutation analysis: Cancer and Leukemia Group B (CALEB) 30106, a CALGB-stratified phase II trial. *J. Thorac. Oncol.* **5**, 1382–1390 (2010).
43. Kelly, K. et al. Phase III trial of maintenance gefitinib or placebo after concurrent chemoradiotherapy and docetaxel consolidation in inoperable stage III non-small-cell lung cancer: SWOG S0023. *J. Clin. Oncol.* **26**, 2450–2456 (2008).
44. Wrona, A., Dziadziuszko, R. & Jassem, J. Combining radiotherapy with targeted therapies in non-small cell lung cancer: Focus on anti-EGFR, anti-ALK and anti-angiogenic agents. *Transl. Lung Cancer Res.* **10**, 2032–2047 (2021).
45. Ishikawa, N. et al. Increases of amphiregulin and transforming growth factor-α in serum as predictors of poor response to gefitinib among patients with advanced non-small cell lung cancers. *Cancer Res.* **65**, 9176–9184 (2005).
46. Kaplan, H. S. & Murphy, E. D. The effect of local roentgen irradiation on the biological behavior of a transplantable mouse carcinoma. i. Increased frequency of pulmonary metastasis. *J. Natl Cancer Inst.* **9**, 407–413 (1949).
47. Sundahl, N., Duprez, F., Ost, P., De Neve, W. & Mareel, M. Effects of radiation on the metastatic process. *Mol. Med.* **24**, 16 (2018).
48. Nishiga, Y. et al. Radiotherapy in combination with CD47 blockade elicits a macrophage-mediated abscopal effect. *Nat. Cancer* **3**, 1351–1366 (2022).
49. Lanaya, H. et al. EGFR has a tumour-promoting role in liver macrophages during hepatocellular carcinoma formation. *Nat. Cell Biol.* **16**, 972–981 (2014).
50. Wang, X. et al. EGFR is a master switch between immunosuppressive and immunoactive tumor microenvironment in inflammatory breast cancer. *Sci. Adv.* **8**, eabn7983 (2022).
51. Nickerson, N. K., Mill, C. P., Wu, H. J., Riese, D. J. & Foley, J. Autocrine-derived epidermal growth factor receptor ligands contribute to recruitment of tumor-associated macrophage and growth of basal breast cancer cells in vivo. *Oncol. Res.* **20**, 303 (2013).
52. Chayangsu, C., Khunsri, S., Sriuranpong, V. & Tanasanvimon, S. The correlations between serum amphiregulin and other clinicopathological factors in colorectal cancer. *J. Gastrointest. Oncol.* **8**, 980–984 (2017).
53. Kim, S. A. et al. Amphiregulin can predict treatment resistance to palliative first-line cetuximab plus FOLFIRI chemotherapy in patients with RAS wild-type metastatic colorectal cancer. *Sci. Rep.* **11**, 23803 (2021).
54. Xu, Q. et al. Targeting amphiregulin (AREG) derived from senescent stromal cells diminishes cancer resistance and averts programmed cell death 1 ligand (PD-L1)-mediated immunosuppression. *Aging Cell* **18**, e13027 (2019).

**Publisher's note** Springer Nature remains neutral with regard to jurisdictional claims in published maps and institutional affiliations.

Springer Nature or its licensor (e.g. a society or other partner) holds exclusive rights to this article under a publishing agreement with the author(s) or other rightsholder(s); author self-archiving of the accepted manuscript version of this article is solely governed by the terms of such publishing agreement and applicable law.

© The Author(s), under exclusive licence to Springer Nature Limited 2025, corrected publication 2025

# Methods

### Patient cohort

**Tissue biopsy microarray data.** Patients with advanced metastatic solid tumours were enrolled in a clinical trial between January 2016 and March 2017 (NCT02608385[18]). Clinical characteristics of the patient cohort are provided in Supplementary Table 1. Each patient received SBRT to at least 2 metastases, with doses ranging from 30–50 Gy delivered over 3–5 fractions. Owing to SBRT planning constraints, not all metastases were targeted. Biopsies were collected from the same metastasis site in 11 patients both before and within 7 days after SBRT, totaling 22 samples. Gene expression analysis was conducted as previously described[18,55].

**PBMCs and serum data.** We collected PBMCs and serum from patients enrolled in the COSINR study (NCT03223155[25]). Clinical characteristics of the patient cohort are provided in Supplementary Table 3. This randomized phase 1/2 trial evaluated the safety and efficacy of combining ICB with ipilimumab/nivolumab and SBRT as a first-line treatment for stage IV NSCLC. Patients, regardless of PD-L1 expression or tumour mutational burden, were randomized to receive SBRT to 2–4 metastatic sites, either concurrently (SBRT with immunotherapy) or sequentially (SBRT followed by immunotherapy).

### Detection of genes upregulated after SBRT and correlation with distant metastasis progression

Genes with an absolute delta value change ≥1 between pre- and post-SBRT were selected, and canonical pathways and upstream regulators were predicted using Ingenuity Pathway Analysis (IPA). Statistical significance was determined using Fisher's exact test *P* values, with a *P* value of ≤0.05 considered significant. The post/pre-SBRT gene expression ratio was calculated for each patient. A 95% confidence interval was calculated for each gene across patients, and genes with confidence intervals that did not cross zero were retained for subsequent analyses. Assessment of study endpoints and tumour progression began at the initiation of SBRT, as described in our previous publication[1]. In brief, clinical evaluations were conducted regularly throughout treatment. CT scans were performed after every fourth pembrolizumab cycle or earlier if indicated. Tumour response was assessed per RECIST 1.1[56], summing axial diameters of irradiated and non-irradiated metastases separately. Tumour control was defined as the absence of progressive disease.

### Cell lines

LLC1 (CRL-1642) and EO771-LMB (CRL-3405) cells were obtained from ATCC and maintained according to ATCC characterization protocols. No additional authentication was performed beyond the identity provided by ATCC. Mycoplasma testing was negative. All cell lines were checked for pathogen contamination via Charles River Research Animal Diagnostic Services before use. Mouse tumour cells were cultured in DMEM (Corning), supplemented with 10% fetal bovine serum (FBS) (Sigma), 100 U ml$^{-1}$ penicillin, and 100 μg ml$^{-1}$ streptomycin, under 5% $CO_2$ conditions. To enhance metastatic homing to the lungs, both LLC and EO771-LMB cell lines underwent two consecutive rounds of in vivo passaging via spontaneous lung metastases. For each passage, $10^6$ cells were injected subcutaneously into the flanks of wild-type mice. After 28 days, spontaneous lung metastases were dissected, and metastatic tumour cells were isolated and re-cultured.

After successful in vivo passaging, CRISPR–Cas9-mediated *Areg* depletion was performed using the amphiregulin CRISPR–Cas9 knockout plasmid (m) (Santa Cruz Biotechnology, sc-419185) in combination with the amphiregulin HDR plasmid (m) (Santa Cruz Biotechnology, sc-419185-HDR) according to the manufacturer's protocols. sc-419185: amphiregulin CRISPR–Cas9 knockout Plasmid (m) is a pool of 3 different guide RNA (gRNA) plasmids: gRNA-A: GCCAGAAG GCATTTCGCTTA; gRNA-B: AGGGGACTACGACTACTCAG; gRNA-C: TGCCGATGCCAATAGCTGCG. In brief, tumour cells were seeded in 6-well plates and transfected at 50% confluency using Lipofectamine 3000 (L3000015, ThermoScientific) and Opti-MEM (31985062, Gibco). After 48 h, the transfected cells were selected using 5 μg ml$^{-1}$ of puromycin (P9620, Sigma-Aldrich), and sorted based on RFP-expression using an Aria III cell sorter (BD Biosciences). The resulting *Areg*-knockout and RFP-expressing control cell lines were validated using quantitative PCR with reverse transcription (RT–qPCR) and flow cytometry, as well as mouse AREG ELISA of conditioned cell culture medium and tumour cell lysates.

### In vivo mouse experiments

All mice were maintained under specific pathogen-free conditions and used in accordance with the Institutional Animal Care and Use Committee (IACUC) guidelines. This study was approved by the IACUC of the University of Chicago (ACUP 70931 and 72213). All mice were on a C57BL/6 background. Wild-type C57BL/6 mice were purchased from Harlan Envigo or bred in-house. *Vav*-Cre (B6.Cg-Tg(VAV1-cre)1Graf/MdfJ) mice and *LysM*-Cre (B6.129P2-*Lyz2*$^{tm1(cre)Ifo}$/J) were purchased from The Jackson Laboratory. *Vav*-Cre mice were bred with *Areg*$^{fl/fl}$ mice[57], provided by A. Rudensky, to generate conditional *Areg*-knockout (Vav1$^{\Delta Areg}$) mice. To generate conditional *Egfr*-knockout mice, *LysM*-Cre (B6.129P2-*Lyz2*$^{tm1(cre)Ifo}$/J) from The Jackson Laboratory were bred with *Egfr*-floxed mice (*Egfr*$^{fl/fl}$)[58], provided by D. Tilley. For tumour studies, 8- to 10-week-old female C57BL/6 (wild-type) mice were used. In studies involving conditional knockout mice, age- and sex-matched littermates served as controls. Mice were housed under a 12-h light:dark cycle, at 19–22 °C with 30–70% humidity.

### In vivo flank tumours

To generate flank tumours, $1 \times 10^6$ tumour cells were injected subcutaneously into the flank in 100 μl serum-free DMEM. Tumour volumes were measured along three orthogonal axes ($a$, $b$, $c$) and calculated as: tumour volume = $a \times b \times c/2$.

### In vivo irradiation of flank tumours

Once flank tumours reached 150–200 mm$^3$, mice were assigned to treatment groups in a way that ensured similar average tumour sizes across groups. Irradiation was administered using a Philips RT-250 X-ray generator (250 kVp, 15 mA, 1.0 mm copper filter, 156 cGy/min dose rate). The generator was regularly calibrated using a Farmer-type ionization chamber to ensure accurate dose delivery. Film dosimetry in a water phantom was performed to assess dose distribution, with films placed at varying depths to establish the dose gradient and verify dose uniformity. Results confirmed tumour site dose delivery with minimal variation.To minimize irradiation exposure to healthy tissue, mice were anaesthetized by intraperitoneal injection of 90–120 mg ketamine and 5–10 mg xylazine per kg body weight and then fully shielded with lead, leaving only the flank tumour exposed. For hindlimb irradiation in non-tumour-bearing mice, the right hindlimb was exposed to the radiation beam while the rest of the body was shielded with lead.

### Intravenous lung metastasis model

One-hundred thousand LLC$^{AR+}$ and LLC$^{AR-}$ tumour cells were injected in 100 μl serum-free DMEM via retro-orbital intravenous injection under continuous inhalative anaesthesia. Mice were euthanized 7 and 14 days post-injection and lungs were removed.

### Orthotopic lung cancer model and CT-guided irradiation

A total of $0.8 \times 10^4$ LLC$^{AR+}$ and LLC$^{AR-}$ tumour cells were injected percutaneously into the right lung in a total volume of 4 μl (2 μl serum-free DMEM + 2 μl growth factor reduced Matrigel (356231, Corning)) under continuous inhalative anaesthesia. Orthotopically implanted lung tumours were visualized using contrast-enhanced conebeam computed tomography (CBCT) on an X-RAD 225 Cx (Precision X-ray),

building on previously published protocols[59,60]. In brief, a CBCT scan was acquired under continuous inhalative anaesthesia using 360 projection images (1° per image), with X-ray tube settings of 60 kV, 0.8 mA, and a 1.0 mm aluminium filter. To enhance soft tissue contrast, 300 µl iomeron-400 were injected intravenously 2 min prior to CBCT acquisition. Iomeron-400 was provided by R. Fretta. Orthotopic lung tumour sizes were measured by manually outlining contrast-enhancing tumour areas using Horos (Version 3.3.6), and CT-guided irradiation was delivered once tumours reached a mean size of 10–20 $mm^3$, using two opposing beams (0° and 180°) with a 3 × 3 mm collimator, at X-ray tube settings of 220 kV, 13 mA and a 0.15 mm copper filter. The isocentre of the radiation beam was aligned to the centre of the contrast-enhanced tumour volume.

### In vivo treatments

Anti-AREG antibody (AF989, R&D Systems) was administered intravenously once every 3 days at a dose of 1.5 µg $ml^{-1}$ blood volume for four doses, starting on the day of radiotherapy. Anti-CD47 antibody (IAP, BE0270, BioXcell) was administered intravenously once every 3 days at a dose of 200 µg per mouse for four doses, starting on the day of radiotherapy. Recombinant AREG (989-AR-100/CF, R&D Systems) was administered intravenously once every 2 days at a dose of 50 pg per ml blood volume for eight doses, starting on day 5. Gefitinib (Iressa, ZD1839, Selleckchem) was administered orally by gavage at a dose of 75 mg $kg^{-1}$ body weight for 15 doses, starting on day 5. Rat IgG2a (BE0089, BioXcell) or goat IgG (BE0130, BioXcell) were used as isotype controls and administered every three days at 200 µg per dose, for four doses each, starting on the day of radiotherapy.

### Study endpoints

All mice used in this study were monitored at regular intervals and euthanized before reaching humane experimental endpoints, as defined in the ACUP protocols 70931 and 72213, approved by the IACUC of the University of Chicago. Mice were removed from the study if any subcutaneous tumour exceeded 20 mm in diameter or if a significant decline in body condition score (BCS) were observed. For orthotopic lung tumour and intravenous lung metastasis models, mice were removed if BCS worsened significantly. These criteria were not exceeded in any of the experiments performed for this study.

### In vitro reagents and treatments

For STAT3 inhibitor treatment, $LLC^{AR+}$ cells were seeded and allowed to attach overnight before treatment with STAT3 inhibitor (Stattic, S7024, Selleckchem) at a concentration of 5 µM for 12 h, before RNA was collected using RNeasy Microkit (74136, Qiagen) for RT–qPCR.

For IFNβ treatment, $LLC^{AR+}$ cells were seeded and allowed to attach overnight before treatment with recombinant Mouse IFNβ1 (carrier-free) (581302, BioLegend) at a concentration of 100 ng $ml^{-1}$ for 3 and 12 h before RNA was collected using the RNeasy Microkit(Qiagen) for RT–qPCR, or at concentrations of 50, 100 and 200 ng $ml^{-1}$ for 24 h before protein was collected for ELISA.

For experiments involving siSTAT2, Accell Mouse Stat2 (20847) siRNA - SMARTpool (E-049890-00-0010, Horizon Discovery) was used, which consists of a pool of 4 siRNAs targeted at *Stat2*: (1) 5′-CGA UAAAGUCGAAAUCUAC-3′; (2) 5′-GCUUCAGAUACACAGUUUU-3′; (3) 5′-GAACUUAGCUAUUUUAUUA-3′; and (4) 5′-CCAGCAGCUUGA GAUUGAA-3′. $LLC^{AR+}$ cells were transfected with siRNA for 72 h before verifying knockdown efficiency. Cells were re-seeded and allowed to attach overnight before irradiation with 4 Gy. RNA was collected 12 h after irradiation using RNeasy Microkit (Qiagen) for RT–qPCR, and protein was collected 24 h after irradiation for ELISA.

### In vitro irradiation of tumour cells

For in vitro irradiation of tumour cells, the same settings were used as described under 'In vivo irradiation of flank tumours'.

### BMDM generation

Bone marrow cells from non-tumour-bearing mice were isolated by flushing femurs and tibias with RPMI-1640 supplemented with 10% fetal bovine serum (FBS) and 1% penicillin-streptomycin. Red blood cells were lysed using ammonium-chloride-potassium (ACK) lysis buffer (A1049201, Gibco), and the remaining cells were filtered through a 40 µm filter. Cells were resuspended at a density of $1 \times 10^6$ cells per ml and cultured in complete RPMI-1640 medium (11875-093, Gibco) with recombinant mouse GM-CSF (20 ng $ml^{-1}$) (576308, BioLegend). Fresh culture medium was added on day 3 and cells were used for downstream experiments on day 4.

### T-cell suppression assay

Splenic T cells from non-tumour-bearing wild-type mice were isolated using the EasySep Mouse T Cell Isolation Kit (19851, STEMCELL Technologies) following the manufacturer's instructions and stained with 1 µM CellTrace Violet (C34557, ThermoFisher) in PBS for 20 min at 37 °C, then resuspended in R10 media + IL-2 at a final concentration of 50 U $ml^{-1}$ (212-12, PeproTech). Two-hundred thousand T cells were seeded into wells of a 96-well round-bottom plate, with 50,000 BMDMs pre-treated for 24 h with 50 and 100 ng $ml^{-1}$ recombinant mouse AREG (989-AR-100, R&D systems). CD3/CD28 Dynabeads (11452D, Gibco) were included in stimulated wells at a 1:1 T cell:bead ratio. After 2 days, 100 µl of medium was replaced with fresh medium containing IL-2. T cells and monocytes were co-cultured for four days, and T-cell proliferation was analysed by flow cytometry.

### Clonogenic assay

One-hundred tumour cells per well were seeded in six-well plates and allowed to adhere overnight. The next day, cells were irradiated with 2, 4, 6 or 8 Gy or treated with 0, 62.5, 125, 250, 500 or 1,000 pg $ml^{-1}$ rAREG. Plates were maintained for 7–10 days, with medium and the corresponding treatment refreshed every 72 h. Colonies were then fixed in 100% ice-cold methanol, stained with crystal violet, and manually counted.

### AREG ELISA

We collected serum from patients enrolled in the concurrent and sequential arms of the COSINR study (NCT03223155)[3] and measured serum AREG levels using the Human Amphiregulin ELISA kit (EHAREG, Invitrogen) according to the manufacturer's instructions. A total of 42 matched serum samples from $n = 21$ patients were collected before SBRT and on day 1 of ipilimumab/nivolumab cycle 3 (typically 70–80 days after treatment initiation).

For the mouse AREG ELISA, blood samples were collected from tumour-bearing and non-tumour-bearing mice by retro-orbital bleeding on days 1, 3, and 5 post-radiotherapy. Flank tumour samples were collected on day 5 post-radiotherapy, weighed, and homogenized. Similarly, muscle and skin samples were collected from the irradiated hindlimb of non-tumour-bearing mice on day 5 post-radiotherapy, weighed, and homogenized. All samples were centrifuged at 4 °C for 15 min at 10,000*g* to remove cells and debris. AREG concentrations in tissue supernatants and serum were measured using the mouse Amphiregulin DuoSet ELISA Kit (DY989, R&D Systems) according to the manufacturer's protocol.

### In vitro live-cell imaging

The Incucyte live-cell analysis system (EssenBioscience/Sartorius) was used for live-cell imaging experiments. For cell proliferation assays, cells were plated at 20% confluency, and confluence was measured every 60–120 min for 46-72 h. For irradiation experiments, cells were allowed to attach overnight before irradiation with 2, 4, or 6 Gy. For scratch-wound assays, cells were grown to confluency in 96-well plates, and wounds were generated using the 96-Well WoundMaker (Sartorius). Wells were imaged every 60–120 min at 10× magnification until

full confluency was reached. For co-culture assays, tumour cells and BMDMs were stained for 30 min with CellTracker Red (CMTPX) and CellTracker Green (CMFDA) dye, respectively. Ten thousand BMDMs were co-plated with $0.5 \times 10^4$ tumour cells for 48 h and imaging was performed using 10× objectives with phase contrast and the fluorescent channels green (excitation 441–481 nm/emission 503–544 nm) and red (excitation 567–607 nm/emission 622–704 nm). Data were collected using Incucyte Base software (v2019A) and tumour cell–MNP interactions were quantified using the Cell Counter plugin of ImageJ (1.54g), by manually counting green MNPs in direct contact with a red tumour cell.

### In vitro analysis of phagocytic ratio

BMDMs were generated as described in 'BMDM generation'. BMDMs were then isolated by negative selection using the EasySep Monocyte Isolation Kit (19861, StemCell Technologies) according to the manufacturer's instructions. For the isolation of lung-resident monocytes, mice were perfused with 10 ml ice-cold PBS, lungs were removed, minced, and digested in 1 mg ml$^{-1}$ collagenase IV and 200 µg ml$^{-1}$ DNase I at 37 °C for 45 min on a shaker at 150 rpm. Red blood cells were lysed using ACK cell lysis buffer (A1049201, Gibco), and cells were filtered, washed, and isolated using the EasySep Monocyte Isolation Kit. The isolated cells were then cultured in GM-CSF-supplemented RPMI for 4 days as described above (BMDM generation).

BMDMs and lung monocytes were seeded at 30,000 cells per well onto poly-L-lysine-coated (P4707, Sigma) 8-well glass-bottom slides (80827, Ibidi), and treated overnight with 1 µg ml$^{-1}$ polyinosinic-polycytidylic acid (Poly-IC, HY-107202, MedChemExpress). LLC$^{AR+}$ and LLC$^{AR-}$ cells, untreated or pre-treated with 250 pg ml$^{-1}$ recombinant AREG or 1.5 µg ml$^{-1}$ anti-AREG antibody for 24 or 48 h, were grown to 80% confluence, detached, and seeded at 30,000 cells per well overnight. The following day, tumour cells were detached and seeded on adherent BMDMs (or vice versa) at 30,000 cells per well, allowing for 3 h of interaction at 37 °C. After 2.5 h, cells were stained at 1:100 dilution with anti-mouse Ly6C (PE/Dazzle 594, 128044, BioLegend), anti-mouse CD47 (BV421, 127527, BioLegend), and anti-mouse SIRPα (Alexa Fluor 647, 144028, BioLegend) for 30 min, then fixed, and permeabilized with 4% PFA and 0.5% Triton X-100. Following PBS washes, cells were blocked with 5% BSA, stained with primary antibodies for phospho-MyoIIA (Ser19, 3671, Cell Signaling, 1:100) or MyoIIA (3403, Cell Signaling, 1:100) for 30 min, followed by secondary anti-rabbit AF488 (A32731, Invitrogen) at 2 µg ml$^{-1}$ in 1% BSA.

Cells were visualized using a SoRa Subdiffraction Marianas Spinning Disk Confocal microscope with a 40× or 63× NA 1.0 objective. Ly6C$^+$ MNPs within 10 µm of tumour cells were assessed for their phagocytic ratio, calculated by comparing the MFI of p-MyoIIA at the phagocytic synapse to that of distant membrane sections for MNPs located within 10 µm of a tumour cell. A phagocytic ratio >1 indicated reduced MyoIIA dephosphorylation at the MNP membrane regions most closely co-localized with tumour cells.

### Transwell migration assay

A single-cell suspension of tumour cells ($10^3$ cells per insert) was added to the upper compartment of inserts with 8 µm pores (3422, Corning) in serum-free medium. The same growth medium, containing 10% FCS, was added to the bottom chamber. After overnight incubation, wells were gently washed with PBS, and migrated cells were fixed with 70% methanol for 10 min, stained with 0.05% crystal violet, and cells in the mesh were counted using the Cellcounter plugin in ImageJ (1.54g).

### RNA extraction and quantitative real-time polymerase chain reaction (qRT-PCR)

RNA was extracted using the RNeasy Micro Kit (74136, Qiagen) according to the manufacturer's protocols. DNA was synthesized using the High-Capacity cDNA Reverse Transcription Kit (4368814, Applied Biosystems). Real-time PCR was performed with SYBR Green PCR Master Mix (4309155, Applied Biosystems), and results were normalized to GAPDH. Relative gene expression was calculated using the $2^{-\Delta\Delta CT}$ method. Primer sequences: *Areg* (forward: GGTCTTAGGCTCAGG CCATTA; reverse: CGCTTATGGTGGAAACCTCTC), and *Cd47* (forward: CATGGCCCTCTTCTGATTTC; reverse: GGAGGTTGTATAGTCTTC TGATTGG).

### Histology

**H&E staining for lung metastasis quantification.** Mouse lung tissues were fixed in 4% paraformaldehyde for a minimum of 24 h and processed at The University of Chicago HTRC core facility for embedding, sectioning, and H&E staining. Slides were scanned using a CRi Panoramic SCAN 40× Whole Slide Scanner. Lung metastases were analysed using QuPath (v0.3.0). Metastases were manually annotated using the 'wand' tool, and the mean size of the three to five largest metastatic lesions per lung was calculated. Metastasis size was normalized to the total lung area present on the slide. Two to three sections per lung were analysed, with sections spaced 300 µm apart.

**Immunofluorescent staining.** Lungs from LLC flank tumour-bearing mice treated with 0, 5, 10 or 20 Gy radiotherapy were collected at the experimental endpoint, fixed in 4% paraformaldehyde for 24 h, then paraffin-embedded, and sectioned at The University of Chicago HTRC core facility. Slides were heated to 55 °C for 45 min, deparaffinized with two 2-min xylene washes, followed by graded ethanol washes (100%, 90%, 75%, and 30%) and $ddH_2O$. Antigen retrieval was performed by incubating slides at 90 °C in antigen retrieval buffer (10% glycerol, 10% 10× citrate buffer, and 80% $ddH_2O$) for 45 min, cooling to room temperature, and rinsing with $ddH_2O$. Tissues were blocked in 5% BSA for 45 min in a humidity chamber before staining.

Primary antibodies (p-EGFR, Tyr992, 44786 G, Invitrogen; Ly6C-PE/Dazzle 594, HK1.4, 128044, BioLegend) were applied at a 1:100 dilution in 1% BSA, and slides were incubated overnight at 4 °C. After washing, slides were incubated with secondary anti-rabbit AF488 antibody (A32731, Invitrogen) at 1:500 in 1% BSA for 1 h at room temperature. Following a $ddH_2O$ wash, slides were treated with the TrueVIEW Autofluorescence Kit (Vector, SP8400) as per protocol, quenched for 2 min, rinsed, and stained with 1 µg ml$^{-1}$ DAPI for 10 min, followed by washing. Slides were then mounted in Vectashield Vibrance Antifade Mounting Medium (H-1800-10, Vector), and lung metastases were imaged using a SoRa Subdiffraction Marianas Spinning Disk Confocal microscope with a 40× NA 1.0 objective.

**Tissue-specific AI cell segmentation for the detection of p-EGFR$^+$ Ly6C$^+$ MNPs.** A custom tissue-specific AI-based cell segmentation model was developed using the human-in-the-loop pipeline of Cellpose[61,62] (2.0) to analyse images of immunofluorescently stained lung sections. The full code is available on Github (https://github.com/apiffko/IF.mono.quantif). In brief, segmentation masks were generated to classify individual cells within the tissue using a custom Python classification pipeline. For each segmented cell, morphological features and intensity distributions across different regions of the cell were extracted. A logistic regression classifier was then trained on these features, using manually identified Ly6C$^+$ MNPs as ground truth, to differentiate Ly6C$^+$ MNPs from Ly6C$^-$ cells. A cut-off value for classification was determined by maximizing the Youden's J index in the learning cohort[63]. The fraction of Ly6C$^+$ MNPs was calculated by normalizing the detected MNP count to the total tissue area (in µm$^2$), derived from the cytoplasmic channel using Otsu's thresholding[64] and the image's physical dimensions extracted from metadata.

### Flow cytometry

**Mouse lungs.** Mice were euthanized, and lungs were perfused and/or repeatedly washed with PBS to minimize peripheral blood contamination. Lungs were minced and digested with 1 mg ml$^{-1}$ collagenase

IV (C4-22-1G, Sigma-Aldrich) and 200 μg ml$^{-1}$ DNase I (04536282001, Millipore Sigma) at 37 °C for 45-60 min on a shaker at 150 rpm. For some experiments, cells were then pelleted by centrifugation at 400*g* for 10 min and further purified with 40 and 70% Percoll (GE) solutions by centrifuging at 800*g* (no brake) for 20 min at room temperature. Non-tumour cells were collected from the interface. Red blood cells were lysed using ACK lysis buffer (A1049201, Gibco). The resulting cell suspensions were filtered through 70-μm cell strainers. Samples were then washed with PBS and incubated with Zombie NIR (BioLegend, 423105) or LIVE/DEAD yellow (L34959, Invitrogen) fixable viability dye (1:2,000) for 10 min at 4 °C. Fc blocking was performed using anti-FcR (2.4G2, CP025, BioXcell, 1:100). For extracellular staining, surface marker antibodies were added in staining buffer (PBS with 2% FBS and 0.5 mM EDTA (324506, Millipore Sigma)) at a 1:200 dilution. For intracellular staining, cells were fixed and permeabilized using the BD Cytofix/Cytoperm solution (554722, Fisher Scientific) for 60 min at 4 °C and maintained in BD Perm/Wash buffer (BDB554723, Fisher Scientific) per the manufacturer's instructions, followed by incubation with intracellular antibodies (1:100 dilution, 30 min, 4 °C). Flow cytometry data was acquired using a 5-laser Cytek Aurora, collected with SpectroFlo (3.3.0) and analysed with FlowJo (v10.8.1, BD Biosciences).

The following flow cytometry antibodies were used at a dilution of 1:200: CD45 (30-F11), and FoxP3 (MF-14) from eBioscience or Invitrogen; CD11b (M1/70), CD11c (N418), CD4 (GK1.5), CD8a (53-6.7), NK1.1 (PK136), CD3 (17A2), F4/80 (BM8), Ly6C (HK1.4), MHCII (M5/114.15.2), PD-1 (29 F.1A12), PD-L1 (10F9G2), NK1.1 (PK136), CD206 (C068C2), CCR7 (4B12), CD19 (6D5) and Tyr705 STAT3 Phospho (13A3-1) from BioLegend; and Ly6G (1A8), NK1.1 (PK136), CD8 (53-6.7) and F4/80 (T45-2342) from BD Biosciences.

**Human PBMCs.** PBMCs were collected before and after SBRT from patients in the COSINR trial[3]. To isolate the effects of SBRT, only patients from the sequential study arm (SBRT followed by immunotherapy) were included. PBMCs were thawed in warm RPMI + 10% FCS, centrifuged, and washed with PBS before processing, as described above.

The following human flow cytometry antibodies were used at a dilution of 1:200: FOXP3 (236 A/E7), CD20 (2H7), and CD16 (eBioCB16) from Invitrogen; CD4 (SK3), CCR7 (G043H7), PD-1 (EH12.2H7), PD-L1 (B7-H1), HLA-DR (L243), CD11c (3.9), CD303 (BDCA-2), CD304 (12C2), CD1c (L161), CD71 (CY1G4), and CD45RA (HI100) from BioLegend; and CD56 (NCAM16.2), CD141 (1A4), CD45 (HI30) from BD, CD3 (UCHT1), CD33 (WM53) and CD8a (SK1) from ThermoFisher.

**Conjugation of p-EGFR and AREG antibodies.** For AREG and p-EGFR staining, phospho-EGFR (Tyr992) polyclonal antibodies (44-786 G, ThermoFisher) or AREG antibodies (AF989, R&D Systems) were conjugated using LYNX rapid antibody conjugation kits (LNK082C/LNK142PERCPCY5.5, Bio-Rad) and used at a dilution of 1:200.

### Unsupervised clustering analysis of flow cytometry data

CD45$^+$ cells ($1 \times 10^4$ to $0.5 \times 10^5$ cells per sample) were concatenated and used for downstream analysis. FlowJo plugins for Phenograph v2.4[65] and FlowSOM v3.0.18[66] were used for unsupervised nearest-neighbour clustering based on phenotypic similarities. High-dimensional data was visualized using *t*-SNE in FlowJo 10.8.1 (BD). The FlowJo plugin Cluster explorer v.1.7.4 was used for cluster visualization and marker expression mapping on t-SNE plots.

### Bulk RNA sequencing of tumour cells and Ly6C$^+$ MNPs

LLC$^{AR+}$ cells were cultured in vitro for 24 h and treated with 4 Gy irradiation at 50% confluency. RNA was collected 12 h post-irradiation from three technical replicates of each condition (LLC$^{AR+}$ and LLC$^{AR+}$ + 4 Gy). For co-culture experiments, bone-marrow-derived myeloid cells were generated from EGFR$^+$ and EGFR$^-$ mice as described in 'BMDM generation' and co-cultured with LLC$^{AR+}$ or LLC$^{AR-}$ tumour cells at a 5:1 ratio for 24 h. Cells were subsequently stained as described above (flow cytometry) and Ly6C$^+$ MNPs were sorted by an Aria III cell sorter (BD Biosciences) in three technical replicates each. RNA was extracted and purified using the RNeasy Kit (Qiagen) according to the manufacturer's instructions. cDNA library preparation and RNA sequencing were performed by the genomics core facility at The University of Chicago using a NovaSeqX (Illumina). The raw sequence reads (110 bp, paired-end) ranged from ~22 to 36 million per sample, and the data have been deposited in NCBI Gene Expression Omnibus (GEO) under accession number GSE291151.

Raw data quality control was performed using FastQC, and reads were filtered to retain those with an average quality score >30. Reads passing QC were mapped to the mouse reference genome (mm10) using STAR (2.7.10b), and a gene expression matrix with read counts was generated using Subread (2.0.5). Differentially expressed genes (DEGs) were identified using the Bioconductor package DESeq2 (1.46.0), with a false discovery rate (FDR) threshold of <0.1, applying the Wald test and Benjamini-Hochberg correction. GSEA was performed using GSEA (4.3.2).

### scRNA-seq

LLC$^{AR+}$ and LLC$^{AR-}$ flank tumour-bearing mice were treated with 20 Gy once tumours reached 150–200 mm$^3$. Mice were euthanized and lung tissues were collected 5 days post-radiotherapy. Single-cell suspensions were obtained by tissue digestion, and live CD45$^+$ cells were sorted using an Aria III cell sorter (BD Biosciences) (see 'Flow cytometry' for staining details). Purified live CD45$^+$ cells were stained with Total Seq Hashtag antibodies (B0301, B302, B303, and B0304; 155831, 155833, 155835 and 155837, BioLegend). Pre-processing viability of sorted cells was verified using Trypan blue staining. For each biological condition (LLC$^{AR+}$, LLC$^{AR+}$ + 20 Gy, LLC$^{AR-}$ and LLC$^{AR-}$ + 20 Gy), four mice were pooled, and Gene Expression (GEX) and Hashtag Oligo (HTO) libraries were generated and demultiplexed based on TotalSeq hashtag antibody labelling by the genomics core facility at The University of Chicago. Paired GEX and HTO libraries were aligned using cellranger count (Cellranger version 7.1.0 from 10X genomics) with the 'include-introns' option enabled. Alignment rates for all four conditions ranged from 91–94% to the mm10-2020A mouse reference genome. Barcode processing, filtering, UMI counting, and aggregation of sequencing run aggregation were performed using Cellranger (version 7.1.0, 10X genomics). Downstream analyses were performed in Python using Pegasus (version 1.8.1)[67], scanpy (version 1.8.1)[68] and Seurat (version 4.4.0)[69].

Gene expression data for all four biological conditions were pooled into a single Pegasus Unimodal object, and a multi-step quality control approach was used. Two metrics were assessed for each cellular barcode: (1) total number of genes detected; and (2) proportion of mitochondrial UMIs (mito fraction). Cells with <200 genes detected or a mito fraction >20% were excluded as low-quality or dying cells. HTO counts were normalized using centred log-ratio transformation and demultiplexing was performed using the HTODemux() function in the Seurat R package and by setting the positive.quintile parameter to 99. All cells with >6,000 genes detected or multiple HTO barcodes identified by the HTO classifier were considered multiplets and were filtered out, yielding a final dataset of 32,690 CD45$^+$ cells.

To assess technical variability between mice, dimensionality reduction was performed using principal components analysis (PCA). Using the elbow method, the first 50 principal components were selected. A mouse-level *t*-SNE projection was created by averaging the *t*-SNE coordinates of all cells from each single mouse to visualize global transcriptomic shifts between biological conditions. Next, a multi-step approach to clustering cells for cell-type identification was taken in the 32,690 CD45$^+$ cells using the Pegasus package. First, 18,931 robust genes were identified based on expression in at least 5% of all cells in our dataset. Gene expression counts were normalized by scaling counts so that each cell had the same total gene count ($10^5$), followed by log-transformation.

Then, genes were ranked as 'highly variable' based on having moderate mean expression but high dispersion (computed via the loess smoothing method) using Pegasus. Data dimensionality of the dataset was reduced by selecting the top 4000 most highly variable, robust genes. Next, PCA was performed on this dimensionally reduced transcriptome and top 50 principal components were used for downstream analysis. Batch correction was performed using run_harmony, which implements the Harmony algorithm[70], using the top 50 principal components as inputs and batch parameter set to the HTO barcode variable, which maps a unique barcode to each individual mouse in the experiment. A *k*-nearest-neighbour (kNN) graph was constructed, where each cell's 30 nearest neighbours were calculated. Unsupervised clustering was performed using the Leiden algorithm[71] (resolution = 0.8), resulting in 21 cell clusters of 11 major lineages. UMAP was used to visualize clusters. Cluster-specific gene markers were identified using the Mann–Whitney *U* test, comparing gene expression in the cluster of interest against all others ($q$ value <0.05). Cell-type labels were assigned by a combination of manual curation and auto-annotation tools in Pegasus.

For MNP-focused analyses, MNP clusters (4,095 cells) were selected and the clustering pipeline (PCA, kNN, Leiden with resolution = 0.8) was repeated, yielding 17 MNP clusters. Marker genes were identified using Mann–Whitney *U* tests ($q$ value <0.05). Biological condition-specific MNP densities were visualized by calculating the kernel density estimate of the UMAP embedding using the kdeplot function from the Python seaborn library with thresh = 0 and levels = 15. For monocyte differentiation trajectory analysis, 2,600 monocytes were manually selected from MNP clusters, and their developmental relationships were examined using diffusion mapping (top 100 diffusion components) in Pegasus (default parameters were used). Pseudotime analysis was performed in Pegasus to estimate differentiation progression. The top 10 diffusion components were used as input into the Slingshot R package[72] (3.1.8) to infer lineage trajectories. The slingshot function and getLineages were applied with default parameters, setting monocyte population 1 as the starting point.

For RNA velocity analysis, spliced/unspliced mRNA fractions were calculated using Velocyto (version 0.17.17)[73]. RNA velocities for the 2,600 manually selected MNPs were computed using scVelo (0.3.2)[74]. The top 4,000 genes were selected, and moments were calculated using 30 principal components and 15 nearest neighbours. The dynamical model was used to infer the full transcriptional dynamics of splicing kinetics.

For comparison of monocyte gene expression (individual markers or gene signatures), we applied a more stringent cut-off and filtered out cells with mito_fraction > 5. Gene signature calculations were performed using manual literature-curated signatures, as well as Reactome[75] gene sets. Single-cell signature scoring was performed using a bin-based gene-scoring methodology[76], in which all genes are categorized into 50 bins, and the weighted sum of normalized gene counts was calculated for each gene signature. The final gene signature score was determined by subtracting a weighted sum of 1,000 randomly generated null signatures, ensuring minimal impact from technical variability while amplifying biological signals.

### TCGA data analysis

TCGA data was obtained and analysed using the Xena Platform[77] (https://xena.ucsc.edu/). For the analysis of the LUSC cohort, samples were filtered to include only primary tumours from patients who had received radiotherapy. Gene expression levels were stratified into high and low expression groups, defined as the top (high) versus bottom (low) quartile. Survival outcomes were compared between these groups, and statistical significance was calculated using the ggsurvplot function in R (4.3).

### Statistics and reproducibility

For bar graphs, data are presented as mean ± s.e.m., with individual data points displayed. For box plots, the box represents quartile 1 (25th percentile) to quartile 3 (75th percentile), the line indicates the median (50th percentile), and whiskers denote the minimum and maximum values, with individual data points displayed. Statistical outliers were identified by applying the ROUT method ($Q$ = 10%) in Prism 10.3.1 (GraphPad Software). Sample sizes for each experiment were determined based on pilot studies, prior experience with the experimental models, or literature precedent to ensure adequate statistical power. Normality testing was performed using either the D'Agostino-Pearson or Shapiro–Wilk test, depending on sample size.

Unpaired Student's *t*-test was used to compare means between two independent groups (for example, knockout versus control) when data followed a normal distribution. If normality assumptions were not met, a Mann–Whitney *U* test was applied. All *t*-tests shown in the manuscript were two-sided.

One-way ANOVA was applied for comparisons between more than two groups when data followed a normal distribution, with Tukey's, Šídák's or Dunnett's multiple comparison correction. For non-parametric data, a Kruskal–Wallis test with Dunn's multiple comparison test was used.

Ordinary two-way ANOVA was used for analysing tumour growth curves over time, incorporating both treatment effects and time points. Šídák's multiple comparisons test was applied when comparing two groups at individual time points, while Tukey's or Dunnett's multiple comparisons test was used for multiple group comparisons. If the data were not parametric or contained missing values (for example, if a mouse had been euthanized), a mixed-effects model with the Geisser–Greenhouse correction and Tukey's multiple comparisons test was performed.

**Survival analysis.** Kaplan–Meier survival analysis was conducted, with significance assessed using the log-rank (Mantel–Cox) test.

*P* values are reported in the figures and legends where appropriate. Key in vitro and in vivo experiments were performed at least twice independently with similar results.

### Reporting summary

Further information on research design is available in the Nature Portfolio Reporting Summary linked to this article.

## Data availability

The scRNA-seq data have been deposited at the Gene Expression Omnibus (GEO) under accession GSE250375. The bulk RNA-sequencing data have been deposited at the GEO under accession GSE291151. The microarray data of the patients with advanced solid tumours enrolled in the clinical trial (ClinicalTrials.gov ID: NCT02608385[1]) are available from the corresponding author upon reasonable request. The human LUSC genomic and clinical data were derived from the TCGA Research Network (http://cancergenome.nih.gov) using the Xena platform (https://xena.ucsc.edu/). Publicly available datasets used: mouse reference genome (mm10-2020A): https://www.ncbi.nlm.nih.gov/grc/mouse, Reactome: https://reactome.org/ and Molecular Signature Database: https://www.gsea-msigdb.org/gsea/msigdb/index.jsp. All data supporting the findings of this study are available within the Article and its Supplementary Information. Source data are provided with this paper.

## Code availability

The code used for the custom tissue specific AI-based cell segmentation model is available on Github (https://github.com/apiffko/IF.mono.quantif) and has been archived on Zenodo (https://doi.org/10.5281/zenodo.14982759 (ref. 78)).

55. Luke, J. J. et al. Improved survival associated with local tumor response following multisite radiotherapy and pembrolizumab: secondary analysis of a phase I trial. *Clin. Cancer Res.* **26**, 6437–6444 (2020).

56. Eisenhauer, E. A. et al. New response evaluation criteria in solid tumours: revised RECIST guideline (version 1.1). *Eur. J. Cancer* **45**, 228–247 (2009).
57. Arpaia, N. et al. A distinct function of regulatory T cells in tissue protection. *Cell* **162**, 1078–1089 (2015).
58. Lee, T.-C. & Threadgill, D. W. Generation and validation of mice carrying a conditional allele of the epidermal growth factor receptor. *Genesis* **47**, 85–92 (2009).
59. Doki, Y. et al. Mediastinal lymph node metastasis model by orthotopic intrapulmonary implantation of Lewis lung carcinoma cells in mice. *Br. J. Cancer* **79**, 1121–1126 (1999).
60. Wang, L. M. et al. Validation of an orthotopic non-small cell lung cancer mouse model, with left or right tumor growths, to use in conformal radiotherapy studies. *PLoS ONE* **18**, e0284282 (2023).
61. Stringer, C., Wang, T., Michaelos, M. & Pachitariu, M. Cellpose: a generalist algorithm for cellular segmentation. *Nat. Methods* **18**, 100–106 (2021).
62. Pachitariu, M. & Stringer, C. Cellpose 2.0: how to train your own model. *Nat. Methods* **19**, 1634–1641 (2022).
63. Youden, W. J. Index for rating diagnostic tests. *Cancer* **3**, 32–35 (1950).
64. Otsu, N. A threshold selection method from gray-level histograms. *IEEE Trans. Syst. Man Cybern.* **9**, 62–66 (1979).
65. Levine, J. H. et al. Data-driven phenotypic dissection of aml reveals progenitor-like cells that correlate with prognosis. *Cell* **162**, 184–197 (2015).
66. Van Gassen, S. et al. FlowSOM: using self-organizing maps for visualization and interpretation of cytometry data. *Cytometry A* **87**, 636–645 (2015).
67. Li, B. et al. Cumulus provides cloud-based data analysis for large-scale single-cell and single-nucleus RNA-seq. *Nat. Methods* **17**, 793–798 (2020).
68. Wolf, F. A., Angerer, P. & Theis, F. J. SCANPY: large-scale single-cell gene expression data analysis. *Genome Biol.* **19**, 15 (2018).
69. Satija, R., Farrell, J. A., Gennert, D., Schier, A. F. & Regev, A. Spatial reconstruction of single-cell gene expression data. *Nat. Biotechnol.* **33**, 495–502 (2015).
70. Korsunsky, I. et al. Fast, sensitive and accurate integration of single-cell data with Harmony. *Nat. Methods* **16**, 1289–1296 (2019).
71. Traag, V. A., Waltman, L. & van Eck, N. J. From Louvain to Leiden: guaranteeing well-connected communities. *Sci. Rep.* **9**, 5233 (2019).
72. Street, K. et al. Slingshot: cell lineage and pseudotime inference for single-cell transcriptomics. *BMC Genomics* **19**, 477 (2018).
73. La Manno, G. et al. RNA velocity of single cells. *Nature* **560**, 494–498 (2018).
74. Bergen, V., Lange, M., Peidli, S., Wolf, F. A. & Theis, F. J. Generalizing RNA velocity to transient cell states through dynamical modeling. *Nat. Biotechnol.* **38**, 1408–1414 (2020).
75. Gillespie, M. et al. The reactome pathway knowledgebase 2022. *Nucleic Acids Res.* **50**, D687–D692 (2022).
76. Yang, Y. & Li, B. A streamlined method for signature score calculation. *GitHub* https://github.com/lilab-bcb/pegasus/blob/master/signature_score.pdf (2025).
77. Goldman, M. J. et al. Visualizing and interpreting cancer genomics data via the Xena platform. *Nat. Biotechnol.* **38**, 675–678 (2020).
78. ldonle & apiffko. apiffko/IF.mono.quantif: IF.mono.quantif (v.1.0.0). *Zenodo* https://doi.org/10.5281/zenodo.14982760 (2025).



**Acknowledgements** The authors thank A. Arina, C. Maire, M. F. Allega and A. J. Bilecz for scientific discussions and input; J. Wang, X. Huang and R. Torres for technical assistance; and A. K. Huser for editing the manuscript. Research reported in this publication was supported in part by grants from the Ludwig Foundation, the Chicago Tumor Institute, by the National Cancer Institute (NCI) of the National Institutes of Health (NIH) under Award Numbers U54CA274291 and R01CA262508 to R.R.W., as well as by generous gifts from Mr. and Mrs. V. Foglia and the Foglia foundation, Mr. and Mrs. D. Kozin and Mr. and Mrs. J. Weichselbaum. The content is solely the responsibility of the authors and does not necessarily represent the official views of the National Institutes of Health. A. Piffkó and J.H. are recipients of a Walter Benjamin scholarship provided by the German Research Foundation (Deutsche Forschungsgemeinschaft (DFG); A. Piffkó, 455353745; J.H., 459327389). A. Panda was supported by a T32GM007281/GM/NIGMS grant. J.B. was supported by a Clinical Therapeutics Training Grant (T32GM007019) and a NIH/NCI grant (K12CA139160). E.L. is supported by a NIH/NCI R35 CD264619. R.S.R. was supported by NIH/NIGMS R01 GM149073. We acknowledge technical support from the University of Chicago Human Tissue Resource Center (RRID:SCR_019199), Animal Studies Core (P30CA014599), Microscopy Core (P30CA014599), Cellular Screening Core (RRID:SCR_017914), Functional Genomics Core (P30CA014599, RRID:SCR_019196), and Flow Cytometry Core (P30CA014599, RRID: SCR_017760). Grant numbers: Ludwig Center for Metastasis Research, Chicago Tumor Institute, Ludwig Foundation, NIH/NCI U54CA274291 and NIH/NCI R01CA262508 (R.R.W.); Walter Benjamin scholarships: German Research Foundation (Deutsche Forschungsgemeinschaft (DFG)) 455353745 (A. Piffkó) and 459327389 (J.H.); NIH/NCI R35 CA264619 (E.L.), T32GM007281 (A. Panda); NIH Clinical Therapeutics Training Grant T32GM007019 and NIH/NCI grant K12CA139160 (J.B.); and NIH/NIGMS R01 GM149073 (R.S.R.). Technical support was provided through resource core funding: University of Chicago Human Tissue Resource Center SCR_019199; Animal Studies Core SCR_021806; Microscopy Core SCR_019197; Cellular Screening Core SCR_017914; Functional Genomics Core SCR_019196 and Flow Cytometry Core SCR_017760.


**Author contributions** A. Piffkó, K.Y., Y.F., H.L.L. and R.R.W. conceived the study. A. Piffkó, K.Y. and H.L.L. designed the experiments. A. Piffkó, K.Y., K.T., J.H., E.Z.N., C.W., D.C., Y.F., J.B. and L.W. performed the experiments. A. Piffkó, K.Y. and L.W. prepared samples for scRNA-seq, which A. Panda analysed with support from A. Piffkó and K.Y. J.B., L.D. and K.Z. performed additional data analysis. K.T. performed confocal microscopy under supervision from R.S.R., A. Piffkó, K.Y., J.H., K.T. and S.P.P. analysed experimental data. H.L.L., E.L., D.G.T., S.J.C., E.E.V., R.S.R., M.M., C.H. and R.R.W. contributed resources. A. Piffkó, K.Y., S.P.P., H.L.L. and R.R.W. drafted and finalized the manuscript with input from all other authors.

**Competing interests** R.R.W. has stock and other ownership interests with Boost Therapeutics, Immvira, Reflexion Pharmaceuticals, Coordination Pharmaceuticals, Magi Therapeutics and Oncosenescence. He has served in a consulting or advisory role for Aettis, Astrazeneca, Coordination Pharmaceuticals, Genus, Merck Serono S.A., Nano proteagen, NKMax America and Shuttle Pharmaceuticals. He has a patent pending entitled '*Methods and Kits for Diagnosis and Triage of Patients with Colorectal Liver Metastases*' (PCT/US2019/028071). He has received research grant funding from Varian and Regeneron. He has received compensation including travel, accommodations, or expense reimbursement from Astrazeneca, Boehringer Ingelheim and Merck Serono S.A. C.H. has stock and other ownership interests with Accent Therapeutics and Aferna Green. C.H. is a scientific advisory board member of Aferna Green and Rona Therapeutics. A. Panda has consulted for Related Sciences/Danger Bio and owns equity in Danger Bio. E.L. receives research funding to study the biology of ovarian cancer from AbbVie through The University of Chicago that is unrelated to this work. A patent application has been submitted by A. Piffkó, H.L.L., S.P.P. and R.R.W and is pending at the date of publication. The other authors declare no competing interests.

**Additional information**

**Supplementary information** The online version contains supplementary material available at https://doi.org/10.1038/s41586-025-08994-0.

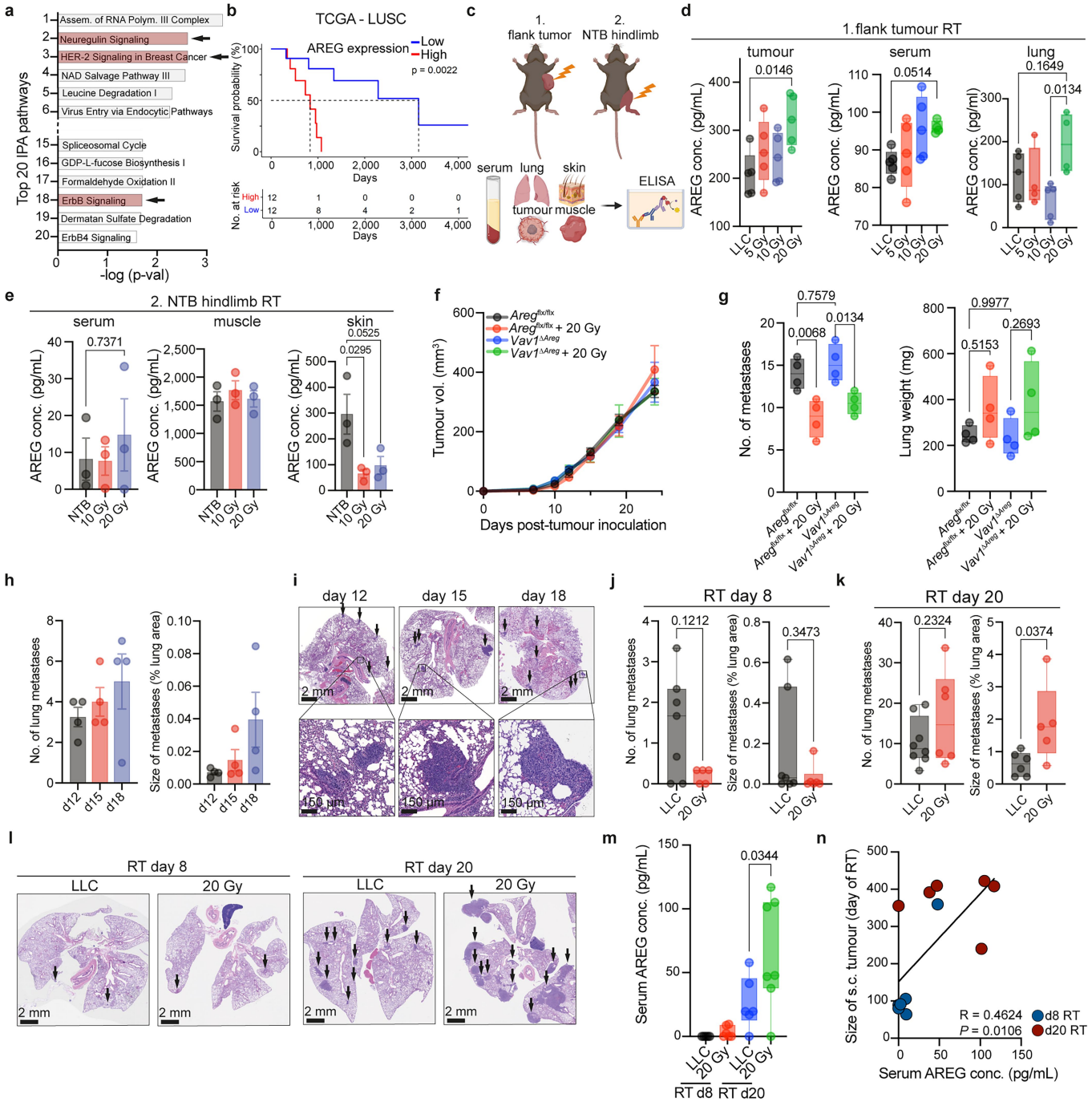

**Correspondence and requests for materials** should be addressed to Ralph R. Weichselbaum.



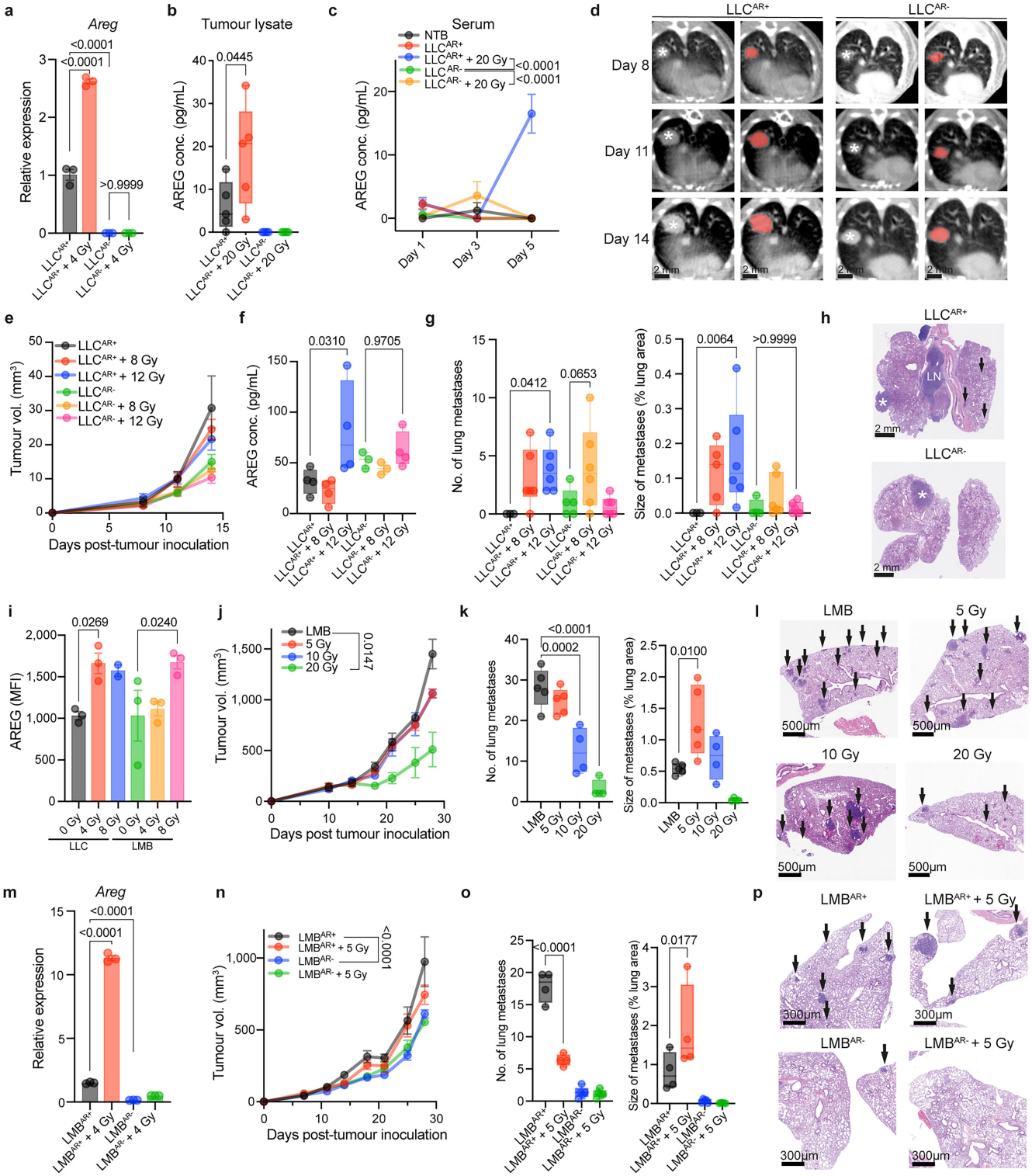
**Peer review information** *Nature* thanks Leila Akkari and the other, anonymous, reviewer(s) for their contribution to the peer review of this work.



**Reprints and permissions information** is available at http://www.nature.com/reprints.

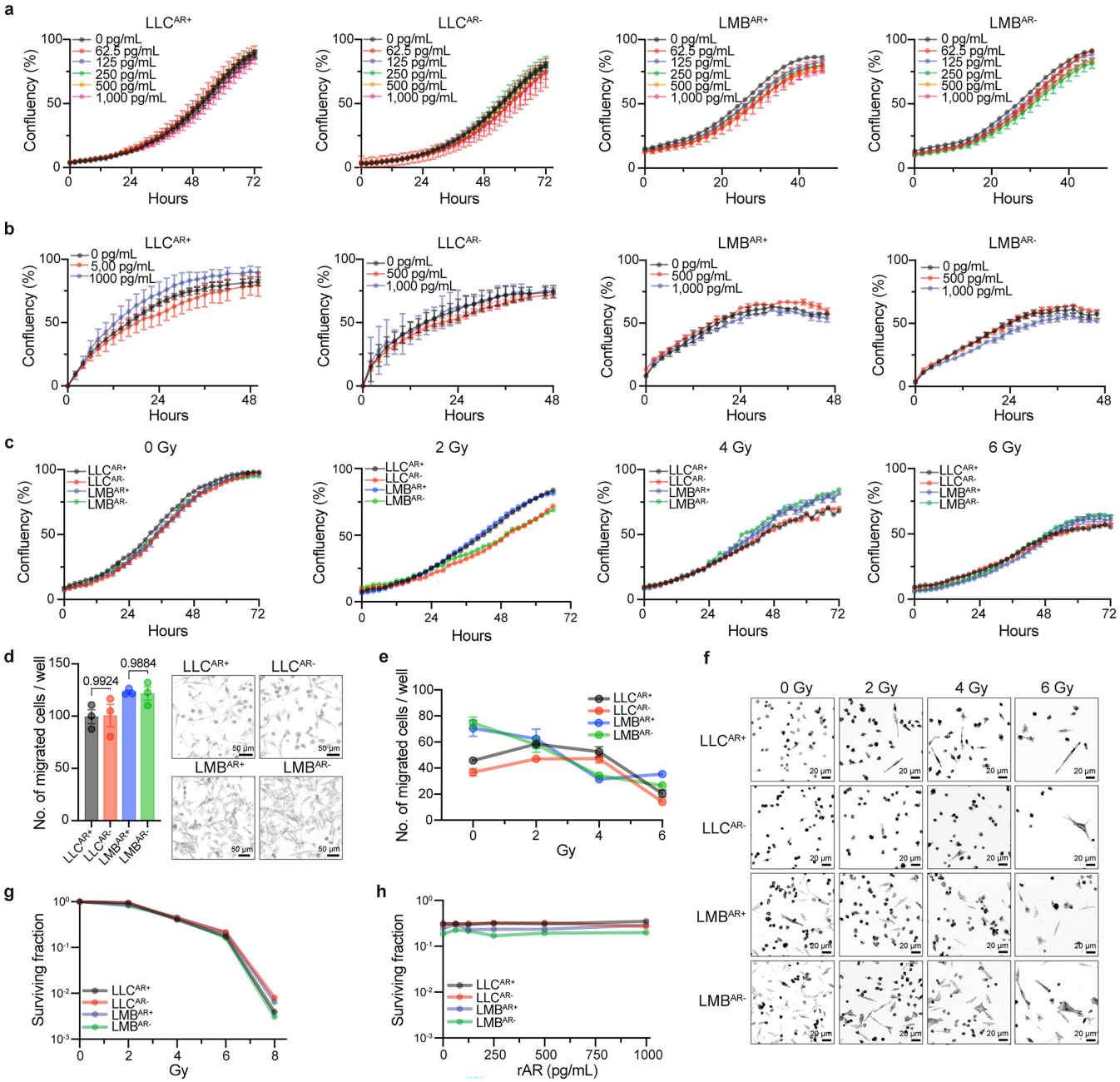



**Extended Data Fig. 1 | Characterization of LLC lung metastasis model reveals dose-dependent AREG secretion from tumour tissue following RT.** **a**, Top 20 RT-induced pathways correlated with distant metastasis progression in patients (Ingenuity Pathway Analysis); pathways including *AREG* are highlighted in red. **b**, Kaplan-Meier survival curves of The Cancer Genome Atlas (TCGA) lung squamous cell carcinoma (LUSC) patients undergoing RT, stratified by tumour AREG expression. Log-rank (Mantel-Cox) test. **c**, Experimental setup: RT applied to either LLC flank tumours (1), or a non-tumour bearing (NTB) hindlimb (2). Serum, lung, skin, tumour and muscle tissues were collected five days post-RT for AREG quantification by ELISA. Created in BioRender (Piffkó, A. (2025) https://BioRender.com/t23f494). **d**, AREG concentration in tumour (left), serum (centre), and lung (right) of LLC tumour-bearing mice five days post-RT, measured by ELISA, $n = 5$ mice per group. One-way ANOVA, Šídák's test. **e**, AREG concentration in serum (left), muscle (centre), and skin (right) of non-tumour-bearing mice five days after RT of the hindlimb, measured by ELISA, $n = 3$ mice per group. One-way ANOVA, Šídák's test. **f**, Growth curve of LLC flank tumours ± 20 Gy in Vav1$^{\Delta Areg}$ and *Areg*$^{flx/flx}$ mice, $n = 4$ mice *in Areg*$^{flx/flx}$, $n = 5$ in all others. **g**, Number (left) of macroscopic metastases and weight of lungs (right) in Vav1$^{\Delta Areg}$ and *Areg*$^{flx/flx}$ mice, $n = 4$ mice per group. One-way ANOVA, Šídák's test. **h**, Number of lung metastases (left), and mean size of the five largest metastases per lung area (right) on days 12, 15, and 18 following subcutaneous LLC tumour injection, $n = 4$ mice per group. **i**, H&E staining. Black arrows indicate metastatic lesions. **j**, Number of lung metastases (left), and mean size of the five largest metastases per lung area (right) of day 8 RT group, $n = 7$ mice per group. Two-sided Mann-Whitney test. **k**, Number of lung metastases (left), and mean size of the five largest metastases per lung area (right) of day 20 RT group, $n = 8$ mice in LLC group, $n = 6$ in 20 Gy group. Unpaired two-sided t-test. **l**, H&E staining. Black arrows indicate metastatic lesions. **m**, Serum AREG-concentration post-RT, measured by ELISA at indicated timepoints, (from left to right; $n = 5$, $n = 6$, $n = 7$, $n = 7$ mice per group). One-way ANOVA, Šídák's test. **n**, Linear regression of serum AREG concentration (pg/mL) five days post-RT vs. flank tumour size at RT. blue = d8 RT, red = d20 RT. Pearson's R and *P* values shown. Data are shown as mean ± SEM; box plots show median (Q2), Q1–Q3, and whiskers (min–max).

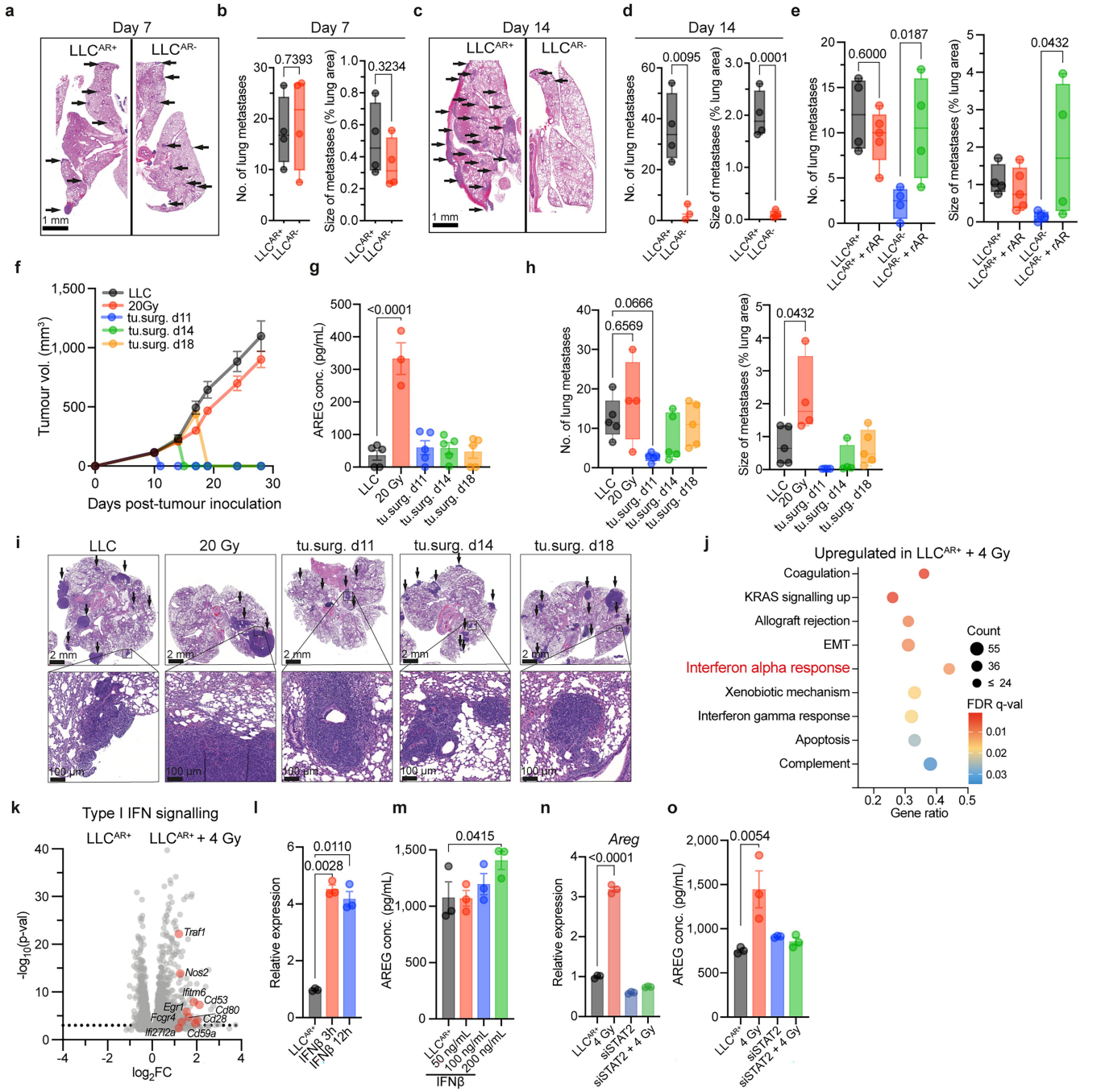



**Extended Data Fig. 2** | See next page for caption.

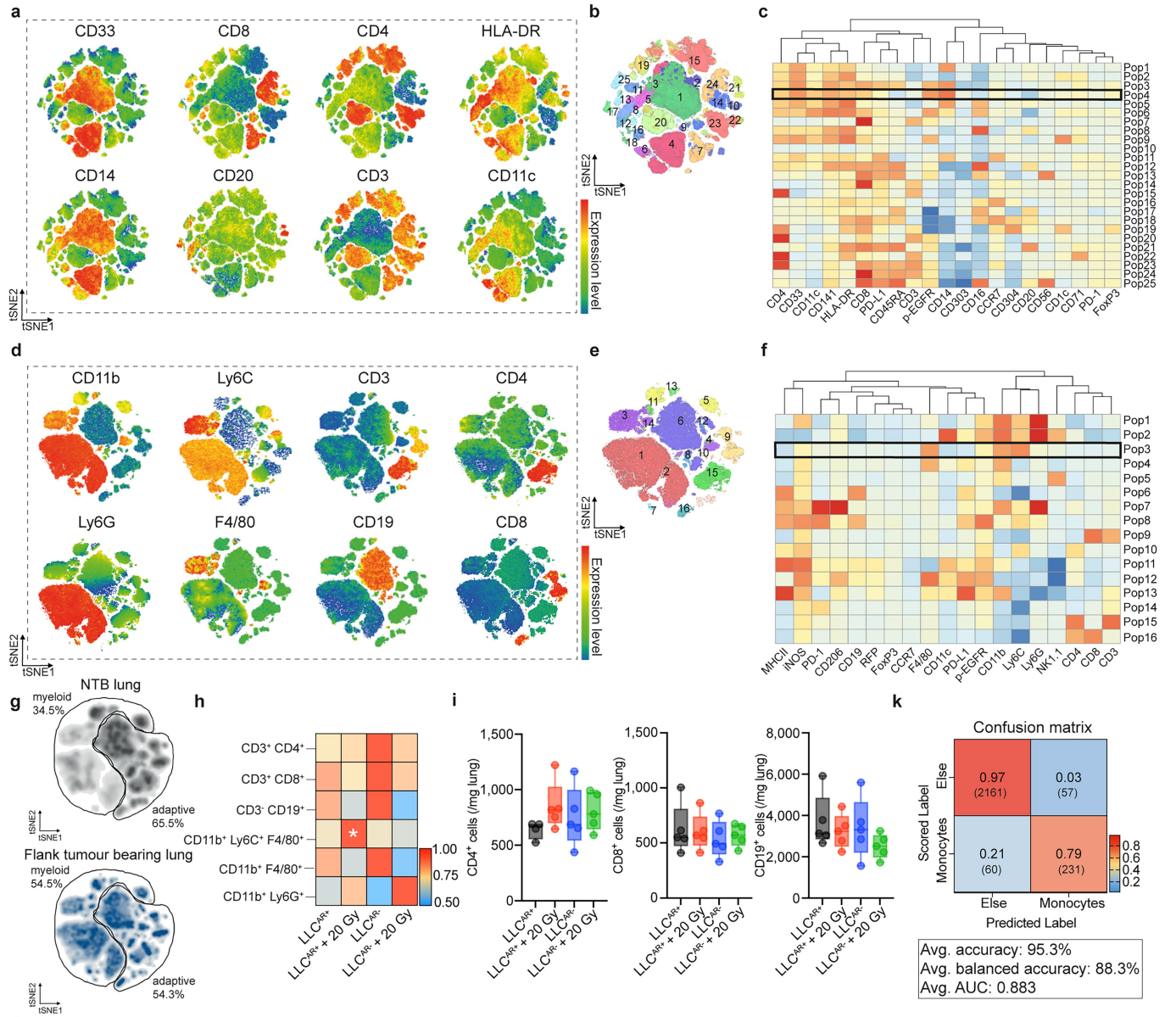
**Extended Data Fig. 2 | Characterization of spontaneously metastatic orthotopic lung LLC and subcutaneous EO771 – LMB models. a**, *Areg* upregulation in $LLC^{AR+}$ and $LLC^{AR-}$ cells after 4 Gy RT in vitro, measured by RT-qPCR 3 h post-RT. One-way ANOVA, Šídák's test. $n = 3$ technical repeats. **b**, AREG concentration in flank tumour lysate ± 20 Gy RT, measured by ELISA 5 days post-RT, $n = 5$ mice in AR+ groups, $n = 4$ in AR- groups. One-way ANOVA, Šídák's test. **c**, Serum AREG concentration in tumour-bearing mice ± 20 Gy RT, measured by ELISA. Blood draw timepoints post-RT as indicated, ctrl - $n = 3$ non-tumour bearing mice, $n = 5$ mice in other groups. Two-way ANOVA, Tukey's test. **d**, CT-images of orthotopic $LLC^{AR+}$ and $LLC^{AR-}$ tumours on days 8, 11, and 14 post-injection. White asterisks/red highlights indicate tumours. **e**, Growth curves of $LLC^{AR+}$ and $LLC^{AR-}$ orthotopic lung tumours ± 8 or 12 Gy CT-guided RT. $n = 6$ mice per group. Two-way ANOVA, Šídák's test. **f**, Serum AREG concentration of $LLC^{AR+}$ and $LLC^{AR-}$ orthotopic lung tumour-bearing mice five days after 8 or 12 Gy RT, measured by ELISA, $n = 4$ mice in all groups. One-way ANOVA, Šídák's test. **g**, Number of contralateral lung metastases (left) and mean size of the five largest metastases per contralateral lung area (right) from $LLC^{AR+}$ and $LLC^{AR-}$ orthotopic tumours ($n = 4$ in $LLC^{AR+}$, $n = 5$ in $LLC^{AR-}$, $n = 6$ mice in others). One-way ANOVA, Šídák's test. **h**, H&E staining of $LLC^{AR+}$ and $LLC^{AR-}$ orthotopic lung tumours. Black arrows indicate contralateral intrapulmonary metastatic lesions, white asterisks = orthotopic tumours, LN = extrapulmonary, intrathoracic lymph node metastasis. **i**, AREG MFI in LMB and LLC tumour cells post 4 Gy and 8 Gy RT in vitro, determined by flow cytometry. $n = 2$ technical repeats in LLC + 8 Gy, $n = 3$ in all other groups. **j**, Growth curves of LMB flank tumours ± RT with indicated doses, $n = 4$ mice in all groups, two independent experiments. Two-way ANOVA, Tukey's test. **k**, Number of LMB lung metastases (left) and mean size of the five largest lung metastases per lung area (right), $n = 5$ mice in LMB and 5 Gy groups, $n = 4$ in 10 Gy and 20 Gy groups. One-way ANOVA, Dunnett's test. **l**, H&E staining. Black arrows indicate metastatic lesions. RT doses as indicated. **m**, *Areg* upregulation in $LMB^{AR+}$ and $LMB^{AR-}$ cells after 4 Gy RT in vitro post-RT, RT-qPCR. One-way ANOVA, Šídák's test. $n = 3$ technical repeats. **n**, Growth curves of $LMB^{AR+}$ and $LMB^{AR-}$ flank tumours ± 5 Gy; $n = 4$ mice in $LMB^{AR-}$ + 5 Gy group, $n = 5$ mice in all others. **o**, Number of lung metastases (left), and mean size of five largest metastases per lung area (right), $n = 4$ mice in AR+ groups, $n = 5$ in AR- groups. One-way ANOVA, Šídák's test. **p**, H&E staining. Black arrows indicate metastatic lesions. Data are shown as mean ± SEM; box plots show median (Q2), Q1–Q3, and whiskers (min–max).



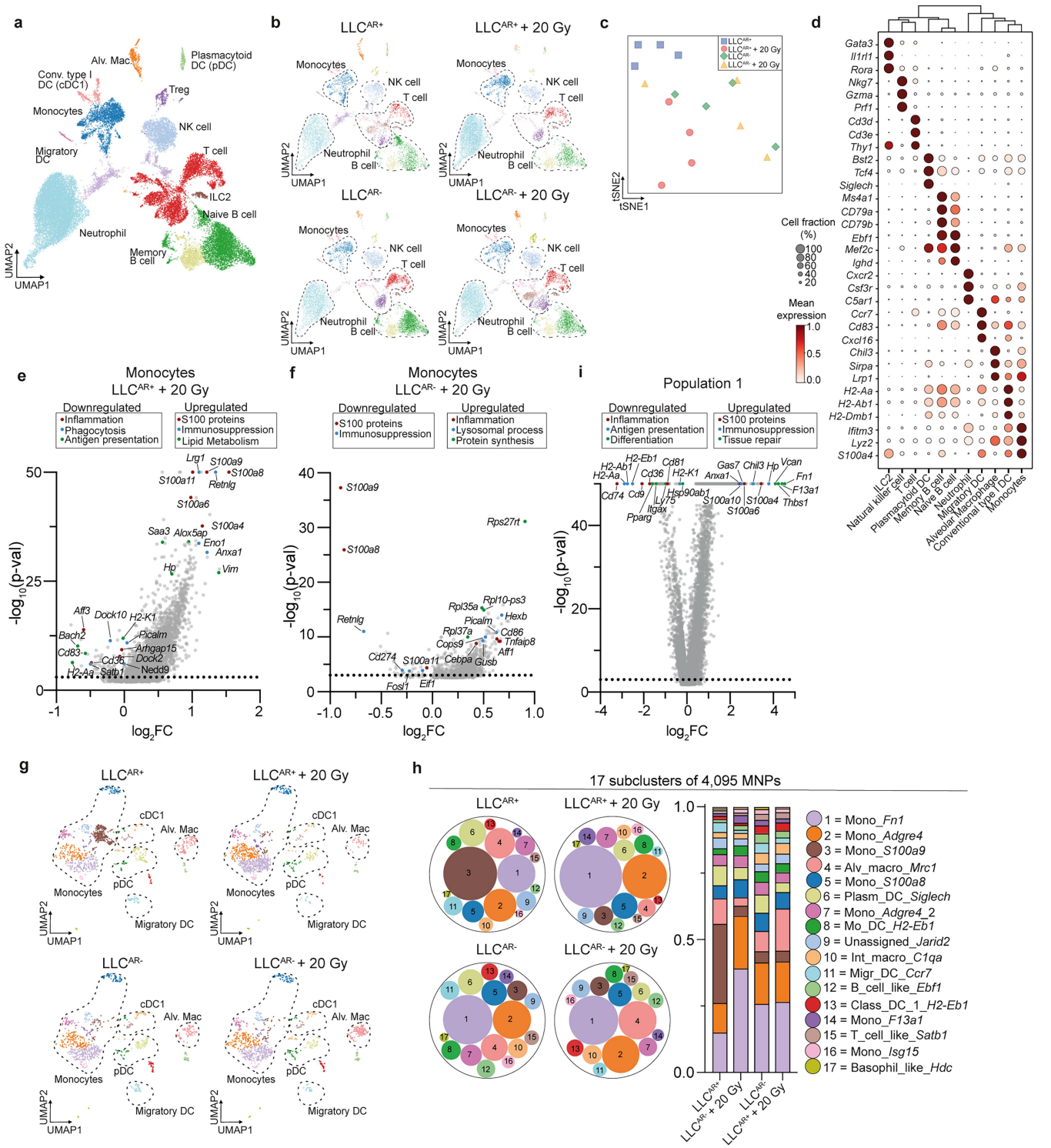

**Extended Data Fig. 3 | Proliferative, migratory, and clonogenic behaviour of AR+ and AR- LLC and LMB cells with and without RT. a**, In vitro proliferation of tumour cells treated with recombinant AREG. Proliferation measured as percent of confluency, analysed by live cell imaging over 72 h, $n = 3$ wells per condition and cell line. **b**, In vitro horizontal migration after scratch-wound assay of tumour cells treated with recombinant AREG. Migration measured as percent of confluency of wound area, analysed by live cell imaging over 48 h. $n = 3$ wells per condition and cell line. **c**, In vitro proliferation of tumour cells treated with RT. Proliferation measured as percent of confluency, analysed by live cell imaging over 72 h. Cells were irradiated with 0, 2, 4, or 6 Gy 24 h before start of proliferation assay. $n = 3$ wells per condition and cell line. **d**, In vitro migration of tumour cells measured by transwell assay. $1 \times 10^3$ cells were plated in serum-free media in inserts (8.0 µm pore size) overnight. Cells in the mesh were counted as migrating cells (left), images of migrated cells in mesh (right), $n = 3$ wells per cell line. **e**, In vitro migration of tumour cells post-RT measured by transwell assay. Tumour cells were irradiated with 0, 2, 4, or 6 Gy. The next day $1 \times 10^3$ cells were plated in serum-free media in inserts (8.0 µm pore size) overnight, $n = 4$ wells per condition and cell line. **f**, Microscopy images of migrated cells post-RT in mesh. **g**, In vitro colony formation of tumour cells treated with RT. 100 cells were seeded / well, allowed to attach overnight and then irradiated with 0, 2, 4, 6, or 8 Gy. Colonies containing >50 cells were counted 10 days after seeding, $n = 3$ wells per condition and cell line. **h**, In vitro colony formation of AR+ and AR- tumour cells treated with recombinant AREG. Colonies containing >50 cells were counted 10 days after seeding, $n = 3$ wells per condition and cell line. Panels **a**-**e**, **g**–**h** representative of at least two independent experiment with similar results. Data are shown as mean ± SEM for **a**-**e** and mean for **g**–**h**.




**Extended Data Fig. 4 | Recombinant AREG mimics tumour cell-derived AREG phenotype in vivo. a**, H&E staining of lungs 7 days post i.v. injection of $1 \times 10^5$ LLC$^{AR+}$ and LLC$^{AR-}$ tumour cells. Black arrows indicate metastatic lesions. **b**, Number of lung metastases (left), and mean size of five largest metastases per lung area (right), $n = 4$ mice per group. Unpaired two-sided t-test. **c**, H&E staining of lungs 14 days post i.v. injection of $1 \times 10^5$ LLC$^{AR+}$ and LLC$^{AR-}$ tumour cells. Black arrows indicate metastatic lesions. **d**, Number of lung metastases (left), and mean size of five largest metastases per lung area (right), $n = 4$ mice per group. Unpaired two-sided t-test. **e**, Number of metastases per lung (left) and mean size of largest metastases per lung area after ± intravenous (i.v.) recombinant AREG (rAR) treatment (right), $n = 5$ in LLC$^{AR+}$ + rAR group, $n = 4$ mice in all other groups. One-way ANOVA, Šídák's test. **f**, Growth curve of LLC flank tumours ± 20 Gy RT or complete surgical resection of the flank tumour on day 11, 14, and 18, $n = 4$ mice in 20 Gy, $n = 5$ in all other groups. **g**, AREG concentration in serum of tumour-bearing mice five days after 20 Gy RT or complete surgical resection of the flank tumour, measured by ELISA, $n = 3$ mice in 20 Gy, $n = 5$ in all other groups. One-way ANOVA, Šídák's test. **h**, Number of lung metastases (left - One-way ANOVA, Šídák's test), and mean size of the five largest metastases per lung area (right – unpaired two-sided t-test), $n = 4$ mice in 20 Gy, $n = 5$ in all other groups. **i**, H&E staining. Black arrows indicate metastatic lesions. **j**, Dot plot of Gene Set Enrichment Analysis (GSEA) comparing upregulated Hallmark pathways in RNA-seq of LLC$^{AR+}$ + 4 Gy. **k**, Volcano plot of up- and downregulated genes in LLC$^{AR+}$ cells + 4 Gy RT. Significantly upregulated differentially-expressed genes (DEGs) involved in type-I-IFN pathway are coloured in red. DEGs determined by Wald test, Benjamini-Hochberg FDR correction (DESeq2). **l**, Relative expression of *Areg* in LLC$^{AR+}$ cells after interferon β (IFNβ) treatment, measured by RT-qPCR. One-way ANOVA, Dunnett's test. $n = 3$ technical repeats. **m**, AREG concentration in LLC$^{AR+}$ cells after IFNβ treatment, measured by ELISA. Kruskal-Wallis, Dunn's test. $n = 3$ technical repeats. **n**, Relative expression of *Areg* in LLC cells post-RT and siSTAT2 treatment, measured by RT-qPCR. One-way ANOVA, Šídák's test. $n = 3$ technical repeats. **o**, AREG concentration in LLC$^{AR+}$ cells after 4 Gy RT and siSTAT2 treatment, measured by ELISA. One-way ANOVA, Šídák's test. $n = 3$ technical repeats. Data are shown as mean ± SEM; box plots show median (Q2), Q1–Q3, and whiskers (min–max).

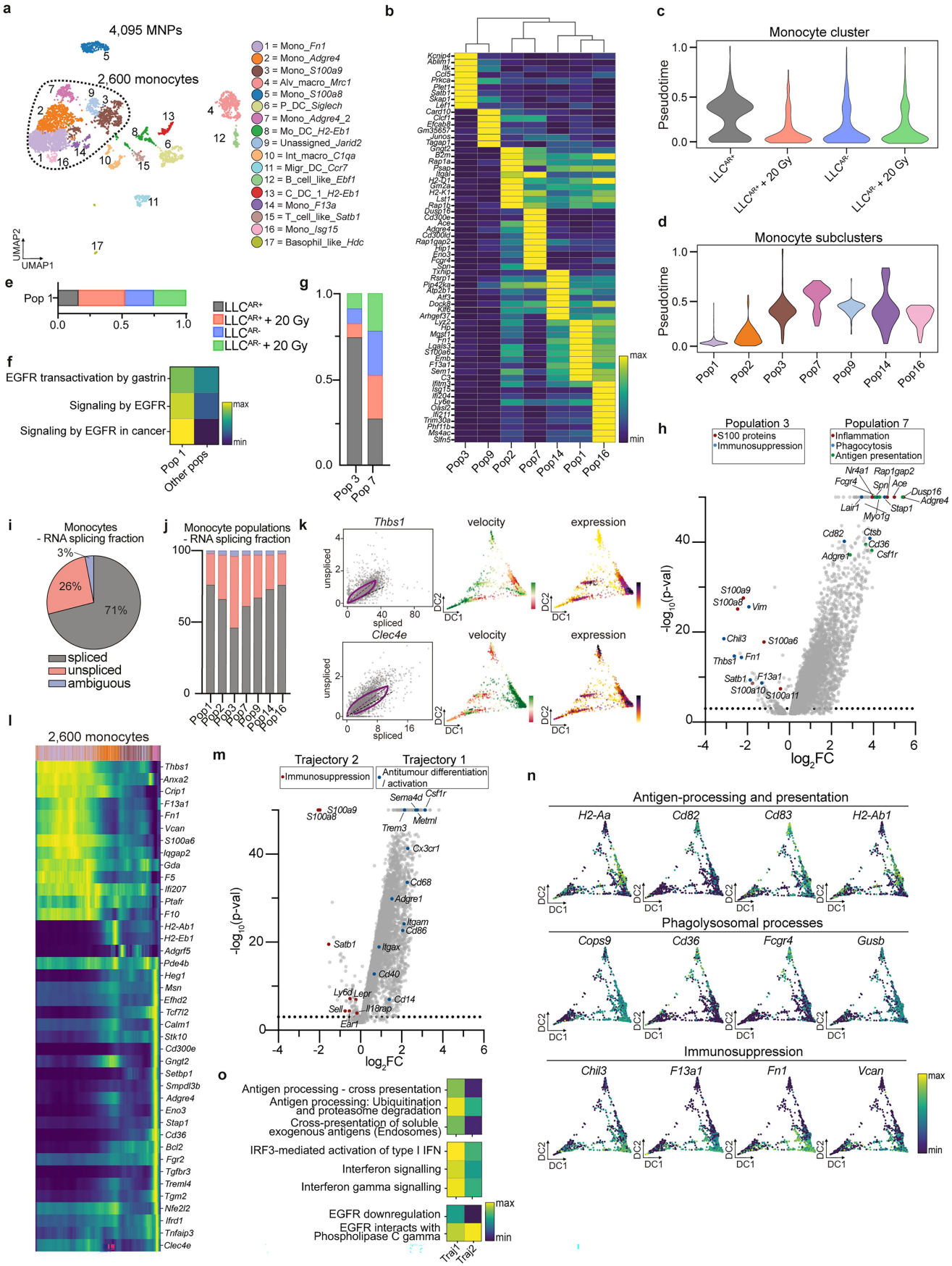



**Extended Data Fig. 5 | Extended information about human PBMC and immune cell populations in LLC$^{AR+}$ and LLC$^{AR-}$ lungs ± RT. a**, Spectral flow cytometry and unsupervised t-SNE clustering of 800,000 live CD45$^+$ PBMCs of $n = 30$ matched samples ($n = 15$ patients), pre- and post SBRT. Expression intensity of selected extracellular markers. **b**, Unsupervised cluster assignment of 25 PBMC clusters (k-nearest neighbours & FlowSOM). **c**, Heatmap of marker expression across PBMC clusters. Black box highlights CD33$^+$ CD14$^+$ p-EGFR$^+$ monocytes (population 4). **d**, Spectral flow cytometry and t-SNE clustering of 230,000 live CD45$^+$ immune cells from lungs of non-tumour-bearing ($n = 3$) and tumour-bearing ($n = 5$ per group) mice. Expression intensity of selected extracellular markers. **e**, Unsupervised cluster assignment of 16 murine lung immune cell clusters (k-nearest neighbours & FlowSOM). **f**, Heatmap of marker expression in murine lung immune cell clusters. Black box highlights Ly6C$^+$, F4/80$^+$, p-EGFR$^+$ monocyte-derived macrophages (population 3). **g**, t-SNE density plots from lung tissue of non-tumour-bearing (NTB) vs. tumour-bearing mice, myeloid and adaptive immune cell clusters are outlined. **h**, Heatmap of immune cell populations identified by surface marker expression using conventional gating, after max normalization of the fraction of live CD45$^+$ cells. Asterisk: highest fraction of Ly6C$^+$, F4/80$^+$ population. **i**, Quantification of CD8$^+$ and CD4$^+$ T cells and CD19$^+$ B cells in the lung tissue of LLC$^{AR+}$ and LLC$^{AR-}$ ± 20 Gy tumour-bearing mice, identified by surface marker expression using conventional gating, normalized per mg lung tissue, $n = 5$ mice per group. One-way ANOVA, Šídák's test. **j**, Schematic overview of workflow for AI-based cell segmentation model followed by logistic regression classifier training. DAPI nuclear stain= blue, Tyr992 p-EGFR = AF488 (green), Ly6C = PE/Dazzle 594 (red). **k**, Confusion matrix showing the performance of the classification model. AUC = area under the curve. Box plots in **i** show median (Q2), Q1–Q3, and whiskers (min–max).



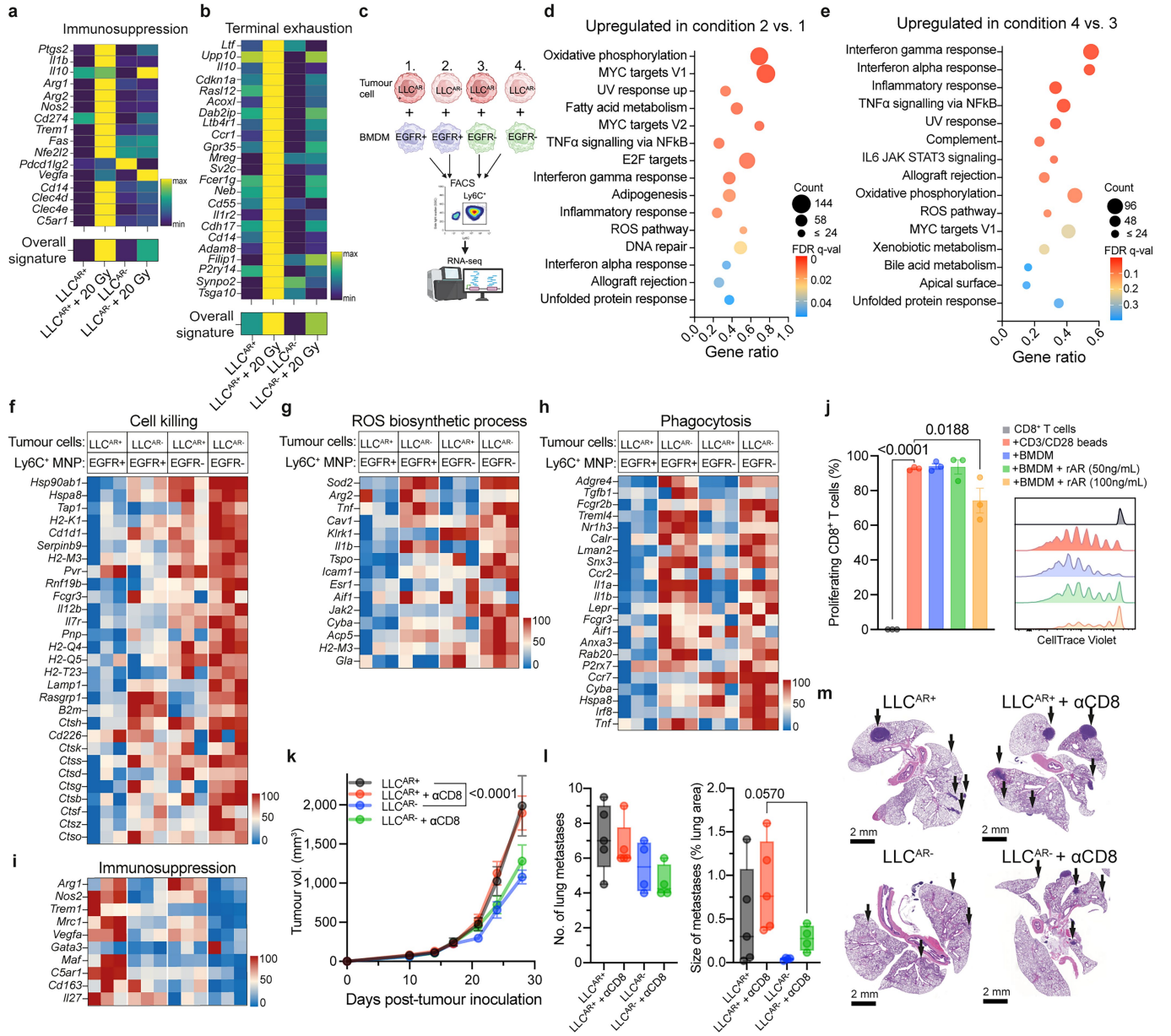

**Extended Data Fig. 6** | See next page for caption.

**Extended Data Fig. 6 | Extended information about immune populations identified by scRNA-seq in LLC$^{AR+}$ and LLC$^{AR}$ lungs ± 20 Gy. a**, Unsupervised uniform manifold approximation and projection (UMAP) of 32,690 live CD45$^{+}$ cells in the lungs of LLC$^{AR+}$ and LLC$^{AR-}$ tumour-bearing mice ± 20 Gy, *n* = 4 mice per group, annotated into 11 major cell lineages. Conv. type I DC = conventional type I dendritic cells, Alv. Mac = alveolar macrophages, Treg = regulatory T cells, NK cell = natural killer cells, ILC2 = group 2 innate lymphoid cells. **b**, UMAP of CD45$^{+}$ cells stratified by condition; monocytes, B cells, T cells, NK cells, and neutrophils are outlined. **c**, t-SNE projection of the global transcriptomic profile from 16 individually hashtagged mice across four conditions. **d**, Bubble plot showing the top three marker differentially expressed genes (DEGs) for 11 major cell lineages. DEGs identified by two-sided Wilcoxon rank-sum test. **e**, Volcano plot of DEGs in monocytes from LLC$^{AR+}$ + 20 Gy. Selected genes are coloured by function. P-values of 0 are depicted at $1^{-50}$ (log10). Two-sided Wilcoxon rank-sum test. **f**, Volcano plot of DEGs in monocytes from LLC$^{AR-}$ + 20 Gy. Selected genes are coloured by function. Two-sided Wilcoxon rank-sum test. **g**, UMAP of MNPs stratified by experimental condition. Monocytes, conv. type I DCs, plasmacytoid DCs, migratory DCs, and alveolar macrophages are outlined. Annotations assigned using Pegasus auto-annotation and top DEGs. Alv_mac = alveolar macrophage, cDC1 = conventional type 1 DC, pDC = plasmacytoid DC. Cluster colours consistent with Fig. 3c. **h**, Dot plot and bar graph showing the fraction of cells in 17 MNP subclusters across conditions. Mono = monocyte, Alv_macro = alveolar macrophage, Plasm_DC = plasmacytoid DC, Mo_DC = monocyte-derived DC, Int_macro = interstitial macrophage, Migr_DC = migratory DC, Class_DC_1 = classical type 1 DC. **i**, Volcano plot of DEGs in population 1 (Mono_*Fn1*). Selected genes are coloured by function. P-values of 0 are depicted at $1^{-50}$ (log10). Two-sided Wilcoxon rank-sum test.

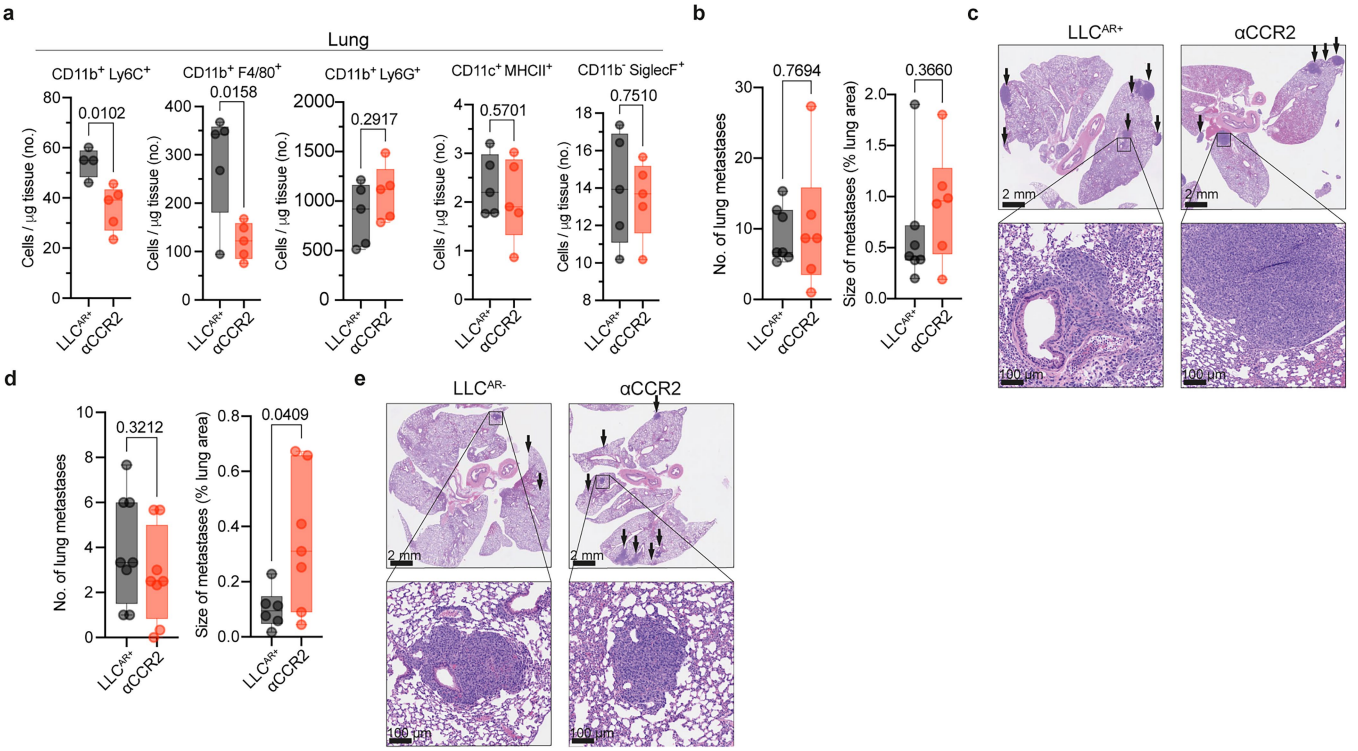



**Extended Data Fig. 7** | See next page for caption.

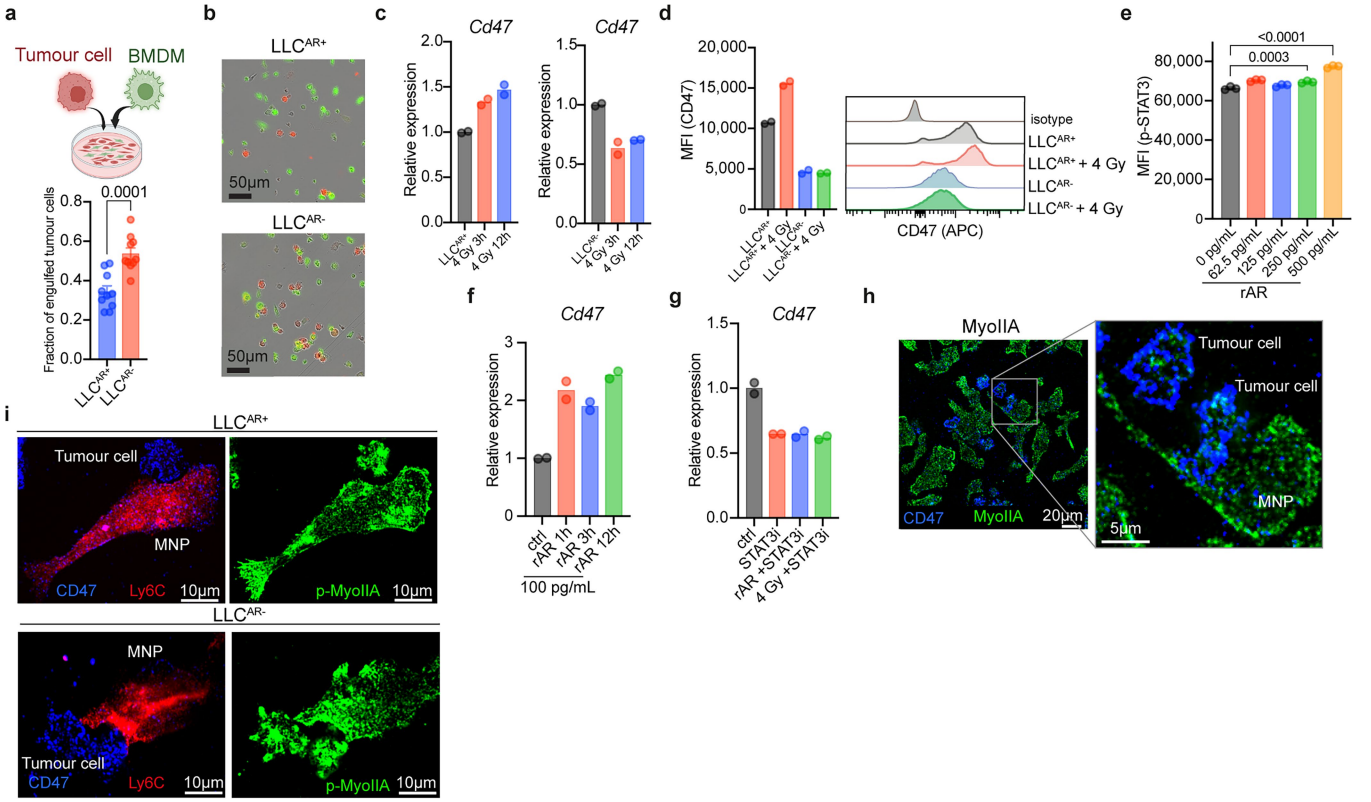
**Extended Data Fig. 7 | Extended information about pseudotime and trajectory analysis of monocytes identified by scRNA-seq. a**, UMAP of 4,095 MNPs from lungs of $LLC^{AR+}$ and $LLC^{AR-}$ tumour-bearing mice ± 20 Gy, $n = 4$ mice per group. Clusters used for pseudotime analysis (2,600 monocytes) outlined. Cluster colours and names consistent with Fig. 3c. **b**, Heatmap of top differentially expressed genes (DEGs) of the seven monocyte populations used for trajectory analysis. **c**, Violin plot of pseudotime values for 2,600 monocytes, stratified by experimental condition. **d**, Violin plot of pseudotime values across seven monocyte subpopulations. **e**, Frequency of cells from the four experimental groups in population 1. **f**, Heatmap of Reactome pathways related to EGFR signalling in population 1 vs. all other populations. **g**, Frequency of cells from four experimental conditions in Pop3 Mono_*S100a9* and Pop7 Mono_*Adgre4*. **h**, Volcano plot of DEGs in populations 3 and 7, selected genes coloured by function. P-values of 0 are depicted at $1^{-50}$ (log10). Two-sided Wilcoxon rank-sum test. **i**, Pie chart of total monocyte RNA splicing ratios detected by scVelo. **j**, Bar plot of splicing ratios across seven monocyte populations. **k**, Phase portraits of unspliced vs. spliced RNA ratios for *Thbs1* and *Clec4e* (first and last gene in **l**). Right: inferred velocity and gene expression projected onto diffusion map. **l**, Time-series heatmap of the top forty velocity-informed driver genes visualized across trajectory monocyte clusters, ordered by diffusion pseudotime. **m**, Volcano plot of DEGs in trajectories 1 and 2, selected genes coloured by function. P-values of 0 are depicted at $1^{-50}$ (log10). Two-sided Wilcoxon rank-sum test. **n**, Expression of selected genes involved in antigen processing and presentation, phagolysosomal processes and immunosuppression, projected onto the diffusion map. **o**, Heatmap of Reactome pathway enrichment in trajectories 1 and 2 related to antigen processing and presentation, inflammation, and EGFR signalling.



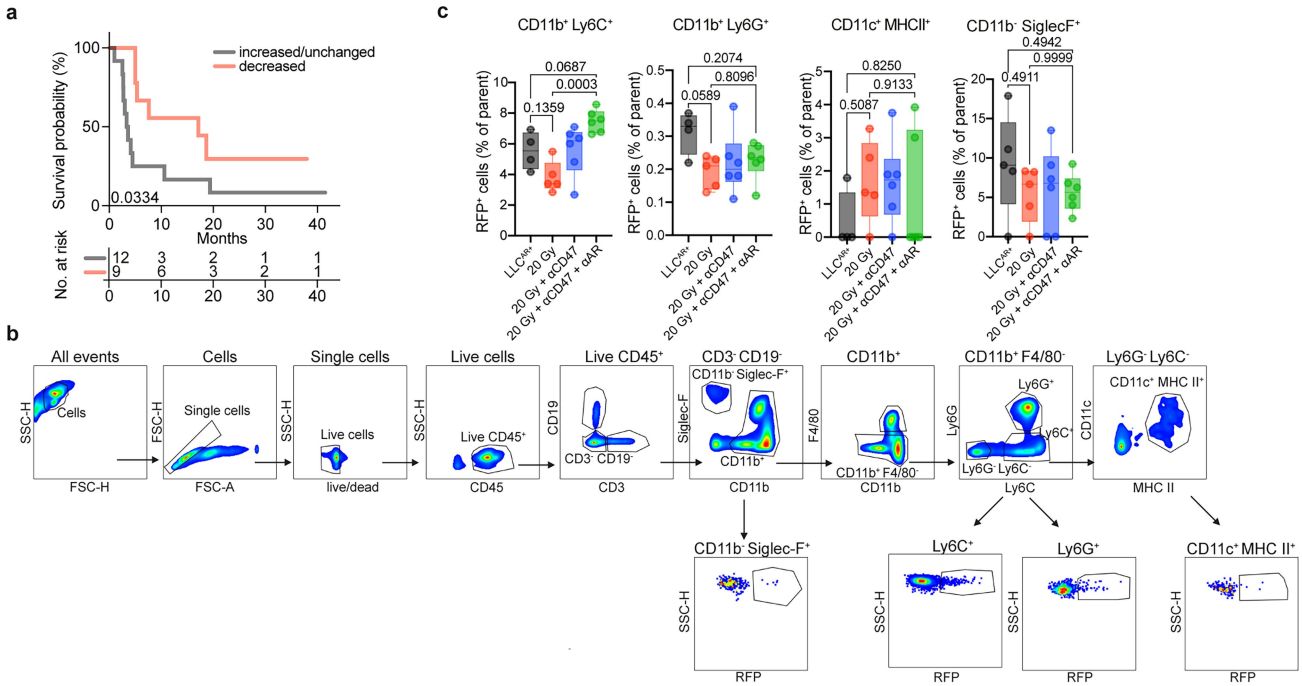

**Extended Data Fig. 8 | AREG induces T-cell suppressive monocyte phenotype, but T cells do not determine lung metastasis in vivo. a**, Heatmap of individual genes and overall gene signature genes involved in immunosuppression in monocyte cluster from Fig. 3a. **b**, Heatmap of individual genes and overall gene signature of terminal T-cell exhaustion (Miller et al.[31]) in CD8$^+$ T cell cluster 2 from Fig. 3a. **c**, Experimental setup: BMDM from *Egfr*$^{flx/flx}$ (EGFR + ) and LysM$^{\Delta Egfr}$ (EGFR-) mice were co-cultured with LLC$^{AR+}$ or LLC$^{AR-}$ tumour cells followed by fluorescence-activated cell sorting (FACS) of Ly6C$^+$ cells and RNA-seq ($n = 3$ technical replicates). Created in BioRender. Piffkó, A. (2025) https://BioRender.com/s42t906. **d**, Dot plot of Gene Set Enrichment Analysis (GSEA) showing upregulated Hallmark pathways in conditions 2 vs. 1 (LLC$^{AR-}$ + EGFR+ MNPs vs. LLC$^{AR+}$ + EGFR+ MNPs). Wald test and Benjamini-Hochberg method. **e**, Dot plot of GSEA showing upregulated Hallmark pathways in conditions 4 vs. 3 (LLC$^{AR-}$ + EGFR- MNPs vs. LLC$^{AR+}$ + EGFR- MNPs). Wald test and Benjamini-Hochberg method. **f**, Heatmap of normalized counts of genes involved in cell killing (RNA-seq of Ly6C$^+$ MNPs; gene signatures in **f-h** adapted from Wang et al.[29]). **g**, Heatmap of genes related to reactive oxygen species (ROS) biosynthetic processes in Ly6C$^+$ MNPs. **h**, Heatmap of phagocytosis-related genes in Ly6C$^+$ MNPs. **i**, Heatmap of immunosuppressive genes in Ly6C$^+$ MNPs. **j**, Proliferation of CD8$^+$ T cells after co-culture with bone-marrow derived myeloid cells (BMDM) pre-treated with rAR (left), and histogram of proliferating CD8$^+$ T cell populations (right), $n = 3$ technical replicates. One-way ANOVA, Šídák's test. **k**, Growth curves of LLC$^{AR+}$ and LLC$^{AR-}$ flank tumours ± i.v. CD8-antibody (αCD8), $n = 7$ mice in AR+ groups, $n = 6$ in LLC$^{AR-}$, $n = 8$ in LLC$^{AR-}$ + αCD8. Two-way ANOVA, Tukey's test. **l**, Number of metastases (left), and size of five largest metastases per lung area post-αCD8 treatment (right), $n = 5$ mice in AR+ groups, $n = 4$ mice in AR- groups. One-way ANOVA, Šídák's test. **m**, H&E staining. Black arrows indicate metastatic lesions. Data is shown as mean ± SEM; box plots show median (Q2), Q1–Q3, and whiskers (min–max).



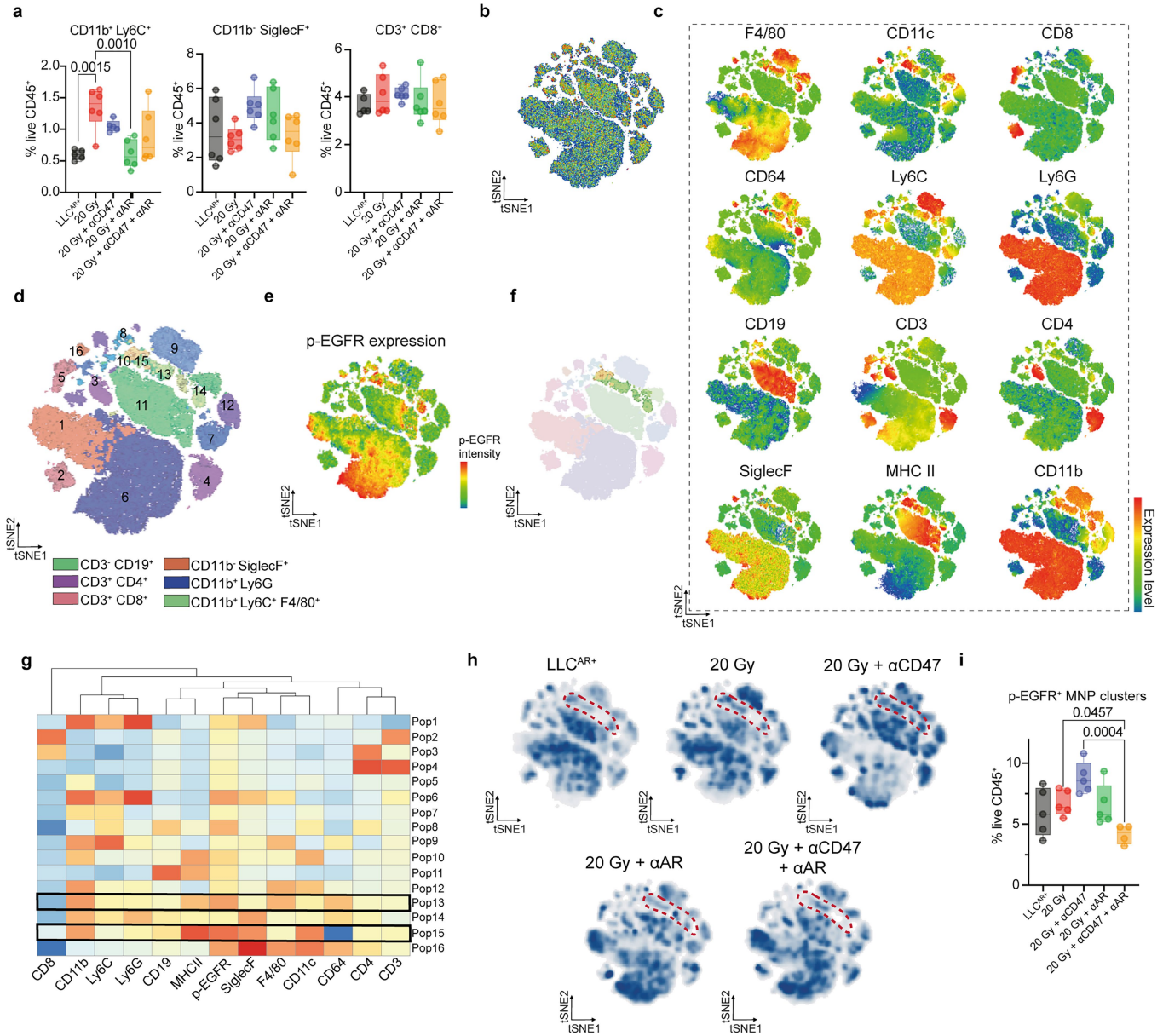

**Extended Data Fig. 9 | Anti-CCR2 antibody-mediated depletion of MNPs determines in vivo lung metastasis phenotype. a**, Count of $CD11b^+Ly6C^+$ monocytes, $CD11b^+F4/80^+$ macrophages, $CD11c^+MHCII^+$ dendritic cells, $CD11b^+Ly6G^+$ granulocytes, and $CD11b^-SiglecF^+$ alveolar macrophages per µg lung tissue in LLC tumour-bearing mice treated with anti-CCR2 antibody (αCCR2), $n = 5$ mice per group. Populations identified using conventional gating strategy. Unpaired two-sided t-test. **b**, Number of lung metastases (left), and mean size of the five largest metastases per lung area (right) of $LLC^{AR+}$ + αCCR2, $n = 7$ mice $LLC^{AR+}$, $n = 6$ mice αCCR2. Unpaired two-sided t-test for number and two-sided Mann-Whitney test for size. **c**, H&E staining. Black arrows indicate metastatic lesions. **d**, Number of lung metastases (left), and mean size of the five largest metastases per lung area (right) of $LLC^{AR-}$ + αCCR2, $n = 8$ mice $LLC^{AR-}$, $n = 7$ mice αCCR2. Unpaired two-sided t-test. **e**, H&E staining. Black arrows indicate metastatic lesions. Box plots show median (Q2), Q1–Q3, and whiskers (min–max).




**Extended Data Fig. 10 | AREG upregulates CD47 via STAT3 signalling to suppress MNP phagocytosis. a**, Schematic of live cell imaging co-culture system with CellTracker Red tumour cells and CellTracker Green bone-marrow derived myeloid cells (BMDM) (top). Fraction of engulfed LLC$^{AR+}$ and LLC$^{AR-}$ tumour cells after 4 h, $n = 10$ technical replicates (bottom). Created in BioRender, Piffkó A, 2025. https://biorender.com/t54k444. **b**, Live cell imaging of co-culture system with CellTracker labelled tumour cells and BMDMs. **c**, *Cd47* expression in LLC$^{AR+}$ (left) and LLC$^{AR-}$ post-RT (right), measured by RT-qPCR, $n = 2$ technical replicates. **d**, Histogram and quantification of CD47 mean fluorescence intensity (MFI) on LLC$^{AR+}$ and LLC$^{AR-}$ cells ± 4 Gy, $n = 2$ technical repeats. **e**, MFI of p-STAT3 (Tyr705) in LLC cells, after 25 min of rAR treatment at indicated concentrations, $n = 3$ technical replicates. One-way ANOVA, Šídák's test. **f**, *Cd47* expression in LLC$^{AR+}$ cells post-rAR treatment, measured by RT-qPCR, $n = 2$ technical replicates. **g**, *Cd47* expression in LLC$^{AR+}$ cells post-RT, rAR, and STAT3i (Stattic, 5 μM) treatment, measured by RT-qPCR, $n = 2$ technical replicates. **h**, IF staining of Ly6C$^+$ MNPs co-cultured with LLC tumour cells, stained for MyoIIA (AF488, green) and CD47 (BV421, blue). Close-up of phagocytic synapse. **i**, IF staining of Ly6C$^+$ MNPs co-cultured with LLC$^{AR+}$ (left) and LLC$^{AR-}$ (right). Stained for p-MyoIIA (AF488, green), Ly6C (PE/Dazzle 594, red), and CD47 (BV421, blue). Data are shown as mean ± SEM. One representative experiment out of two independent experiments is shown.




**Extended Data Fig. 11 | AREG blockade synergizes with anti-CD47 and increases MNP phagocytosis in vivo. a**, Kaplan-Meier plot of progression-free survival stratified by AREG serum levels, measured by ELISA. $n = 42$ samples from $n = 21$ patients (pre-SBRT and after three cycles of ICB + SBRT). Log-rank (Mantel-Cox) test. **b**, Representative gating strategy for mouse lung tissue identifying RFP+ phagocytic MNP populations. **c**, Percentage of phagocytic RFP$^+$Ly6C$^+$ monocytes (left), RFP$^+$Ly6G$^+$ neutrophils, RFP$^+$CD11c$^+$MHCII$^+$ dendritic cells, and RFP$^+$ CD11b$^-$Siglec-F$^+$ alveolar macrophages shown as percentage of the parent population. Cells isolated from lungs of LLC$^{AR+}$ tumour-bearing mice that were treated with 20 Gy RT or a combination with anti-AREG- (αAR) and anti-CD47-antibody (αCD47). $n = 5$ in LLC$^{AR+}$ and 20 Gy group, $n = 6$ in other groups. One-way ANOVA, Šídák's test. Box plots show median (Q2), Q1–Q3, and whiskers (min–max).




**Extended Data Fig. 12 | Tyr992 p-EGFR expression of Ly6C$^+$ MNPs from lung tissue of LLC$^{AR+}$ tumour-bearing mice treated with 20 Gy RT, αAR, and αCD47. a**, Percentage of CD11b$^+$ Ly6C$^+$ MNPs, CD11b$^-$ SiglecF$^+$ alveolar macrophages and CD3$^+$ CD8$^+$ T cells, shown as percentage of live CD45$^+$ cells from lungs of LLC$^{AR+}$ tumour-bearing mice treated with 20 Gy RT, anti-AREG-antibody (αAR), and anti-CD47-antibody (αCD47). $n = 6$ mice per group. One-way ANOVA, Šídák's test. **b**, t-SNE dimensionality reduction of 250,000 live CD45$^+$ immune cells from lung tissue. **c**, Expression intensity of extracellular markers projected onto t-SNE. **d**, Identification of 16 immune cell populations by unsupervised clustering (k-nearest neighbours & FlowSOM). **e**, Expression intensity of Tyr992 p-EGFR projected onto t-SNE. **f**, Identification of two clusters with the highest p-EGFR expression (Clusters 13 and 15). **g**, Heatmap of marker expression across 16 clusters. Black boxes highlight MNP populations with high expression of Tyr992 p-EGFR (populations 13 and 15). **h**, Density plot of t-SNEstratified by experimental condition; p-EGFR$^+$ MNP populations outlined. **i**, Percentage of p-EGFR$^+$ MNP populations, shown as percentage of live CD45$^+$ cells, $n = 5$ mice per group. One-way ANOVA, Šídák's test. Box plots show median (Q2), Q1–Q3, and whiskers (min–max).

nature portfolio

Corresponding author(s): Ralph R. Weichselbaum

Last updated by author(s): Mar 14, 2025

# Reporting Summary

Nature Portfolio wishes to improve the reproducibility of the work that we publish. This form provides structure for consistency and transparency in reporting. For further information on Nature Portfolio policies, see our Editorial Policies and the Editorial Policy Checklist.

## Statistics

For all statistical analyses, confirm that the following items are present in the figure legend, table legend, main text, or Methods section.

| n/a | Confirmed |
|---|---|
| ☐ | ☒ The exact sample size (*n*) for each experimental group/condition, given as a discrete number and unit of measurement |
| ☒ | ☐ A statement on whether measurements were taken from distinct samples or whether the same sample was measured repeatedly |
| ☐ | ☒ The statistical test(s) used AND whether they are one- or two-sided<br>*Only common tests should be described solely by name; describe more complex techniques in the Methods section.* |
| ☐ | ☒ A description of all covariates tested |
| ☐ | ☒ A description of any assumptions or corrections, such as tests of normality and adjustment for multiple comparisons |
| ☐ | ☒ A full description of the statistical parameters including central tendency (e.g. means) or other basic estimates (e.g. regression coefficient) AND variation (e.g. standard deviation) or associated estimates of uncertainty (e.g. confidence intervals) |
| ☐ | ☒ For null hypothesis testing, the test statistic (e.g. *F*, *t*, *r*) with confidence intervals, effect sizes, degrees of freedom and *P* value noted<br>*Give P values as exact values whenever suitable.* |
| ☒ | ☐ For Bayesian analysis, information on the choice of priors and Markov chain Monte Carlo settings |
| ☒ | ☐ For hierarchical and complex designs, identification of the appropriate level for tests and full reporting of outcomes |
| ☒ | ☐ Estimates of effect sizes (e.g. Cohen's *d*, Pearson's *r*), indicating how they were calculated |

*Our web collection on statistics for biologists contains articles on many of the points above.*

## Software and code

Policy information about availability of computer code

| | |
|---|---|
| Data collection | SpectroFlo Software (3.3.0) to collect the flow cytometry data; Excel (16.63.1) for tumour size measurements, CRi Panoramic SCAN 40x Whole Slide Scanner to collect H&E and IHC data; NovaSeq6000 (Illumina) to collect scRNA-seq raw data; NovaSeqX (Illumina) to collect RNA-seq raw data; Incucyte Base software (v2019A) to collect live cell imaging data |
| Data analysis | FlowJo (10.8.1) for flow cytometry analysis with FlowJo plugins Phenograph (2.4), ClusterExplorer (1.7.4), and FlowSOM (3.0.18). GraphPad Prism (10.3.1) for statistical data analysis of in vivo tumor, flow and metastasis data; Qupath (0.3.0) and ImageJ (1.54g) for H&E and IF data, Incucyte Base software (v2019A) for live cell imaging data. For scRNA-seq: Cellranger (7.1.0), Python Pegasus (1.8.1), scanpy (1.8.1), Seurat (4.4.0), Slingshot (3.18), Velocyto (0.17.17), scVelo (0.3.2), R (4.3). For RNA-seq: STAR (2.7.10b, Subread (2.0.5) DESeq2 in Bioconductor 1.46.0, GSEA (4.3.2). A custom code has been developed for AI-assisted monocyte detection in IF stainings using the human-in-the-loop pipeline of Cellpose (2.0) and has been deposited on Github (https://github.com/apiffko/IF.mono.quantif) and Zenodo (https://doi.org/10.5281/zenodo.14982759) - please see Code reporting summary for more details. |

For manuscripts utilizing custom algorithms or software that are central to the research but not yet described in published literature, software must be made available to editors and reviewers. We strongly encourage code deposition in a community repository (e.g. GitHub). See the Nature Portfolio guidelines for submitting code & software for further information.

## Data

Policy information about availability of data

All manuscripts must include a data availability statement. This statement should provide the following information, where applicable:

- Accession codes, unique identifiers, or web links for publicly available datasets
- A description of any restrictions on data availability
- For clinical datasets or third party data, please ensure that the statement adheres to our policy

All data generated or analyzed during this study are included in this published article (and its supplementary information files). Source data are provided with this paper. The single-cell RNA sequencing data have been deposited at the Gene Expression Omnibus (GEO) repository with the accession number GSE250375. The bulk-RNA sequencing data have been deposited at the GEO repository with the accession number GSE291151. The microarray data of the patients with advanced solid tumors enrolled in the clinical trial (NCT02608385) are available from the corresponding author on reasonable request. The human LUSC genomic and clinical data were derived from the TCGA Research Network (http://cancergenome.nih.gov) using the Xena platform (https://xena.ucsc.edu/). Mouse reference genome (mm10-2020A): https://www.ncbi.nlm.nih.gov/grc/mouse. Molecular Signature Database: https://www.gsea-msigdb.org/gsea/msigdb/index.jsp. Reactome datasets: https://reactome.org/.

## Research involving human participants, their data, or biological material

Policy information about studies with human participants or human data. See also policy information about sex, gender (identity/presentation), and sexual orientation and race, ethnicity and racism.

| | |
|---|---|
| Reporting on sex and gender | Does not apply. |
| Reporting on race, ethnicity, or other socially relevant groupings | Does not apply. |
| Population characteristics | NCT02608385 is a phase I/II trial designed to evaluate the safety and efficacy of pembrolizumab with multisite stereotactic body radiation therapy in patients with advanced solid tumors.<br>The COSINR study (NCT03223155) is a randomized phase I/II trial designed to evaluate the safety and efficacy of combination immune checkpoint blockade (ICB) and stereotactic body radiotherapy (SBRT) as first-line treatment for patients with stage IV NSCLC. |
| Recruitment | Eligibility criteria for NCT02608385 are described in: Luke, J.J. et al. Safety and Clinical Activity of Pembrolizumab and Multisite Stereotactic Body Radiotherapy in Patients with advanced solid tumors. JCO 36, 1611-1618 (2018).<br>Eligibility criteria for NCT03223155 are described in: Bestvina, C.M. et al. A Phase 1 Trial of Concurrent or Sequential Ipilimumab, Nivolumab, and Stereotactic Body Radiotherapy in Patients With Stage IV NSCLC Study. JTO 17, 130-140 (2022). |
| Ethics oversight | NCT02608385 was approved University of Chicago Biological Sciences Division IRB Committee (IRB15-1130)<br>NCT03223155 was approved by the University of Chicago Biological Sciences Division IRB Committee (IRB17-0547-CR003).<br>All patients treated on the trials provided written informed consent. |

Note that full information on the approval of the study protocol must also be provided in the manuscript.

# Field-specific reporting

Please select the one below that is the best fit for your research. If you are not sure, read the appropriate sections before making your selection.

☒ Life sciences ☐ Behavioural & social sciences ☐ Ecological, evolutionary & environmental sciences

For a reference copy of the document with all sections, see nature.com/documents/nr-reporting-summary-flat.pdf

# Life sciences study design

All studies must disclose on these points even when the disclosure is negative.

| | |
|---|---|
| Sample size | Sample sizes were chosen based on previous studies; Yang at al. 2022 (https://doi.org/10.1038/s41565-022-01225-x), and Wang et al. 2023 (https://doi.org/10.1016/j.ccell.2023.04.019). This estimate informed our power analysis and allowed us to choose a sample size balancing statistical power with practical considerations such as time, cost and resource availability. Ethical considerations (3R) played a role in determining sample size for in vivo experiments, by aiming to use the smallest number of subjects necessary to achieve reliable results. |
| Data exclusions | For in vivo experiments, individual mice were removed from the study either prior to treatment, if found to be an engraftment outlier or from the final analysis if, at end point, the mouse was found to be a significant outlier with regards to tumor growth. These exclusion criteria were established prior to tumor engraftment. All outlier calculations for in vivo experiments were performed using the GraphPad Outlier Calculator (https://www.graphpad.com/quickcalcs/Grubbs1.cfm). |
| Replication | The murine experiments were performed independently for two or three times as indicated in respective figure legends. The human PBMC |

| | |
|---|---|
| Replication | and biopsy gene array analysis, as well as the scRNA-seq were performed as single experiments. Number of biological / technical replicates is indicated in the figure legends. |
| Randomization | Mice were allocated to treatment or control groups based on the average tumor size to achieve similar tumor burden between groups at the time of treatment initiation. Age- and sex matched mice were used within an experiment, and age- and sex-matched littermate controls were used for studies involving conditional KO mice. For all other experiments, samples were randomly allocated. |
| Blinding | Drug administration and tumor measurements were performed by two different groups of investigators. Data analysis (flow cytometry / H&E) was independently assessed in a blinded manner by a second investigator. Blinding was not fully implemented for in vitro assays because treatment conditions required adjustments during handling, such as media changes and incubation times. |

# Reporting for specific materials, systems and methods

We require information from authors about some types of materials, experimental systems and methods used in many studies. Here, indicate whether each material, system or method listed is relevant to your study. If you are not sure if a list item applies to your research, read the appropriate section before selecting a response.

## Materials & experimental systems

| n/a | Involved in the study |
|---|---|
| ☐ | ☒ Antibodies |
| ☐ | ☒ Eukaryotic cell lines |
| ☒ | ☐ Palaeontology and archaeology |
| ☒ | ☐ Animals and other organisms |
| ☐ | ☒ Clinical data |
| ☒ | ☐ Dual use research of concern |
| ☒ | ☐ Plants |

## Methods

| n/a | Involved in the study |
|---|---|
| ☒ | ☐ ChIP-seq |
| ☐ | ☒ Flow cytometry |
| ☒ | ☐ MRI-based neuroimaging |

## Antibodies

Antibodies used

Antibodies used for IF stainings:
pEGFR, Tyr 992, #44786G, Invitrogen, 1:100
Ly6C-PE/Dazzle 594, HK1.4, #128044, Biolegend, 1:100
CD47, BV421, miap301 #127527, Biolegend, 1:100
SIRPα, AF647, P84, #144028, Biolegend, 1:100
Phospho-Myosin Light Chain 2 (Ser19), #3671, Cell Signaling, 1:100
Myosin IIa Antibody, #3403, Cell Signaling, 1:100
Anti-Rabbit IgG (H+L), AF488, #A32731, Invitrogen, 1:500

Hashtag antibodies for scRNA-seq:
B0301 Hashtag 1, M1/42, 155831, Biolegend, 1:200
B0302 Hashtag 2, M1/42 155833, Biolegend, 1:200
B0303 Hashtag 3, M1/42 155835, Biolegend 1:200
B0304 Hashtag 4, M1/42 155837, Biolegend 1:200

Antibodies used in vivo
CD47, BE0270, BioXcell, IAP, 200 ug x 4
AREG, AF989, R&D Systems 1.5ug/ml blood volume, x 4
Rat IgG2a BE0089 BioXcell 2A3 200 ug x 4
Goat IgG BE0130 BioXcell200 ug x 4

Murine antibodies used for flow cytometry:
CD16/32 BE0307 BioXcell 2.4G2 unconjugated 1:100
CD11b 101241 BioLegend M1/70 BV711 1:200
CD11c 117329 BioLegend N418 BV421 1:200
CD3 100249 BioLegend 17A2 BV750 1:200
CD4 100410 BioLegend GK1.5 PE-Cy5 1:200
CD45 58-0451-82 invitrogen 30-F11 AF532 1:200
CD8a 100759 BioLegend 53-6.7 BV711 1:200
CD8a 53-6.7, 563786, BD, BUV395, 1:200
CD8a 100714 BioLegend 53-6.7 APC-Cy7 1:200
CD8a 563786 BD Biosciences 53-6.7 BUV395 1:200
F4/80 123110 BioLegend BM8 PE 1:200
F4/80 123141 BioLegend BM8 BV785 1:200
F4/80 749282 BD Biosciences T45-2342 BUV805 1:200
LIVE/DEAD™ Fixable Yellow Dead Cell Stain L34959 invitrogen 1:2000
Zombie NIR Fixable Viability Kit Biolegend 423105 1:2000
Ly-6C 128012 BioLegend HK1.4 PerCP-Cy5.5 1:200
Ly-6G 560601 BD Biosciences 1A8 PE-Cy7 1:200
MHCII (I-A/I-E) 107622 BioLegend M5/114.15.2 AF700 1:200

NK-1.1 741233 BD Biosciences PK136 BUV563 1:200
NK-1.1 108748 BioLegend PK136 PE-CF594 1:200
PD-1 135225 BioLegend 29F.1A12 BV785 1:200
phospho-EGFR (Tyr992) polyclonal antibody (44-786G), 1:200 - conjugated with LYNX rapid antibody conjugation kit (LNK082C, BioRad)
AREG, AF989, R&D Systems, 1:200 - conjugated with LYNX rapid antibdoy conjugation kit (LNK142PERCPCY5.5, BioRad)
FoxP3 126419 BioLegend MF14 BV421 1:200
PD-L1 124336, BioLegend 10F9G2 BV650 1:200
CD206 141734, BioLegend C068C2 AF700 1:200
CCR7 120123, BioLegend 4B12 PE/Cy7 1:200
CD19 566167, BD, 6D5, BV480, 1:200
Tyr705 STAT3 Phospho, BioLegend 651004, 13A3-1, PE, 1:200
CD47, BV421, miap301 #127527, Biolegend, 1:200
CD47, APC, miap301 #127514, Biolegend, 1:200

Human antibodies used for flow cytometry:
FoxP3 (236A/E7), 14-4777-82, Invitrogen, PE/Cy7 1:200
CD20 (2H7), 14-0209-82, Invitrogen, SB436 1:200
CD16 (eBioCB16), 16-0168-85, Invitrogen, eFluor450 1:200
CD4 (SK3) 344602, Biolegend, BV750 1:200,
CCR7 (G043H7), 353207, Biolegend, BV421 1:200
PD-1 (EH12.2H7), 329950, Biolegend, BV650 1:200
PD-L1 (B7-H1), 329706, Biolegend, PE, 1:200
HLA-DR (L243), 980412, Biolegend, APC/Fire 750, 1:200
CD11c (3.9), 301636, Biolegend, BV605, 1:200
CD303 (BDCA-2), 354234, Biolegend, BV711, 1:200
CD304 (12C2) 354540, Biolegend, APC/Fire810 1:200
CD56 (NCAM16.2), 612928, BD, BUV563, 1:200
CD141 (1A4) 746604, BD, BV480, 1:200
CD45 (HI30), 612891, BD, BUV805, 1:200
CD3 (UCHT1), 58-0038-42, ThermoFisher, AF532, 1:200
CD33 (WM53), BDB740293, Fisher Scientific, BUV395, 1:200
CD8a (SK1), 46-0087-42, ThermoFisher, PerCP-eFluor 710, 1:200
CD1c (L161), 331544, Biolegend, BV785,1:200
CD71 (CY1G4), 334120, Biolegend, PE-Dazzle 594, 1:200
CD45RA (HI100), 304120, Biolegend, AlexaFluor 700, 1:200

Validation

All antibodies used are commercially available and validated by the manufacturers. Additional information can be found on the manufacturers websites.
Antibodies used for IF stainings:
pEGFR, Tyr 992, #44786G, Invitrogen https://www.thermofisher.com/antibody/product/Phospho-EGFR-Tyr992-Antibody-Polyclonal/44-786G
Ly6C-PE/Dazzle 594, HK1.4, #128044, Biolegend https://www.biolegend.com/nl-be/products/pe-dazzle-594-anti-mouse-ly-6c-antibody-12513
CD47, BV421, miap301 #127527, Biolegend https://www.biolegend.com/fr-ch/products/brilliant-violet-421-anti-mouse-cd47-antibody-15866
SIRPα, AF647, P84, #144028, Biolegend https://www.biolegend.com/fr-lu/products/alexa-fluor-647-anti-mouse-cd172a-sirpalpha-antibody-15378
Phospho-Myosin Light Chain 2 (Ser19), #3671, Cell Signaling https://www.cellsignal.com/products/primary-antibodies/myosin-iia-antibody/3403?srsltid=AfmBOorTUaCD5y787N6Iy33hn4zaqENIQGUOmHCmOYt4xHePp4M96Khp
Myosin IIa Antibody, #3403, Cell Signaling https://www.cellsignal.com/products/primary-antibodies/myosin-iia-antibody/3403?srsltid=AfmBOopTnkWSRJKug-k23v7eW9cfJ8_HNgCQD11Ufo9Hr7n_vXSpXJFF
Anti-Rabbit IgG (H+L), AF488, #A32731, Invitrogen, https://www.thermofisher.com/antibody/product/Goat-anti-Rabbit-IgG-H-L-Highly-Cross-Adsorbed-Secondary-Antibody-Polyclonal/A32731

Hashtag antibodies for scRNA-seq:
B0301 Hashtag 1, M1/42, 155831, Biolegend https://www.biolegend.com/fr-ch/products/totalseq-b0301-anti-mouse-hashtag-1-antibody-17771
B0302 Hashtag 2, M1/42, 155833, Biolegend https://www.biolegend.com/fr-ch/products/totalseq-b0302-anti-mouse-hashtag-2-antibody-17772
B0303 Hashtag 3, M1/42, 155835, Biolegend https://www.biolegend.com/fr-ch/products/totalseq-b0303-anti-mouse-hashtag-3-antibody-17773
B0304 Hashtag 4, M1/42, 155837, Biolegend https://www.biolegend.com/fr-ch/products/totalseq-b0304-anti-mouse-hashtag-4-antibody-17774

Antibodies used in vivo (Target molecule, catalog number, supplier, webpage)
CD47, BE0270, BioXcell https://bioxcell.com/invivomab-anti-mouse-cd47-iap-be0270
AREG, AF989, R&D Systems https://www.rndsystems.com/products/mouse-amphiregulin-antibody_af989
Rat IgG2a BE0089 BioXcell https://bxcell.com/product/rat-igg2a-isotype-control/
goat IgG BE0130 BioXcell https://bioxcell.com/invivomab-polyclonal-goat-igg-be0130

Antibodies used iin murine flow cytometry (Target molecule, catalog number, supplier, webpage)
CD16/32 BE0307 BioXcell 2.4G2 https://bioxcell.com/invivomab-anti-mouse-cd16-cd32-be0307
CD11b 101241 BioLegend https://www.biolegend.com/en-us/products/brilliant-violet-711-anti-mouse-human-cd11b-antibody-7927
CD11c 117329 BioLegend https://www.biolegend.com/en-us/products/brilliant-violet-421-anti-mouse-cd11c-antibody-7149
CD3 100249 BioLegend https://www.biolegend.com/en-us/products/brilliant-violet-750-anti-mouse-cd3-antibody-15755

CD4 100410 BioLegend https://www.biolegend.com/en-us/products/pe-cyanine5-anti-mouse-cd4-antibody-251
CD45 58-0451-82 invitrogen https://www.thermofisher.com/antibody/product/CD45-Antibody-clone-30-F11-Monoclonal/58-0451-82
CD8a 100759 BioLegend https://www.biolegend.com/en-us/products/brilliant-violet-711-anti-mouse-cd8a-antibody-7926
CD8a 563786 BD Biosciences https://www.bdbiosciences.com/en-us/products/reagents/flow-cytometry-reagents/research-reagents/single-color-antibodies-ruo/buv395-rat-anti-mouse-cd8a.563786
CD8a 100714 BioLegend https://www.biolegend.com/en-us/products/apc-cyanine7-anti-mouse-cd8a-antibody-2269
F4/80 123110 BioLegend https://www.biolegend.com/en-us/products/pe-anti-mouse-f4-80-antibody-4068
F4/80 123141 BioLegend https://www.biolegend.com/en-us/products/brilliant-violet-785-anti-mouse-f4-80-antibody-9919
F4/80 749282 BD Biosciences https://www.bdbiosciences.com/en-us/products/reagents/flow-cytometry-reagents/research-reagents/single-color-antibodies-ruo/buv805-rat-anti-mouse-f4-80.749282
LIVE/DEAD™ Fixable Yellow Dead Cell Stain L34959 invitrogen https://www.thermofisher.com/order/catalog/product/L34959?SID=srch-srp-L34959
Zombie NIR™ Fixable Viability Kit 423105 Biolegend https://www.biolegend.com/fr-lu/products/zombie-nir-fixable-viability-kit-8657
Ly-6C 128012 BioLegend https://www.biolegend.com/fr-lu/products/percp-cyanine5-5-anti-mouse-ly-6c-antibody-5967
Ly-6G 560601 BD Biosciences https://www.bdbiosciences.com/en-us/products/reagents/flow-cytometry-reagents/research-reagents/single-color-antibodies-ruo/pe-cy-7-rat-anti-mouse-ly-6g.560601
MHCII(I-A/I-E) 107622 BioLegend https://www.biolegend.com/fr-lu/products/alexa-fluor-700-anti-mouse-i-a-i-e-antibody-3413
NK-1.1 741233 BD Biosciences https://www.bdbiosciences.com/en-us/products/reagents/flow-cytometry-reagents/research-reagents/single-color-antibodies-ruo/buv563-mouse-anti-mouse-nk-1-1.741233
NK1.1 108748 Biolegend PK136 https://www.biolegend.com/en-us/products/pe-dazzle-594-anti-mouse-nk-1-1-antibody-10320
PD-1 135225 BioLegend https://www.biolegend.com/fr-lu/products/brilliant-violet-785-anti-mouse-cd279-pd-1-antibody-9874
FoxP3 126419 BioLegend BV421 1:200 https://www.biolegend.com/nl-be/products/brilliant-violet-421-anti-mouse-foxp3-antibody-12143?GroupID=BLG5706
PD-L1 124336, BioLegend BV650 1:500 https://www.biolegend.com/ja-jp/products/brilliant-violet-650-anti-mouse-cd274-b7-h1-pd-l1-antibody-16055
CD206 141734, BioLegend AF700 1:500 https://www.biolegend.com/en-gb/products/alexa-fluor-700-anti-mouse-cd206-mmr-antibody-13456?GroupID=BLG9506
CCR7 120123, BioLegend PE/Cy7 1:500 https://www.biolegend.com/en-gb/products/pe-cyanine7-anti-mouse-cd197-ccr7-antibody-13133?GroupID=BLG4001
CD19 566167, BD, BV480, 1:500 https://www.bdbiosciences.com/en-us/products/reagents/flow-cytometry-reagents/research-reagents/single-color-antibodies-ruo/bv480-rat-anti-mouse-cd19.566167?tab=product_details
AREG AF989, R&D Systems https://www.rndsystems.com/products/mouse-amphiregulin-antibody_af989
Tyr705 STAT3 Phospho, 651004, Biolegend, 13A3-1 https://www.biolegend.com/en-us/products/pe-anti-stat3-phospho-tyr705-antibody-12914
CD47, BV421, miap301 #127527, Biolegend, 1:200 https://www.biolegend.com/en-us/products/brilliant-violet-421-anti-mouse-cd47-antibody-15866
CD47, APC, miap301 #127514, Biolegend, 1:200 https://www.biolegend.com/en-us/products/apc-anti-mouse-cd47-antibody-9119

Antibodies used in human flow cytometry:
FoxP3 (236A/E7), 14-4777-82, Invitrogen, PE/Cy7 1:500 https://www.thermofisher.com/antibody/product/FOXP3-Antibody-clone-236A-E7-Monoclonal/25-4777-42
CD20 (2H7), 14-0209-82, Invitrogen, SB436 1:500 https://www.thermofisher.com/antibody/product/CD20-Antibody-clone-2H7-Monoclonal/14-0209-82
CD16 (eBioCB16), 16-0168-85, Invitrogen, eFluor450 1:500 https://www.thermofisher.com/antibody/product/CD16-Antibody-clone-eBioCB16-CB16-Monoclonal/16-0168-\85
CD4 (SK3) 344602, Biolegend, BV750 1:500, https://www.biolegend.com/de-at/products/purified-anti-human-cd4-antibody-6205
CCR7 (G043H7), 353207, Biolegend, BV421 1:500 https://www.biolegend.com/en-ie/products/brilliant-violet-421-anti-human-cd197-ccr7-antibody-7497?GroupID=BLG9610
PD-1 (EH12.2H7), 329950, Biolegend, BV650 1:500 https://www.biolegend.com/fr-ch/products/brilliant-violet-650-anti-human-cd279-pd-1-antibody-12364
PD-L1 (B7-H1), 329706, Biolegend, PE, 1:500 https://www.biolegend.com/en-gb/products/pe-anti-human-cd274-b7-h1-pd-l1-antibody-4375?GroupID=BLG5402
HLA-DR (L243), 980412, Biolegend, APC/Fire 750, 1:500 https://www.biolegend.com/de-de/products/apc-fire-750-anti-human-hla-dr-antibody-13051
CD11c (3.9), 301636, Biolegend, BV605, 1:500 https://www.biolegend.com/fr-ch/products/brilliant-violet-605-anti-human-cd11c-antibody-8603
CD303 (BDCA-2), 354234, Biolegend, BV711, 1:500 https://www.biolegend.com/ja-jp/products/brilliant-violet-711-anti-human-cd303-bdca-2-antibody-16057
CD304 (12C2) 354540, Biolegend, APC/Fire810 1:500 https://www.biolegend.com/fr-ch/products/apc-fire-810-anti-human-cd304-neuropilin-1-antibody-22109
CD56 (NCAM16.2), 612928, BD, BUV563, 1:500 https://www.bdbiosciences.com/en-us/products/reagents/flow-cytometry-reagents/research-reagents/single-color-antibodies-ruo/buv563-mouse-anti-human-cd56.612928?tab=product_details
CD141 (1A4) 746604, BD, BV480, 1:500 https://www.bdbiosciences.com/en-us/products/reagents/flow-cytometry-reagents/research-reagents/single-color-antibodies-ruo/bv480-mouse-anti-human-cd141.746604?tab=product_details
CD45 (HI30), 612891, BD, BUV805, 1:500 https://www.bdbiosciences.com/en-us/products/reagents/flow-cytometry-reagents/research-reagents/single-color-antibodies-ruo/buv805-mouse-anti-human-cd45.612891?tab=product_details
CD3 (UCHT1), 58-0038-42, ThermoFisher, AF532, 1:500 https://www.thermofisher.com/antibody/product/CD3-Antibody-clone-UCHT1-Monoclonal/58-0038-42
CD33 (WM53), BDB740293, Fisher Scientific, BUV395, 1:500 https://www.fishersci.com/shop/products/mouse-anti-human-cd33-buv395-clone-wm53-also-known-as-wm-53-bd-optibuild/BDB740293
CD8a (SK1), 46-0087-42, ThermoFisher, PerCP-eFluor 710, 1:500 https://www.thermofisher.com/antibody/product/CD8a-Antibody-clone-SK1-Monoclonal/46-0087-42
CD1c, 331544, Biolegend, BV785,1:500, https://www.biolegend.com/nl-nl/products/brilliant-violet-785-anti-human-cd1c-antibody-17375
CD71 334120, Biolegend, PE-Dazzle 594, 1: 500 https://www.biolegend.com/fr-lu/products/pe-dazzle-594-anti-human-cd71-

antibody-15988
CD45RA, 304120, Biolegend, AlexaFluor 700, 1:500 https://www.biolegend.com/de-at/products/alexa-fluor-700-anti-human-cd45ra-antibody-3421

## Eukaryotic cell lines

Policy information about cell lines and Sex and Gender in Research

| | |
|---|---|
| Cell line source(s) | Cell lines: LLC (CRL-1642) and E0771-LMB (CRL-3405) cells were purchased from ATCC (Manassas, VA) and were maintained according to the method of characterization used by ATCC. To enhance metastatic homing to the lungs, both LLC and EO771-LMB cell lines underwent two consecutive rounds of in vivo passaging via spontaneous lung metastases. For each passage, 1 × 10^6 cells were injected subcutaneously into the flanks of WT mice. After 28 days, spontaneous lung metastases were dissected, and metastatic tumour cells were isolated and re-cultured. CRISPR-Cas9 mediated Areg-depletion was conducted using amphiregulin CRISPR KO plasmid from Santa Cruz (sc-419185). sc-419185: amphiregulin CRISPR/Cas9 KO Plasmid (m) is a pool of 3 different gRNA plasmids:A:GCCAGAAGGCATTTCGCTTA. B: AGGGGACTACGACTACTCAG, C: TGCCGATGCCAATAGCTGCG. The cell lines were authenticated by flow cytometry, RT-qPCR and murine AREG-ELISA of conditioned cell culture media and tumour cell lysates. |
| Authentication | Cell lines were not independently authenticated beyond the identity provided from the ATCC. AR+ and AR- cell lines were authenticated by flow cytometry, RT-qPCR and murine AREG-ELISA of conditioned cell culture media and tumour cell lysates. |
| Mycoplasma contamination | All cell lines were mycoplasma negative. All cell lines were checked for pathogen contamination via Charles River Research Animal Diagnostic Services before use. |
| Commonly misidentified lines (See ICLAC register) | No commonly misidentified cell lines were used |

## Clinical data

Policy information about clinical studies

All manuscripts should comply with the ICMJE guidelines for publication of clinical research and a completed CONSORT checklist must be included with all submissions.

| | |
|---|---|
| Clinical trial registration | NCT02608385 & NCT03223155 |
| Study protocol | The full trial protocol of NCT02608385 is described in: Luke, J.J. et al. Safety and Clinical Activity of Pembrolizumab and Multisite Stereotactic Body Radiotherapy in Patients with advanced solid tumors. JCO 36, 1611-1618 (2018).<br><br>The full COSINR trial protocol (NCT03223155) is described in: Bestvina, C.M. et al. A Phase 1 Trial of Concurrent or Sequential Ipilimumab, Nivolumab, and Stereotactic Body Radiotherapy in Patients With Stage IV NSCLC Study. JTO 17, 130-140 (2022). |
| Data collection | 11 patients were analyzed from NCT02608385 and 15 and 21 patients from NCT03223155 for flow cytometry and serum ELISA, respectively. All clinical data were obtained and stored at the University of Chicago Medical Center. |
| Outcomes | Clinical evaluation of patients was performed during radiotherapy and with every immunotherapy treatment. Radiographic evaluation was performed using CT scans every 12 weeks, or earlier if clinically warranted. a modified version of RECIST version 1.1 was used to assess overall response, allowing for the incusion of both irradiated and nonirradiated metastases as target and nontarget metastases. The rest of the RECIST principles were applied. Tumor control was defined as any response other than progressive disease. The Kaplan-Meier method was used to estimate progression-free survival (PFS) and overall survival (OS), defined as the time from SBRT planning to either progression per RECIST criteria or death from any cause. |

## Flow Cytometry

### Plots

Confirm that:

☒ The axis labels state the marker and fluorochrome used (e.g. CD4-FITC).

☒ The axis scales are clearly visible. Include numbers along axes only for bottom left plot of group (a 'group' is an analysis of identical markers).

☒ All plots are contour plots with outliers or pseudocolor plots.

☒ A numerical value for number of cells or percentage (with statistics) is provided.

### Methodology

| | |
|---|---|
| Sample preparation | Lungs were minced and digested with 1 mg/mL collagenase IV (#C4-22-1G, Sigma-Aldrich) and 200 µg/mL DNase I (#04536282001, Millipore Sigma) at 37°C for 45-60 min on a shaker at 150 rpm/min. For some experiments, cells were then pelleted by centrifugation at 400 × g for 10 min and further purified with 40 and 70% Percoll (GE) solutions by centrifuging at 800 × g (no brake) for 20 min at room temperature. Non-tumor cells were collected from the interface. Red blood cells were lysed using ACK lysis buffer (#A1049201, Gibco). The resulting cell suspensions were filtered through 70 µm cell strainers. Samples were then washed with PBS and incubated with Zombie NIR (BioLegend, 423105) or LIVE/DEADTM yellow (L34959, Invitrogen) fixable viability dye (1:2000) for 10 min at 4°C. Fc blocking was performed using anti-FcR (2.4G2, #CP025, BioXcell, |

| | |
|---|---|
| | 1:100). For extracellular staining, surface marker antibodies were added in staining buffer (PBS with 2% FBS and 0.5 mM EDTA (#324506, Millipore-Sigma)) at a 1:200 dilution. For intracellular staining, cells were fixed and permeabilized using the BD Cytofix/Cytoperm solution (#554722, Fisher Scientific) for 60 minutes at 4°C and maintained in BD Perm/Wash buffer (#BDB554723, Fisher Scientific) per the manufacturer's instructions, followed by incubation with intracellular antibodies (1:100 dilution, 30 min, 4°C). |
| Instrument | Cytek Aurora (5-laser) |
| Software | SpectroFlo Software (3.3.) and FlowJo (10.8.1). |
| Cell population abundance | After antibody staining of single cells, FSC - SSC gating was used to determine pure live cell population to be analyzed. |
| Gating strategy | Gating was performed using fluorescence intensity which is distinct from negative control cells (no-staining). |

☒ Tick this box to confirm that a figure exemplifying the gating strategy is provided in the Supplementary Information.